DEVELOPING MODELS TO INVESTIGATE MECHANISMS OF GENOMIC IMPRINTING

Stellar K. Hur

A DISSERTATION

in

Cell and Molecular Biology

Presented to the Faculties of the University of Pennsylvania

in

Partial Fulfillment of the Requirements for the

Degree of Doctor of Philosophy

2017

Supervisor of Dissertation

_____

Dr. Marisa S. Bartolomei, Professor of Cell and Developmental Biology,
Perelman School of Medicine, University of Pennsylvania

Graduate Group Chairperson

_____

Dr. Daniel S. Kessler, Associate Professor of Cell and Developmental Biology,
Perelman School of Medicine, University of Pennsylvania

Dissertation Committee

Dr. Montserrat C. Anguera, Assistant Professor of Department of Biomedical Sciences,
School of Veterinary Medicine, University of Pennsylvania

Dr. Klaus H. Kaestner, Professor of Genetics,
Perelman School of Medicine, University of Pennsylvania

Dr. Paul J. Gadue, Associate Professor of Pathology and Laboratory Medicine,
Children's Hospital of Philadelphia

Dr. Zhaolan Zhou, Associate Professor of Genetics,
Perelman School of Medicine, University of Pennsylvania

This dissertation is dedicated to the ones who have inspired me to:

accept, understand, and appreciate.

ACKNOWLEDGMENT

I would like to thank my mentor Dr. Marisa Bartolomei for providing intellectual support and having faith in me in carrying out research. She has always respected and cared about my research and “never led me astray,” as she once said. This has also applied in personal interactions—she listens, understands, and gives best advices.

I would also like to thank the Bartolomei lab members. First and foremost, thank you to Dr. Joanne Thorvaldsen and Christopher Krapp, my amazing baymates and best mentors in many aspects. When I was secretly happy or sad for various reasons, they have always been there for me. I thank the former and current graduate students and research associates in the lab, Dr. Jamie Weaver, Dr. Lara Abramowitz, Dr. Rob Plasschaert, Martha Stefaniak, Frances Xin, Jen Myers SanMiguel, Aimee Juan, Suhee Chang, Blake Caldwell, and Tre Artis. They have set the highest standards for colleagues—they are the most warm-hearted, brilliant, and dedicated scientists. Lastly, I thank the former and current senior scientists in the lab, Dr. Folami Ideraabdullah, Dr. Sebastien Vigneau, Dr. Martha Susiarjo, Dr. Eric de Waal, Dr. Jennifer Kalish, and Dr. Lisa Vrooman. I truly appreciate all the science and soft skills I learned from them, which became especially helpful as I was preparing for the next stage of my career. I particularly thank the devoted contributors to the work in this dissertation—Dr. Joanne Thorvaldsen, Dr. Folami Ideraabdullah, Dr. Jennifer Kalish, Suhee Chang, and the former and current undergraduates Carolyn Lye and Alice Yu.

I am grateful for all the fruitful collaborative experiences. I would like to thank Dr. Andrea Riccio, Dr. Lacey Luense, Dr. Catherine May, Andrea Freschi, and Angela Hines, for their help in successfully developing and completing the projects that I have undertaken. I am also looking forward to the new collaboration on the iPSC project with the CHOP human ES/iPS core led by Dr. Paul Gadue.

I would like to thank my exemplary thesis committee, Dr. Montserrat Anguera, Dr. Klaus Kaestner, Dr. Zhaolan Zhou, and Dr. Paul Gadue. Every committee meeting was filled with cerebral discussion, and it has always guided me in the right direction. I specially thank the chair of my committee, Dr. Montserrat Anguera, for her hands-on help in deriving and characterizing iPSCs. She always greets me with a big smile and that is enough to make me feel supported.

I would like to thank my friends and family. Being away from family for so long would not have worked out without my loving friends in the US. I am also lucky to have many friends living outside the US—regardless of the time zone they are in or being able to see each other only occasionally, they find a time to talk to me and are the best supporters of mine. I thank my grandparents, who inspired me to pursue the field of science and always care about my well-being. Lastly, I thank my mother, aunt, and sister, who are my best friends. They understand, trust, and love me for who I am, which has become a cornerstone in decisions I have made at every stage of my life (and I know it will continuously be this way). I feel very fortunate to be surrounded by so many incredible people.

ABSTRACT

DEVELOPING MODELS TO INVESTIGATE MECHANISMS OF GENOMIC IMPRINTING

Stellar K. Hur

Dr. Marisa S. Bartolomei

Genomic imprinting is a conserved, essential process in mammalian development that regulates the expression of a small number of genes in a monoallelic, parent-or-origin-specific manner. Misregulation of imprinted genes is associated with imprinting disorders including Beckwith-Wiedemann syndrome (BWS) and Silver-Russell syndrome (SRS) that exhibit abnormal growth phenotypes. These disorders are associated with aberrant regulation of the imprinted loci in human 11p15 including the *H19/IGF2* locus. Finding various alterations of 11p15 associated with BWS and SRS inspires investigation of imprinting mechanisms in human, which could provide insights into therapeutics. Mouse models have been fundamental to the study of mechanisms of imprinting, serving as a proxy for the orthologous human locus. However, elements that regulate genomic imprinting, the imprinting control regions (ICRs), often diverge across species. Thus, it is essential to first understand whether the diverged ICR has a species-specific role in regulating imprinting. In Chapter 2, we generated a mouse in which the human ICR sequence replaces the orthologous mouse ICR at the *H19/Igf2* locus. We show that the imprinting mechanism has partially diverged between mouse and human, depending on the parental origin of the human ICR sequence in mouse. Additionally, we find that this mouse model is optimal for studying specific alterations associated with BWS and SRS. The partially diverging imprinting mechanism between mouse and human suggests that entirely human models are compelling alternatives. In Chapter 3, we demonstrate the derivation of induced pluripotent stem cells (iPSCs) from BWS patient fibroblasts. We find that the iPSCs exhibit proper epigenetic and transcriptional

signatures of BWS. Although we find that certain aspect of epigenetic perturbation is inevitable in our iPSCs, the consequence of this perturbation remains unknown. Therefore, we propose that the iPSCs can be differentiated into clinically-relevant cell types to elucidate molecular mechanisms leading to BWS. Overall, the work in this dissertation underscores the versatile and complementary use of different model systems in investigating imprinting mechanisms. In addition to serving as platforms to model imprinting disorders, these models provide insights into the evolutionary perspective of imprinting as well as the significance of various epigenetic mechanisms that regulate imprinting.

TABLE OF CONTENTS

LIST OF TABLES

LIST OF FIGURES

CHAPTER 1.
INTRODUCTION

1.1 Genomic imprinting

Two copies of autosomal genes exist in the mammalian genome, with each copy inherited from the respective parental allele. The majority of mammalian genes are simultaneously expressed or silenced from both parental alleles. However, a subset of genes, known as imprinted genes, are uniquely regulated such that their expression occurs in a monoallelic, parent-of-origin-specific manner (Figure 1.1).

Although imprinted genes comprise a small portion of the genome—about 150 imprinted genes have been identified in mouse and around half of them are conserved in human—they are essential for normal embryonic development (Moore et al., 2015; Plasschaert and Bartolomei, 2014). In 1984, androgenetic (two paternal pronuclei) and gynogenetic (two maternal pronuclei) mouse embryos were generated by transplanting pronuclei between one-cell-stage embryos. Here, uniparentally-derived embryos failed to complete normal embryogenesis (Barton et al., 1984; McGrath and Solter, 1984). These classic studies suggested that gene expression differences must exist between the maternally and paternally inherited chromosomes and that normal development requires both maternally and paternally expressed genes. Imprinted genes were unknown at the time. However, subsequent studies in mouse models identified imprinted genes (for the list of mouse imprinted genes see, http://www.mousebook.org/mousebook-catalogs/imprinting-resource) and illustrated that disruption of gene dosage or regulation of these genes could severely impair embryonic growth, explaining the phenomena observed in the androgenetic and gynogenetic embryos. Various human imprinting disorders have also been described, with individuals displaying growth, neurological, and metabolic clinical features (Kalish et al., 2014; Peters, 2014; Plasschaert and Bartolomei,

2014). This emphasizes the conserved importance of correct regulation and expression of imprinted genes for proper mammalian development.

1.1.1 Hypotheses on origins of genomic imprinting

Imprinted genes are conserved in mammals, and they have significantly expanded in the therian lineage of mammals such as marsupials and eutherians (placental mammals) (Renfree et al., 2013). Due to their complex nature of parental allele-specific regulation and subsequent monoallelic expression, imprinted genes are especially susceptible to various genetic/epigenetic challenges. Why, then, would mammals develop such a costly mechanism of gene expression that could make the organism more vulnerable to insults? To start addressing this question, it is worth reviewing the two widely accepted hypotheses on the evolution of genomic imprinting.

The parental-conflict theory proposes that each parental genome has conflicting "interests" in provisioning offspring. For example, paternally expressed genes prefer to promote the growth of embryos to increase their genetic fitness. On the other hand, maternally expressed genes try to suppress growth of embryos, allowing for more equal allocation of limited maternal reproductive resources across successive pregnancies. In support of this hypothesis, many paternally expressed imprinted genes such as *Igf2*, *Kcnq1ot1*, *Dlk1*, *Rasgrf1*, *Peg1*, *Peg3*, *Peg10*, *Rtl1*, and *Plagl1* promote growth, and the maternally expressed imprinted genes, such as *H19*, *Cdkn1c*, *Phlda2*, *Igf2r*, and *Grb10* suppress growth (Patten et al., 2014; Renfree et al., 2013).

Another hypothesis known as the maternal-offspring coadaptation theory proposes that genomic imprinting has evolved in the context of coordinating the maternal-offspring interactions to increase the fitness of offspring. The theory posits that monoallelic (compared to biallelic) expression of genes allows for a more rapid

adaptation of important traits for provisioning offspring, such as embryonic growth and maternal care. For example, the paternally expressed *Peg3* gene is important not only for proper maternal care and growth of the placenta by adult females, but also for regulating ability of neonates to suckle (Isles, 2009; Renfree et al., 2013). Thus, this gene might have evolved to be critical for facilitating the interaction between mom and offspring, leading to imprinted, and thus fine-tuned expression. This hypothesis is further supported by the fact that the majority of imprinted genes are expressed in placenta, a vital tissue that connects physiology between mom and fetus (Renfree et al., 2013).

Each theory proposes a slightly distinct view on the origins of imprinting. However, both theories share a common theme: imprinting must have evolved to facilitate coordination and/or adaption of expression of a subset of genes in response to the demands of complex biological processes required during mammalian development. These intriguing theories underscore the need to further probe the evolutionary perspective of imprinted genes at a molecular level. To this end, systematic investigation on functions and mechanisms of imprinted genes in various mammalian species will be valuable.

1.1.2 Regulation of *cis*-regulatory elements for genomic imprinting

Imprinted genes are typically found in clusters. Within a cluster, the parental-specific expression of imprinted genes is coordinately regulated by a *cis*-regulatory element, the imprinting control region (ICR). One hallmark feature of ICRs is parental-specific differential DNA methylation (Abramowitz and Bartolomei, 2012). Proper regulation of imprinted genes is highly dependent on the correct establishment, maintenance, and erasure of the differential DNA methylation at ICRs (Figure 1.2)

<u>Establishment</u>

Studies in the mouse germ cells have established that ICRs acquire sperm- or oocyte-specific DNA methylation pattern during gametogenesis (Figure 1.2) (Davis et al., 1999; Lucifero et al., 2004). In both male and female germline, the *de novo* DNA methyltransferase DNMT3a and its accessory protein DNMT3L are required for establishing DNA methylation at ICRs (Bourc'his and Bestor, 2004; Bourc'his et al., 2001; Kaneda et al., 2004; Kato et al., 2007). How these DNA methylation machinery proteins are specifically recruited to the ICRs is currently unclear.

One hypothesis states that transcription at the ICRs is required for DNA methylation establishment. Evidence to support this idea exists in both female and male germ lines. At the *Gnas* imprinted locus, truncation of an upstream transcript *Nesp* (that goes through the ICR of the locus) in the oocyte leads to loss of methylation at the locus (Chotalia et al., 2009). This suggests that transcription through the ICR is necessary for correctly establishing methylation at this locus. Transcripts crossing other maternally methylated ICRs are also found at the *Snrpn, Grb10, Igf2r, Impact, Kcnq1,* and *Zac1* imprinted loci (Chotalia et al., 2009; Mapendano et al., 2006). Similarly, transcription was detected in the male germ cells at the *H19/Igf2* locus, where the timing of transcription correlated with that of ICR methylation establishment (Henckel et al., 2012). However, the upstream signal for transcription in the germ cells as well as precise mechanism of how transcription affects ICR methylation establishment remain to be determined.

Maintenance

Following fertilization in early embryos, ICRs resist the dynamic DNA methylation reprogramming and preserve the parental-allele-specific methylation pattern in somatic cells (Figure 1.2). To this end, the maternal factor DPPA3 was shown to maintain DNA methylation at several ICRs by interacting with histone H3 lysine (K) residue 9 di-

methylation (H3K9me2) and/or by suppressing the activity of DNA demethylating ten-eleven translocation (TET) family enzymes (Bian and Yu, 2014; Nakamura et al., 2012). The zinc finger protein ZFP57, which interacts with TRIM28, was shown to protect ICRs from DNA demethylation (Li et al., 2008; Messerschmidt et al., 2014; Riso et al., 2016). The DNA methylation maintenance enzyme DNMT1 methylates newly replicated DNA, maintaining methylation at ICRs during cell divisions (Li et al., 1993).

In order to maintain the differentially methylated status of the ICRs, the hypomethylated allele needs to be protected from aberrantly gaining methylation in somatic cells. Activating post-translational histone modification marks seem to play major role in this regard (discussed below). Yet, one *trans* factor that carries out this function is the methylation-sensitive zinc-finger protein CTCF (Holwerda and de Laat, 2013). Inability to bind CTCF at the ICR of the *H19/Igf2* imprinted locus caused aberrant ICR hypermethylation (Engel et al., 2006). Mechanistically, a few groups proposed that CTCF can activate PARP1, which can add ADP-ribose groups to DNMT1 and inactivate the maintenance methyltransferase (Guastafierro et al., 2008; Yu et al., 2004; Zampieri et al., 2012). However, this argument needs to be revisited because the presence or absence of the ADP-ribolysated form of CTCF might be tissue-specific (Ideraabdullah et al., 2014).

Erasure

In order to establish the sex-specific methylation pattern in mature gametes, it is important that the established somatic ICR methylation is erased in primordial germ cells (PGCs) (Figure 1.2). During this process, both passive (methylation that is lost due to the absence of active DNMT1) and active mechanisms were shown to be involved. Specifically, TET1 and TET2 enzymes are necessary to actively demethylate ICRs at

multiple imprinted loci (Messerschmidt et al., 2014). To do this, TET proteins catalyze oxidation of methylated cytosine into hydroxymethylated cytosine, and possibly further oxidized species, and the base excision repair pathway is activated to further remove the oxidized forms of cytosine (Dawlaty et al., 2013; Hackett et al., 2013; Pastor et al., 2013). Studying ICR methylation erasure and re-establishment requires access to early (and limited) germ cells. Thus, most of the above findings were from mouse studies. Yet, recent studies in human prenatal germ cells illustrate remarkable similarity in DNA demethylation/re-methylation dynamics between the mouse and human germlines, emphasizing that the ICR reprogramming is a conserved fundamental process in mammalian development (Gkountela et al., 2015; Guo et al., 2015; Tang et al., 2015).

Histone modifications and genomic imprinting

In addition to DNA methylation, parental allele-specific histone modifications have been described at ICRs in both somatic and germ cells (Delaval et al., 2007; Singh et al., 2013; Stewart et al., 2015; Verona et al., 2008). Increasing evidence suggests that histone modification composition can affect the extent of DNA methylation at ICRs (Abramowitz and Bartolomei, 2012). For example, it was shown that oocytes lacking KDM1B, a H3K4 demethylase, failed to establish DNA methylation at several ICRs (Ciccone et al., 2009). This is consistent with the well-established antagonistic relationship between DNA methylation and the activating histone marks such as H3K4me2 and H3K4me3 at both imprinted and non-imprinted loci (Meissner et al., 2008; Ooi et al., 2007; Singh et al., 2013; Stewart et al., 2015). Importantly, Hajkova *et al*. illustrated that extensive histone modification erasure occurs in PGCs (Hajkova et al., 2008), suggesting that epigenetic reprogramming during this stage also occurs at a chromatin level. The mechanisms by which histone modifications are deposited or

removed at ICRs are currently unknown. However, it is quite evident that proper establishment and erasure of histone modifications at ICRs is equally vital as that of DNA methylation for correct regulation of imprinting. Indeed, various imprinting disorders are associated with altered histone modification profiles at ICRs (Nativio et al., 2011).

Which epigenetic mark (i.e. DNA methylation or histone modifications) works as the “primary” signal for distinctly marking each parental allele to regulate imprinted gene expression is an active area of research in the field. This could be locus-dependent. Overall, understanding the relationship between the two epigenetic modifications in regulating genomic imprinting will tremendously contribute to the field of imprinting.

1.1.3 Evolution and conservation of imprinting control regions (ICRs)

Imprinted genes are conserved in mammals and differentially methylated ICRs play fundamental roles in genomic imprinting. This has led researchers to elucidate the molecular bases of the evolution of imprinted genes by examining orthologous ICR sequences between different mammalian species. Comparative sequence analyses conducted by Suzuki *et al*. illustrated that novel CpG-rich sequences (which form the now called ICRs) emerged at different time points during mammalian evolution in various imprinted regions. These sequences emerged predominantly during eutherian evolution following the marsupial-eutherian split, suggestive of the evolutionary timeline during which functional imprinted genes were established (Suzuki et al., 2011).

One potential mechanism by which the novel CpG-rich sequences (or ICRs) are gained is via retrotransposition. This hypothesis stems from the fact that these sequences are 1) similar to transposable elements in that they are enriched with CpG sites and 2) subject to DNA methylation in the gametes, a mechanism reminiscent of the conserved epigenetic host defense mechanism against foreign DNA (e.g., transposable

elements) in the germ cells (Barlow, 1993; McDonald et al., 2005). In fact, previous reports have found evidences of retrotransposition of several imprinted genes including *Peg10*, *Mcts2*, *Nap1L5*, *Inpp5f_v2*, *U2af1-rs1*, and *Nnat*. These studies lead to the speculation that ICRs likely emerged at the same time as the retrotransposition of each imprinted gene (Suzuki et al., 2011). However, not all currently identified ICRs display evidence of retrotransposition, suggesting that other unknown mechanisms could promote acquisition of these regulatory elements in imprinted regions.

Interestingly, after the novel CpG-rich sequences in imprinted regions were acquired, some underwent genetic and/or epigenetic changes over time. For instance, the CpG-rich sequences of *Slc38a4*, *Snrpn*, and *Gnas* became differentially methylated only in the eutherian lineage (thus fulfilling the prerequisites of being designated as ICRs) although the CpG-rich sequences were established earlier. In addition, the number of CpG sites within the orthologous ICR sequences of *Grb10* increased during mammalian evolution, while overall sequence homology was maintained (Suzuki et al., 2011). These observations suggest that some selective pressure could have acted on ICRs and/or imprinted regions, contributing to their evolution at a molecular level.

Consistent with the fact that imprinted genes and ICRs have greatly expanded during eutherian evolution, mouse and human exhibit extensive conservation of imprinted genes by sharing key features of imprinting and spatial organization of *cis*-regulatory elements. However, ICRs are often divergent between human and mouse, raising an interesting question of whether the diverged ICR sequences have any functional species-specific significance. One approach that can be exploited to address this question is to substitute the ICR sequence of one species with that of another

species at the orthologous locus. We took this strategy in specifically probing the *H19*/*Igf2* imprinted locus (described in detail below), as discussed in Chapter 2.

1.2 Imprinted clusters on mouse distal chromosome 7/human 11p15

Two highly conserved imprinted clusters—*H19*/*Igf2* and *Cdkn1c*/*Kcnq1ot1* loci—are located in mouse distal chromosome 7 which is syntenic to the human 11p15 region (Figure 1.3 and Figure 1.4). These chromosomal regions epitomize genomic imprinting for various reasons: 1) Both maternally and paternally methylated ICRs are found, 2) the two major mechanisms of imprinting—insulator model and long non-coding RNA (lncRNA) model—are used, 3) genetic/epigenetic alterations affecting the ICRs are associated with major growth-related imprinting disorders. Thus, various scientific endeavors were pursued to elucidate genomic imprinting in these regions. Most notably, these imprinted regions are involved in growth regulation in both normal and pathological contexts. Therefore, mechanisms of imprinting at the *H19*/*Igf2* and *Cdkn1c*/*Kcnq1ot1* loci as well as their involvement in growth regulation are discussed in detail below.

1.2.1 *H19/Igf2* imprinted locus

H19

H19 is a maternally expressed ~2.5kb lncRNA (Bartolomei et al., 1991) and is one of the few imprinted genes conserved in marsupials. Although the extent of sequence similarity between the marsupial and eutherian *H19* gene is very low, the exonal structure is highly conserved across therians (Figure 1.5A). In fact, *H19*/*Igf2* is the most ancient imprinted cluster identified to date (Smits et al., 2008). Despite the well-known conservation of the gene, functions of *H19* in different tissues/physiological contexts seem to vary and remain to be further investigated. *H19* is abundantly expressed in mouse embryonic endodermal and mesodermal lineage tissues as well as

in placenta, but expression rapidly declines after birth (Bartolomei et al., 1991; Milligan et al., 2000). The best characterized function of *H19* is its role in growth suppression during fetal and placental development; mouse models lacking *H19* display embryonic and placental overgrowth with no other apparent phenotypes (Ripoche et al., 1997; Schmidt et al., 1999).

The mechanism by which *H19* lncRNA regulates growth remains largely unknown. Yet, one recent study proposed that *H19* suppresses placental growth via maternally expressed microRNA (miR)-675 encoded within the first exon of *H19* (Figure 1.5A) (Keniry et al., 2012). Here, two distinct miRs—miR-675-5p and miR-675-3p—are produced (Figure 1.5B). miR-675 is most highly expressed in mouse late gestation placenta (its expression peaks around embryonic day (E) 19.5) while it is lowly expressed in other fetal tissues (Keniry et al., 2012). Such a dissimilar spatiotemporal expression pattern between *H19* and miR-675 suggests that despite sharing the same transcription unit and the seemingly overlapping role in growth suppression, expression of each factor might be regulated and function via different mechanisms. Keniry *et al*. suggests RNA-binding protein HuR as one factor that regulates processing of miR-675 from *H19* (Keniry et al., 2012). This study also demonstrated that overexpression of miR-675 in various embryonic and extra-embryonic cell lines reduced cell proliferation (Keniry et al., 2012). However, testing the role of miR-675 independent of *H19* needs to be carried out *in vivo* to dissect the potentially distinct role of each factor in growth regulation during development.

H19 has also been suggested to regulate a network of imprinted genes (known as the imprinted gene network, IGN) in *trans* to control embryonic growth (Gabory et al., 2009; Varrault et al., 2006). This was hypothesized because modulation of *H19* altered

expression of other growth-related imprinted genes such as *Igf2*, *Dlk1*, *Rtl1*, *Gnas*, *Peg3*, *Slc38a4, Cdkn1c,* and *Igf2r* (Gabory et al., 2009). The extent to which the changes in the IGN gene expression is directly/indirectly regulated by *H19* is unclear. Monnier *et al*. showed that *H19* can physically interact with the methylated CpG binding protein MBD1 and repress a subset of IGN genes by modulating H3K9me2 level *in vitro* (Monnier et al., 2013). Yet, this experiment requires validation *in vivo*. Moreover, whether such a change in imprinted gene expression is merely a secondary effect caused by changes in cell composition and/or number needs to be validated at a single cell level. Nevertheless, the idea of coordinate regulation of imprinted genes is gaining attention, as it has been described during muscle regeneration and lung stem cell self-renewal as well (Al Adhami et al., 2015; Patten et al., 2016; Zacharek et al., 2011). Perhaps this concept fits well with the original hypotheses on genomic imprinting as a way to fine-tune complex gene expression in mammals.

Igf2

Igf2 is a paternally expressed fetal growth factor. Similar to *H19*, *Igf2* is ubiquitously expressed in embryonic and placental tissues (Engström et al., 1998). IGF2 binds to the non-signaling receptor IGF2R (which is also imprinted) with high affinity, although it can also bind to signaling receptors such as IGF1R and the insulin receptor with lower affinity (Bergman et al., 2013). IGF2R acts as a growth suppressor by sequestering and degrading circulating IGF2 (Scott and Weiss, 2000), whereas IGF2 binding to IGF1R promotes growth during fetal development (Baker et al., 1993). The fact that IGF2 plays a pivotal role in embryonic growth is evident in the *Igf2* knock-out mouse models, where mice display embryonic and placental growth restriction with no other apparent phenotype (DeChiara et al., 1990; DeChiara et al., 1991).

Regulation of imprinting at the H19/Igf2 locus

Imprinting at the *H19*/*Igf2* locus is regulated by a model known as the insulator model (Figure 1.3). This model illustrates that an insulator/enhancer blocker is formed at the ICR in an allele-specific manner, preventing the interactions between enhancers and promoters. Previous studies demonstrated that *H19* and *Igf2* share a set of conserved mesodermal and endodermal enhancers located downstream of *H19* (Ishihara et al., 2000; Kaffer et al., 2001; Leighton et al., 1995a). The ICR at this locus, called IC1, is located between *H19* and *Igf2*. On the maternal allele, the unmethylated IC1 forms an insulator by interacting with CTCF (Bell and Felsenfeld, 2000). This prevents the interaction of the *Igf2* promoters with the downstream enhancers, silencing *Igf2* expression; because the *H19* promoter is accessible to the enhancers, only *H19* is expressed on the maternal allele. On the paternal allele, IC1 is DNA methylated and blocks CTCF binding; thus, the insulator does not form and *Igf2* is expressed. The IC1 also plays a role in silencing paternal *H19* expression, by spreading methylation across the *H19* promoter (Tremblay et al., 1997).

Various mouse models that carry mutations at IC1 have supported the essential role of DNA methylation and CTCF binding for proper insulator function of IC1. When the paternal IC1 was mutated at CpG sites to deplete DNA methylation, ectopic binding of CTCF was observed on the paternal allele, leading to biallelic *H19* expression and reduced *Igf2* expression (Engel et al., 2004). When the CTCF binding sites were deleted on the maternal IC1 to disrupt the insulator, biallelic *Igf2* expression and reduced *H19* expression was observed (Engel et al., 2006). These studies demonstrate that any insults leading to aberrant DNA methylation or CTCF binding at the IC1 can disrupt imprinted expression at the *H19/Igf2* locus.

Other *trans*-factors have also been proposed to maintain proper insulator function of IC1, although these hypotheses mostly remain controversial. One such factor is ZFP57, whose binding motifs reside in both mouse and human IC1. ZFP57 was shown to play a role in maintaining DNA methylation at imprinted loci such as *Dlk1-Dio3*, *Peg1*, *Peg3*, and *Nnat* (Li et al., 2008). Conflicting results were presented by two studies: IC1 methylation was unaffected in ZFP57-deficient mice yet affected in the *zfp57*-null mouse embryonic stem cells (ESCs) (Li et al., 2008; Riso et al., 2016). In addition, patients that have mutations in *ZFP57* do not display methylation defects at IC1 (Mackay et al., 2008). Thus, further studies are warranted to assess the role of ZFP57 in IC1 insulator function.

Pluripotency factors such as OCT4 and SOX2 are also proposed as candidates for regulating IC1 function. OCT4-and SOX2-binding sites are present at both mouse and human IC1 (Shmela and Gicquel, 2013). OCT4-binding sites at the mouse IC1 were shown to be important for maintaining hypomethylated state of IC1 in mouse embryonal carcinoma cell line (Hori et al., 2002). However, a mouse model that harbors 0.9kb IC1 fragment deletion (which also deleted the OCT4-binding sites) showed no perturbation of imprinting at the locus (Ideraabdullah et al., 2011). Interestingly, a mouse model with endogenous OCT4 binding site mutations at the IC1 displayed partial gain of methylation during post-zygotic stages, without affecting monoallelic *H19* and *Igf2* expression (Zimmerman et al., 2013). Therefore, the extent to which OCT4-and/or SOX2-binding sites contribute to the insulator function of IC1 awaits further investigation.

H19/Igf2 locus is the only imprinted locus that uses a well-defined insulator model of imprinting. Although CTCF binding sites have been described at other imprinted regions including the *Grb10*, *Rasgrf1*, *Dlk1-Dio3*, and *Cdkn1c/Kcnq1ot1* loci

(Lin et al., 2011; Plasschaert and Bartolomei, 2014; Yoon et al., 2005), it is unknown whether these loci utilize the similar insulator model as the *H19/Igf2* locus.

1.2.2 *Cdkn1c/Kcnq1ot1* imprinted locus

The *Cdkn1c/Kcnq1ot1* imprinted locus includes at least 8-10 maternally expressed protein coding genes (Figure 1.4). Some of these genes are ubiquitously imprinted whereas others are imprinted specifically in placenta. A few genes implicated in growth regulation are discussed below.

Cdkn1c

Cdkn1c is a maternally expressed cyclin-dependent kinase inhibitor. The gene is expressed and imprinted in derivatives of all three germ lineages during mouse embryonic development, primarily in cells that are exiting the cell cycle (Tunster et al., 2011). *Cdkn1c* is a major growth suppressor in the *Cdkn1c/Kcnq1ot1* imprinted cluster. Mice lacking *Cdkn1c* displayed embryonic and placental overgrowth during mid-late gestation (Tunster et al., 2011). Overexpression of *Cdkn1c* alone in transgenic mice could lead to embryonic lethality. In the same study, the level of the fetal growth factor *Igf1* transcript was concomitantly altered upon changes in the dosage of *Cdkn1c* (Andrews et al., 2007), suggesting that growth regulation of *Cdkn1c* could in part be achieved via *Igf1*. Other suggested roles of *Cdkn1c* during development include cell differentiation, migration, and modification of actin cytoskeleton (Andrews et al., 2007; Hatada and Mukai, 1995; Tunster et al., 2011).

Ascl2 and *Phlda2*

Ascl2 and *Phlda2* are maternally expressed genes that are exclusively imprinted and/or preferentially expressed in placenta. *Ascl2* is a transcription factor that is

essential for cell proliferation in placenta (Guillemot et al., 1995), whereas *Phlda2* is a cytoplasmic protein that negatively regulates placental growth (Frank et al., 2002). Because placenta is an essential organ for maternal-offspring nutrient exchange (Frost and Moore, 2010), proper regulation of placental development is indispensable for normal embryonic growth.

Kcnq1ot1 and the regulation of imprinting at the Cdkn1c/Kcnq1ot1 locus

In some imprinted regions, including the *Cdkn1c/Kcnq1ot1*, *Igf2r*, and *Snrpn* loci, parental allele-specific lncRNAs have been identified and were shown to play a role in silencing genes in *cis* (Lee and Bartolomei, 2013). This mechanism of imprinting is known as the lncRNA model and is more widely used than the insulator model. In this model, lncRNAs are expressed from the ICRs and this expression depends on the methylated status of the ICRs (i.e. when ICR is methylated, lncRNA is silenced; when unmethylated, lncRNA is expressed) (Figure 1.4). Subsequently, lncRNAs can silence the genes in *cis* by interfering with transcription of the nearby genes or by promoting repressive chromatin environment at the imprinted locus (Lee and Bartolomei, 2013).

Kcnq1ot1 is a ~91kb lncRNA expressed from the paternal allele that has no known physiological function (Kanduri, 2011). Its transcription initiates from the ICR of the *Cdkn1c/Kcnq1ot1* locus, called IC2, in an antisense orientation. IC2 is located in intron 10 of the *Kcnq1* gene and is methylated on the maternal allele; thus, *Kcnq1ot1* is silenced on the maternal allele and the *cis*-genes are expressed (Kanduri, 2011).

Although *Kcnq1ot1* is ubiquitously expressed, its mode of action seems to be tissue-specific (i.e. placenta-specific and ubiquitously imprinted genes seem to be regulated differently) (Umlauf et al., 2004; Wagschal et al., 2008). Previous studies

proposed that *Kcnq1ot1* can perform bi-directional silencing on the paternal allele by modulating histone modification enrichment at the placenta-specific imprinted genes at the locus. These genes are enriched with the paternal allele-specific H3K27me3 and H3K9me2 (Lewis et al., 2004; Umlauf et al., 2004). In the *Kcnq1ot1* truncation mutant, enrichment of H3K27me3 was affected at these sites (Pandey et al., 2008). Coimmunoprecipitation and RNA fluorescent in situ hybridization (FISH) experiments suggested that *Kcnq1ot1* potentially interacts with various histone modifiers such as G9A (H3K9 methyltransferase), PRC2 complex (catalyzes H3K27 methylation), and RNF2 (ubiquitin E3 ligase) (Pandey et al., 2008; Terranova et al., 2008). Consistently, when G9A was knocked out, partial loss of H3K9me2 and H3K9me3 at the locus was observed (Wagschal et al., 2008). These results suggest that *Kcnq1ot1* regulates imprinting in placenta by interacting with various histone modifiers.

On the other hand, *Kcnq1ot1* seems favor a different epigenetic modification—DNA methylation—in silencing the ubiquitously imprinted genes at the locus, such as *Cdkn1c* and *Slc22a18* (Lewis et al., 2004). To support this idea, somatically established differentially DNA methylated regions (DMRs) are only found around *Cdkn1c* and *Slc22a18*, but not at the placenta-specific imprinted genes (Lewis et al., 2004). Mohammad *et al*. illustrated that *Kcnq1ot1* can recruit DNMT1 to these DMRs to maintain methylation (Mohammad et al., 2010). In addition, both *Cdkn1c* and *Slc22a18* were biallelically expressed in *Dnmt1*-null embryos and placentas. Notably, monoallelic expression of the placenta-specific imprinted genes *Cd81, Osbpl5,* and *Tssc4* was barely affected by loss of DNMT1, suggesting that imprinting in placenta minimally relies on DNA methylation (Lewis et al., 2004).

It is unlikely that all lncRNA imprinting models function via altering chromatin environment. For example, *Airn* is a paternally expressed antisense lncRNA at the *Igf2r* imprinted locus. One of the *cis* genes *Airn* silences is the growth regulator *Igf2r*. Latos *et al*. showed that *Airn* silences *Igf2r* by transcriptional interference, by reducing recruitment of RNA polymerase II to the *Igf2r* promoter (Latos et al., 2012). Thus, in this case, the act of transcription *per se* is more important for imprinting than the lncRNA transcript itself.

In conclusion, the lncRNA model of imprinting seems to be more versatile in its mechanisms of action and is employed by more imprinted loci. Further studies should address questions such as how lncRNAs find their targets, how lncRNAs interact with epigenetic modifiers or transcription machinery proteins, and how lncRNA-driven tissue-specific imprinting is established and maintained.

1.3 Human disorders associated with 11p15

Mouse models have held great value for investigating mammalian imprinting mechanisms. Nevertheless, the recent identification of various alterations at the 11p15 region in human imprinting disorder patients has raised new questions about how imprinting functions in human health and disease. The ability to model the newly discovered alterations will provide additional insights into human imprinting mechanisms and potentially assist in therapeutic advances for these disorders. Furthermore, comparing the phenotypes of the patients to those of mouse models with similar mutations provides clues about the extent to which imprinting mechanisms are conserved between the two species.

As mentioned above, the human 11p15 region is essential for growth regulation. Consistently, two major growth-related imprinting disorders—Beckwith-Wiedemann

syndrome (BWS) and Silver Russell syndrome (SRS)—are associated with misregulation of imprinting in this region. Clinical features and molecular etiologies of both disorders are discussed below.

1.3.1 Clinical features and occurrence rate of BWS and SRS

BWS (OMIM 130650) is a pediatric overgrowth disorder with an estimated frequency of 1/10,500 per live births, affecting males and females equally, making it the most common imprinting disorder (Choufani et al., 2013; personal communication with Jennifer Kalish, MD, PhD at Children's hospital of Philadelphia (CHOP)). Major clinical features include enlarged tongue, hemihyperplasia (asymmetric overgrowth), and abdominal wall defects (Weksberg et al., 2010). Notably, some BWS individuals develop embryonal tumors, most commonly Wilms tumor (kidney cancer) and hepatoblastoma (liver cancer) (Choufani et al., 2013).

SRS (OMIM 180860) is a rarer pediatric growth failure disorder with more than 400 cases being reported since its first description in 1953 (Silver et al., 1953; Russell, 1954; Ishida, 2016). Major clinical features include intrauterine growth restriction, hemihypoplasia (asymmetric undergrowth), and relative macrocephaly (Ishida, 2016).

In both BWS and SRS, the reported occurrence rate could be an underestimation. Improved sensitivity of molecular diagnostic techniques used in the clinic to analyze DNA methylation aberration, chromosomal rearrangements, and percent mosaicism of affected cells has increased the chances of detecting understated molecular signatures in the patients. In addition, the spectrum of clinical phenotypes is now better characterized, which enables clinicians to recognize individuals with subtler clinical features (personal communication with Jennifer Kalish, MD, PhD at CHOP). These

improvements in the medical setting are invaluable to the patients and their families and widen opportunities to dissect human imprinting mechanisms.

BWS and SRS patients display a wide spectrum of clinical phenotypes (Ishida, 2016; Weksberg et al., 2010). This may occur either as a consequence of the mosaic distribution of affected cells or the genetic background of the individuals (Beygo et al., 2013; Kalish et al., 2013; Kannenberg et al., 2012). Thus, studies of imprinting mechanisms in the context of human disorders need to control for the mosaicism and genetic background in the patients. One way such issues can be addressed is by deriving patient-specific induced pluripotent stem cells (iPSC) lines, as discussed in Chapter 3.

1.3.2 Molecular etiology of BWS

Various BWS-associated molecular alterations have been described, including genetic and epigenetic alterations and chromosomal abnormalities (Figure 1.6) (Soejima and Higashimoto, 2013; Weksberg et al., 2010).

Alterations in the *CDKN1C/KCNQ1OT1* locus are prevalent among BWS individuals. In fact, the most common alteration found in BWS population (~50%) is IC2 hypomethylation (Figure 1.6). Because IC2 is never completely hypomethylated in each patient, the epimutation is assumed to occur mosaically, which is a common characteristic of majority of epimutations found in imprinting disorders (Soejima and Higashimoto, 2013; Ishida, 2016). IC2 hypomethylation is accompanied by loss of H3K9 methylation at IC2, biallelic *KCNQ1OT1* expression, and loss of *CDKN1C* expression (Diaz-Meyer et al., 2003; Higashimoto et al., 2003). This phenotype can be explained by the *Cdkn1c/Kcnq1ot1* imprinting mechanism that was elucidated in mouse models, suggesting that a similar imprinting mechanism is used in humans. The overgrowth

phenotype found in these patients is most likely driven by loss of *CDKN1C*, as various *CDKN1C* mutations leading to loss of function of the protein are also found in small subset (~5%) of BWS patients (Hatada et al., 1996; Romanelli et al., 2010).

Although alterations involving the *H19/IGF2* locus are less common, they are associated with increased risk of tumor development. About 2-7% of BWS cases display IC1 hypermethylation (Soejima and Higashimoto, 2013). Notably, an increasing number of studies are finding genetic alterations associated with IC1 hypermethylation (Figure 1.6 and Figure 1.7). One type of mutation is IC1 microdeletions that remove different sequences and numbers of CTCF binding sites (CTS). In these patients, when the mutation is maternally inherited, *IGF2* is biallelically expressed and *H19* expression is reduced, suggestive of a loss of insulator function (Beygo et al., 2013; Prawitt et al., 2005; Sparago et al., 2004). These phenotypes are reminiscent of the mouse models with partial deletions of the IC1 sequence. In these models, IC1 was hypermethylated at the remaining IC1 and biallelic *Igf2* expression was observed upon maternal inheritance of the mutant allele (Engel et al., 2006; Thorvaldsen et al., 1998). These results suggest that the imprinting mechanism at the *H19/IGF2* locus is largely conserved between human and mouse.

Point mutations of the OCT4-SOX2-binding motif have also been identified among BWS individuals with IC1 hypermethylation (Figure 1.7). Maternal transmission of the mutant alleles is associated with clinical phenotypes in the patients (Demars et al., 2010; Habib et al., 2014; Poole et al., 2012). As mentioned previously, studies investigating the role of the mouse OCT4-binding sites in the insulator function of IC1 presented ambiguous results. Similarly, inconsistent arguments were made regarding the role of human OCT4-binding sites in the function of IC1. Mutating the OCT4-binding

sites on human IC1 minimally affected the enhancer-blocking and CTCF-binding activities of IC1 *in vitro* (Beygo et al., 2013). In contrast, human IC1 sequence with OCT4-binding site mutation impaired the ability of IC1 to bind human OCT4/SOX2 proteins *in vitro*, suggesting that the binding of these proteins has a functional role at IC1 (Demars et al., 2010). Overall, the contribution of OCT-SOX-binding sites to the insulator function of IC1 remains unknown in both mouse and human. However, it is possible that 1) the ability of OCT4-SOX2-binding motifs to control IC1 methylation depend on the non-conserved sequence of IC1 between mouse and human and thus be species-specific 2) OCT4 mutations may predispose patients to BWS via unidentified mechanism (Zimmerman et al., 2013).

Lastly, paternal uniparental isodisomy of chromosome 11 (pUPD11) is found in about 20% of BWS cases and normally includes both *H19/IGF2* and *CDKN1C/KCNQ1OT1* loci. pUPD11 occurs when part or entire of the maternal chromosome 11 is lost in a single cell. To repair the missing chromosome or chromosome portion, a duplication of the corresponding region of the paternal chromosome occurs. This rescue event leads to both copies of chromosome 11 having the paternal epigenotype, resulting in IC1 hypermethylation, IC2 hypomethylation, increased *IGF2* expression, and reduced *H19* and *CDKN1C* expression (Kalish et al., 2014)) (Figure 1.8). The majority of pUPD11 BWS cases display mosaicism, indicating that these alterations arise post-zygotically (Kalish et al., 2014). Interestingly, pUPD11 patients are more predisposed to tumor development (Kalish et al., 2014). Despite being one of the common origins of BWS, no models to study pUPD11 exist in the field. This is largely due to the difficulty of engineering such chromosomal lesions as well as the

mosaic nature of UPD in patient samples. In Chapter 3, we describe a human cell-based model system that can be used to investigate pUPD11 and BWS.

1.3.3 Molecular etiology of SRS

The most common alteration associated with SRS is IC1 hypomethylation (Figure 1.6) (Ishida, 2016). Given the established model of imprinting at the *H19/Igf2* locus in mouse, this epimutation is proposed to reduce *IGF2* expression and increase *H19* expression. Indeed, a mouse model depleted of methylation at IC1 had biallelic *H19* expression, reduced *Igf2* expression, and 40% reduction in the size of the animals (Engel et al., 2004). Consistently, Gicquel *et al*. observed that patients with IC1 hypomethylation exhibited reduced *IGF2* and biallelic *H19* expression (Gicquel et al., 2005). However, results from other human studies have led to ambiguous conclusions about the exact mechanisms underlying SRS with IC1 hypomethylation. For example, Azzi *et al*. did not observe difference in *IGF2* expression between IC1 hypomethylation and unaffected patients' fibroblasts. Moreover, total *H19* expression level did not correlate with the degree of IC1 methylation (Azzi et al., 2014). Heckmann *et al*. did not detect differences in IGF2 protein secretion nor *H19* expression between IC1 hypomethylation and unaffected fibroblasts; instead, cells with IC1 hypomethylation exhibited aberrantly expressed genes involved in cell proliferation, cell cycle control, and timing of mitosis (Heckmann et al., 2015). Such discrepancies between human studies could be due to mosaic nature of the epimutation as well as the use of disease-irrelevant tissues, such as blood and fibroblasts, where *H19* and *IGF2* are lowly expressed.

Maternal UPD of chromosome 7 (mUPD7) accounts for ~10% of SRS cases (Figure 1.6) (Bartholdi et al., 2009). mUPD7 encompasses imprinted genes such as *GRB10*, *CPA4, MEST*, *KLF4, MEST1T1,* and *COPG21T1* (Ishida, 2016). However, no

known single mutation of any of these genes has been identified to date, although possible involvement of epimutations cannot be excluded (Ishida, 2016). Of note, maternally expressed *Grb10* suppresses growth in the mouse (Plasschaert and Bartolomei, 2014). In study by Leach *et al*., individuals with mUPD7 in which *GRB10* was excluded from the duplicated region, did not display SRS growth failure phenotypes; this implies that *GRB10* might be involved in pathogenesis of SRS (Leach et al., 2007).

1.4 Challenges in studying imprinting mechanisms

Mouse models are extremely advantageous in investigating imprinting mechanisms because parent-of-origin transmission of an imprinted allele can be tested. Moreover, access to early germ cells such as PGCs allows monitoring of epigenetic reprogramming at ICRs, the most essential aspect of imprinting regulation. However, mouse models with endogenous ICR mutations often do not fully recapitulate human phenotypes associated with mutations at the orthologous locus. Various *Cdkn1c* loss of function mouse models do not present neonatal overgrowth phenotype of BWS (Tunster et al., 2011). A mouse model that carries 1.3kb deletion at IC1, generated to model IC1 microdeletions in human, exhibits biallelic *Igf2* expression with no changes in IC1 methylation (Ideraabdullah et al., 2014). Furthermore, biallelic *Igf2* expression is only observed in tissues of mesodermal origin (Ideraabdullah et al., 2014). Imprinting mechanisms seem to be generally conserved between mouse and human. However, it is possible that across evolution from mouse to human, certain aspects of imprinting have diverged. Tunster *et al.* speculate that differences in the reproductive strategies (i.e. multiparous in mouse and singleton pregnancy in human) might have driven the divergence (Tunster et al., 2011). Thus, mouse models alone might not be sufficient to fully comprehend human imprinting mechanisms.

As a complementary approach, various studies were conducted using patient samples to investigate imprinting mechanisms and/or disease etiology. However, human studies have led to varying conclusions. Such discrepancy can result from 1) the use of blood and/or fibroblasts samples that are often irrelevant to disease (by expressing genes of interest at a very low level), 2) mosaic nature of the genetic mutations or epimutations. In line with this idea, studies have shown that the degree of DNA methylation alterations in BWS and SRS can be tissue-, cell-, and CpG site-specific, regardless of presence of genetic lesions (Beygo et al., 2013; Kannenberg et al., 2012). Therefore, model systems in which mosaicism can be controlled in a disease-relevant cell types are best suited to investigate mechanisms of imprinting.

The overall goal of this dissertation is to develop and explore model systems to study imprinting mechanisms. We have developed both *in vivo* and *in vitro* models with initial interest in modeling human imprinting mechanisms, focusing on the human 11p15 imprinted loci. Beyond serving as platforms to study imprinting mechanisms, these models allowed us to speculate on the evolutionary perspective of imprinting as well as epigenetic vulnerability in cell culture models.

Chapter 2 describes an *in vivo* mouse model where human IC1 sequence replaces the orthologous mouse sequence. We find that the human and mouse imprinting mechanism at the *H19/IGF2* locus has partially diverged. We also propose that this mouse model may serve to study mechanisms of IC1 hypomethylation associated with SRS. Chapter 3 describes an iPSC model derived from the fibroblasts of pUPD11 patients with BWS. These cell lines display the expected and stable epigenetic signatures at the pUPD11-relevant region, making them suitable models to study mechanisms underlying pUPD11 leading to BWS. However, we find that one imprinted

locus that frequently exhibits loss of imprinting in other iPSC models is similarly misregulated in our cell lines, although the significance of this phenotype is unclear.

Importantly, both models overcome issues related to mosaicism: the mouse model displays full penetrance of the epigenetic/genetic phenotype, and the iPSC lines are clonally-driven. Moreover, cell types of interest are readily accessible/can be derived from both models. Therefore, the work in this thesis emphasizes the utility of both mouse/human as well as *in vivo* and *in vitro* complementary approaches in studying imprinting mechanisms.

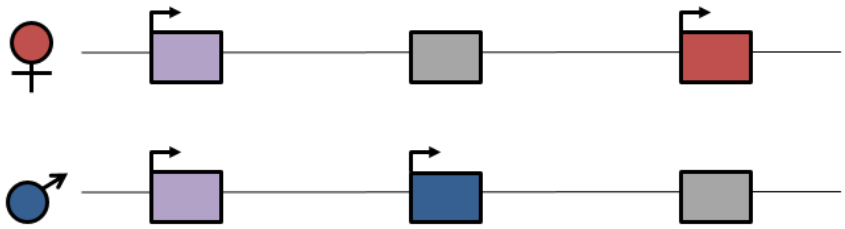

Figure 1.1 Genomic imprinting. Majority of the mammalian genes (purple boxes) are expressed from both parental alleles. However, imprinted genes (red and blue boxes) are expressed in a monoallelic, parent-of-origin specific manner. The blue box represents a paternally expressed imprinted gene, and the red box represents a maternally expressed imprinted gene. Expression is indicated by arrow, and silenced genes are illustrated in grey boxes. The parent-of-origin of the allele is indicated with a female(♀) or a male (♂) symbol on the left.

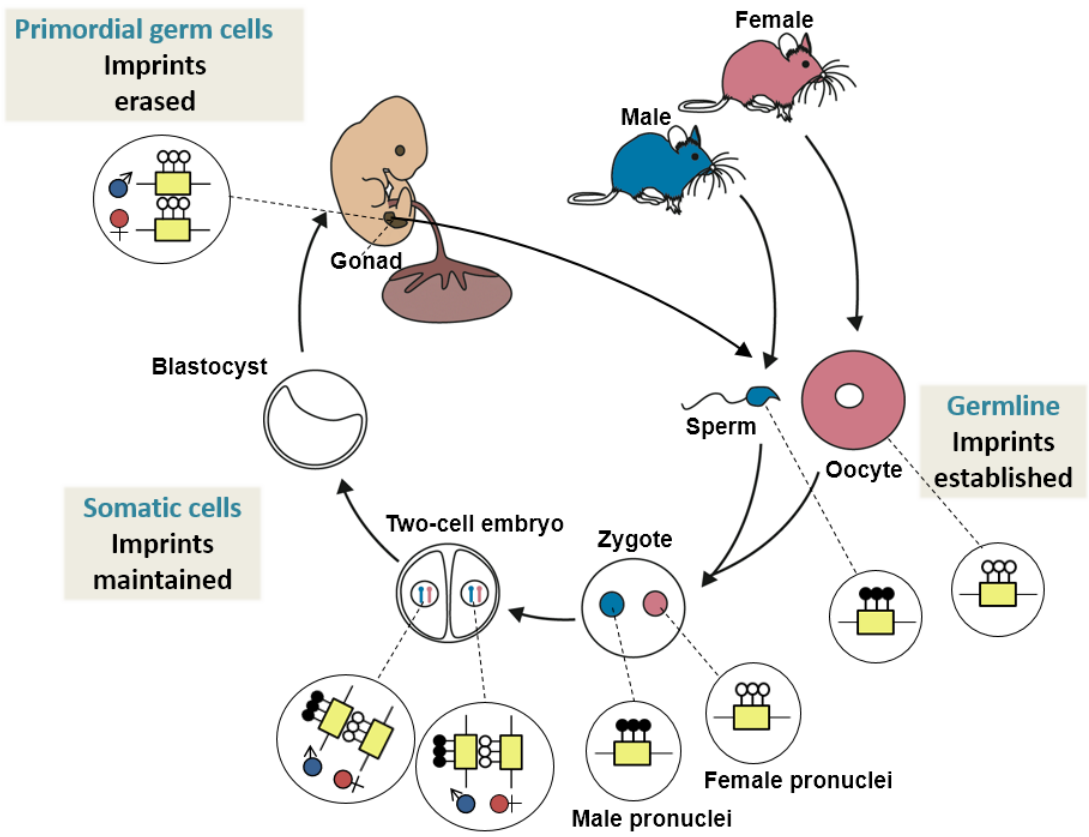

Figure 1.2 DNA methylation reprogramming at ICRs. The figure illustrates a scheme for a paternally methylated ICR (yellow box). During germ cell development, sex-specific DNA methylation pattern (filled lollipops represent methylated CpGs; empty lollipops represent unmethylated CpGs) is established at the ICR. Following fertilization, the parental-allele specific ICR methylation is maintained in somatic cells; the parent-of-origin of the ICR is indicated with a female(♀) or a male (♂) symbol next to the ICR in diploid nuclei. In the primordial germ cells (PGCs) of a growing embryo, somatic methylation pattern is erased, allowing re-establishment of a sperm- or oocyte-specific methylation at the ICR. The figure is adapted from Weaver *et al*. (Weaver et al., 2009)

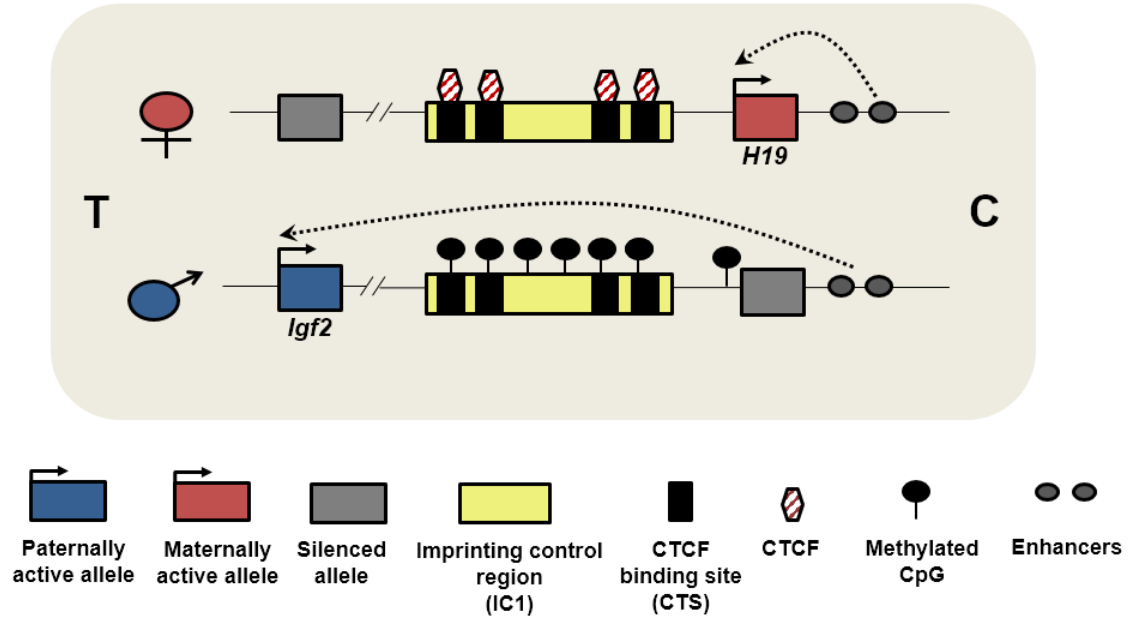

Figure 1.3 Insulator model of imprinting at the *H19/Igf2* locus in mouse. On the maternal allele (♀), CTCF binds to the unmethylated IC1, *Igf2* expression is blocked, and *H19* is expressed. On the paternal allele (♂), the IC1 is methylated, CTCF does not bind, *Igf2* is free to interact with the downstream enhancers and is expressed; *H19* is silenced due to methylation at its promoter. Centromeric (C) and telomeric (T) ends are indicated. Not drawn to scale.

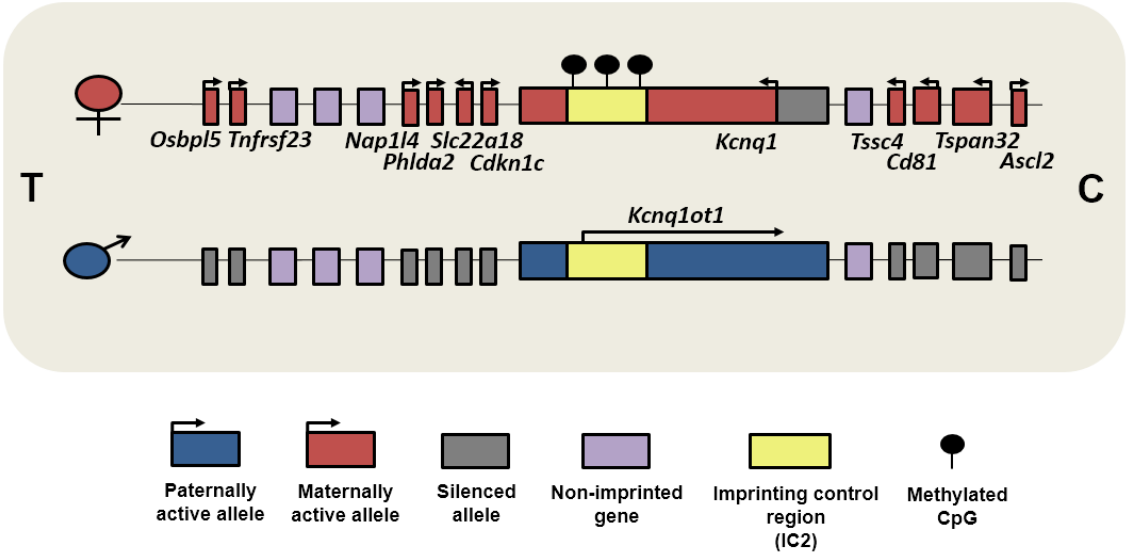

Figure 1.4 LncRNA model of imprinting at the *Cdkn1c/Kcnq1ot1* locus in mouse. On the maternal allele (♀), *Kcnq1ot1* is not expressed due to methylated IC2; thus, adjacent imprinted genes are expressed. On the paternal allele (♂), unmethylated IC2 allows the expression of *Kcnq1ot1; Kcnq1ot1* silences genes in *cis* bidirectionally. Only imprinted genes are labeled. Centromeric (C) and telomeric (T) ends are indicated. Not drawn to scale.

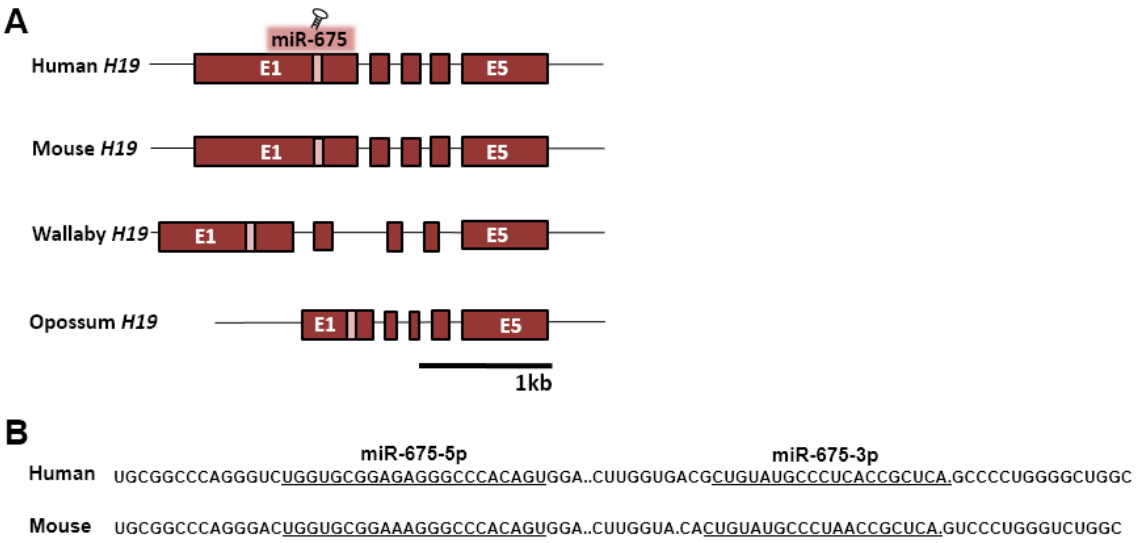

Figure 1.5 *H19* and miR-675 in therians. (*A*) Scale illustration of *H19* gene in eutherians (human and mouse) and marsupials (wallaby and opossum). Although sequence conservation between eutherians and marsupials is low, the exonal structure of the gene is largely conserved in therians. Each exon (E) is depicted in red box. The conserved miR-675 sequence is represented in pink box within E1. (*B*) Shown is the precursor regions of the conserved miR-675 in human and mouse. The predicted mature forms of the miR-675-5p and the miR-675-3p are underlined. Figures adapted from Smits *et al*. (Smits et al., 2008).

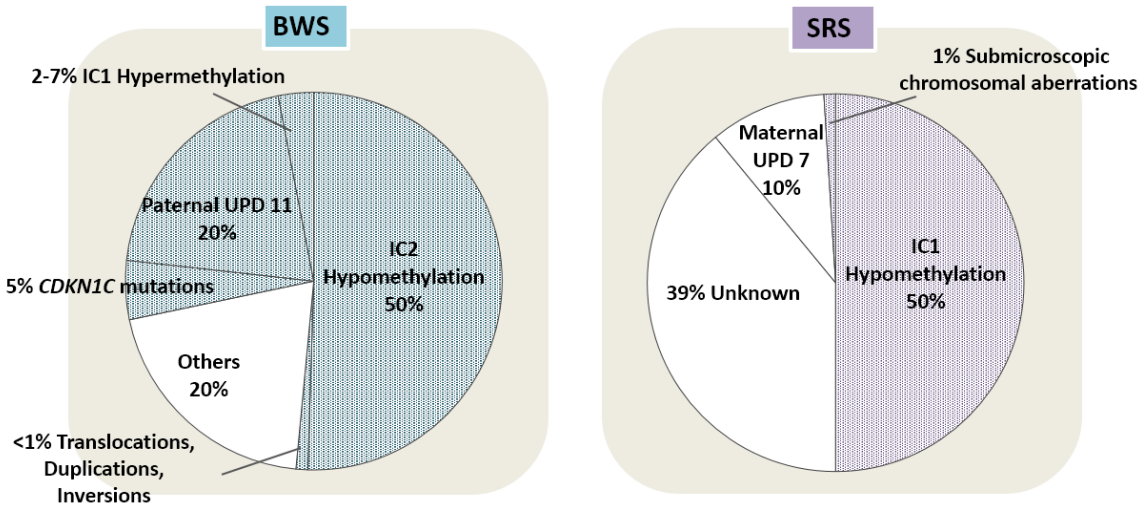

Figure 1.6 Alterations associated with BWS and SRS. In both pie charts, alterations found in human 11p15 are represented in colored slices. UPD11: uniparental isodisomy of chromosome 11; UPD7: uniparental isodisomy of chromosome 7 (Ishida, 2016; Soejima and Higashimoto, 2013; Weksberg et al., 2010).

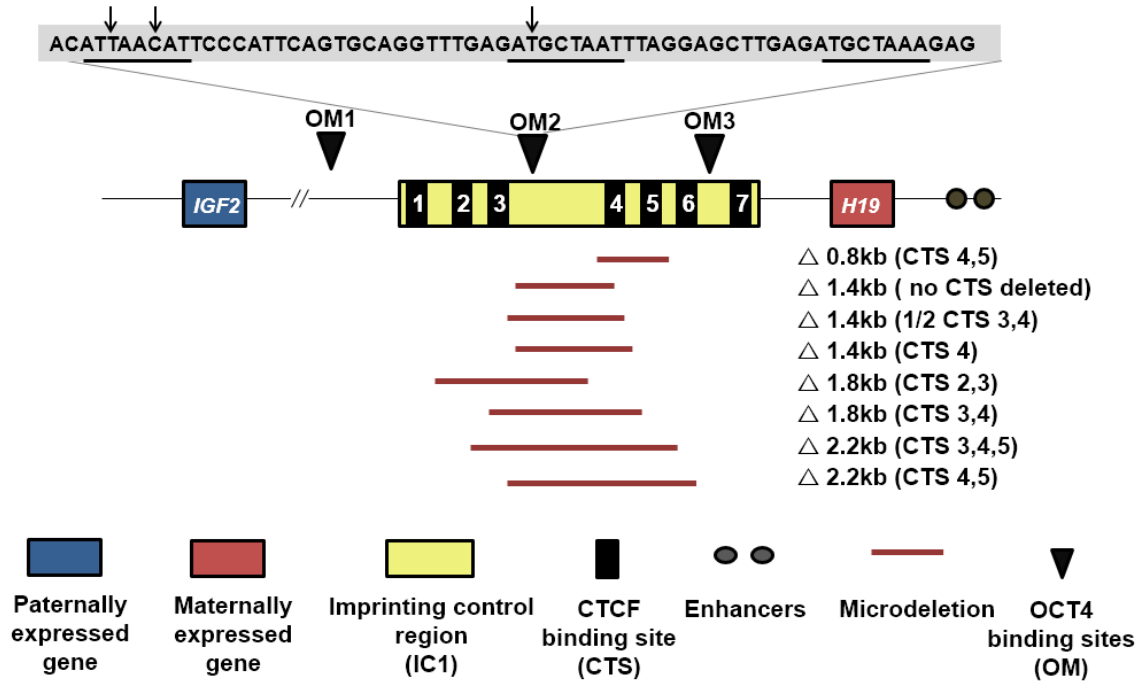

Figure 1.7 IC1 microdeletions and OCT4-binding site point mutations found in BWS IC1 hypermethylation cases. Examples of previously reported mutations at the locus. Here, human IC1 that has seven CTCF binding site (CTS) is illustrated; CTSs within IC1 are numbered for convenience. IC1 microdeletions are depicted in red lines; deletion length and CTS removed by the microdeletion are indicated next to each red line. OCT4-binding sites (Oct4 motif: OM) are noted with inverted triangles; within OM2, three octamer binding motifs are underlined; point mutations are indicated with arrows. Figure modified from Ideraabdullah *et al*. and Beygo *et al*. (Beygo et al., 2013; Demars et al., 2010; Habib et al., 2014; Ideraabdullah et al., 2008; Poole et al., 2012; Prawitt et al., 2005; Sparago et al., 2004).

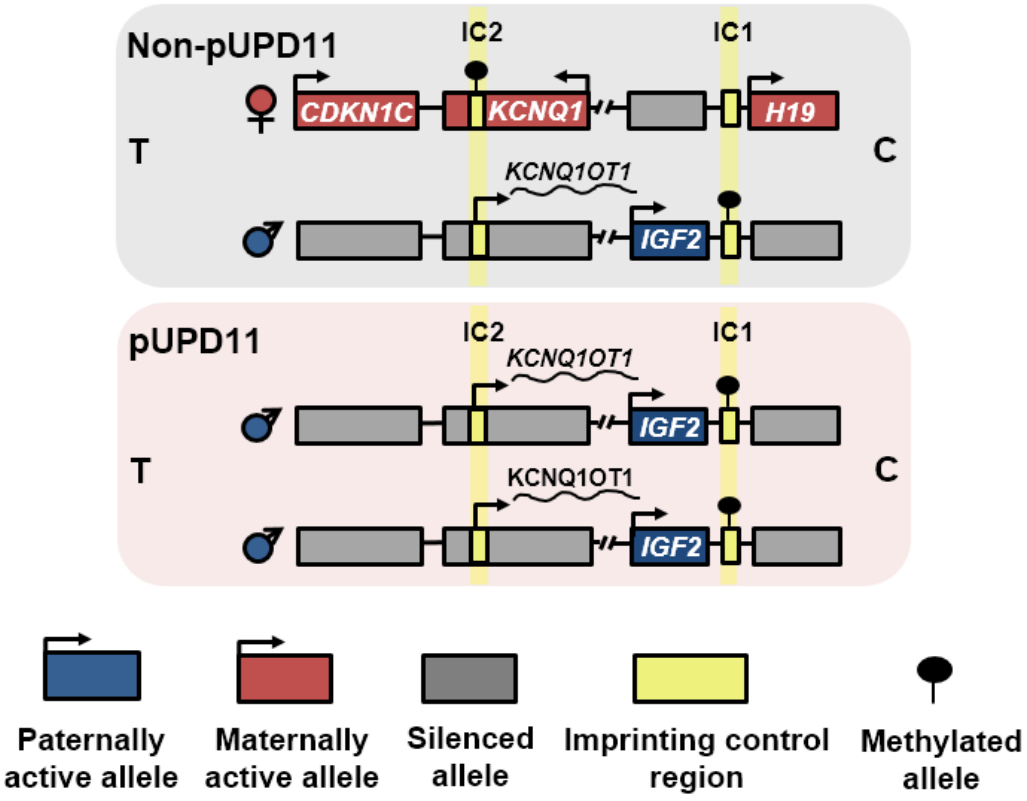

Figure 1.8 pUPD11. A schematic of the 11p15 imprinted loci in non-pUPD11 (top) and pUPD11 (bottom). *Cdkn1c/Kcnq1ot1* locus, regulated by the maternally methylated IC2, is depicted on the left, and *H19/Igf2* locus, regulated by the paternally methylated IC1, is depicted on the right. For simplicity, only selected imprinted genes are shown for the *Cdkn1c/Kcnq1ot1* locus. pUPD11 cells have two copies of paternal allele in this region. The parent-of-origin of the allele is indicated with a female(♀) or a male (♂) symbol. Centromeric (C) and telomeric (T) ends are indicated. Not drawn to scale.

CHAPTER 2.
HUMANIZED MOUSE MODEL

2.1 Background and study rationale

Comparative genome studies have revealed extensive conservation of *H19/Igf2* in therians (Smits et al., 2008). Consistently, key features of imprinting, as well as spatial organization of the mouse and human loci, are shared, including DNA methylation patterns, presence of CTSs at IC1, and downstream enhancers. Notably, however, the length of IC1 and the number of CTSs within IC1 have diverged; the ~5-kb human IC1 has seven CTSs, whereas the corresponding mouse sequence is ~2 kb and has four CTSs (Figure 2.1). In addition, with the exception of the CTCF-binding motifs, IC1 exhibits low sequence homology between mouse and human (Jinno et al., 1996; Jones et al., 2002). This raises the question of whether the human IC1 sequence could successfully regulate *H19/Igf2* imprinting in the mouse. If it can, then an *in vivo* model for imprinting disorders associated with mutations at human IC1 could be generated (Figure 1.7).

Although interspecies compatibility of human IC1 was previously investigated in a transgenic mouse model (Jones et al., 2002), the human transgene failed to exhibit the expected imprinting pattern. The transgene acquired DNA methylation in male germ cells in a copy number-dependent manner, but the methylation was not stably maintained in somatic cells. In addition, the human *H19* transgene was abnormally expressed on paternal transmission. Interpretation of these observations is complicated by transgene copy number variation, however. Furthermore, because long-range chromatin looping plays an essential role in *H19/Igf2* imprinting (Engel et al., 2008; Nativio et al., 2011), the transgene insertion site may influence the phenotype. Thus, it is imperative to test the functionality of the human IC1 element at the orthologous locus.

Here we generated a knock-in mouse model in which the endogenous mouse IC1 (mIC1) was replaced by human IC1 (hIC1). Our goal was to investigate the extent to which hIC1 can functionally replace mIC1. We found that hIC1 properly recapitulates mIC1 function on the maternal allele, whereas hIC1 fails to properly regulate the *H19/Igf2* locus on the paternal allele. hIC1 is incompletely methylated in the male germ cells of knock-in mice, which is associated with increased enrichment of H3K4me2 at hIC1. Overall, this study reveals interspecies incompatibility of hIC1 in the mouse male germline. Importantly, we show that abnormal histone modification composition at hIC1 may affect the proper establishment of DNA methylation at hIC1 during mouse germ cell development.

2.2 Generation of the *H19^{hIC1}* allele

To determine whether hIC1 could functionally substitute for the orthologous mouse sequence, we replaced the endogenous mIC1 with hIC1 by gene targeting in ESCs (Figure 2.2A). Even though we obtained highly chimeric mice after blastocyst injection of the targeted ESCs, germline transmission of the targeted allele was inefficient. Only one female pup with the *H19^{hIC1}* allele was live-born out of >250 agouti pups; all other agouti pups were wild-type, suggesting that the pups inheriting the *H19^{hIC1}* allele might be dying prenatally. The single live-born female knock-in pup was of noticeably smaller size compared with its wild-type siblings and remained small. The neomycin resistance cassette (NeoR) was excised by crossing the female to EIIA-Cre male on a C57BL/6J (B6) background (Jackson Laboratories). Germ-line transmission of the targeted allele and excision of NeoR were confirmed by Southern blot analysis (Figure 2.2B). When bred to a B6 male, the female knock-in mouse was fertile, and wild-type and knock-in progeny were born in the expected Mendelian ratios with no sex bias.

Embryonic lethality on paternal transmission was again observed after NeoR excision. The use of knock-in males in a B6/CF1 mixed strain for paternal transmission did not resolve the embryonic lethality. These results rule out NeoR and pure B6 background as being solely responsible for the failure to obtain mutant pups. The $H19^{hIC1}$ allele was maintained through maternal transmission in a B6 background.

2.3 IC1 imprinting upon maternal transmission of the $H19^{hIC1}$ allele

To investigate *H19* and *Igf2* imprinting when the targeted allele was maternally transmitted, we bred female $H19^{hIC1/+}$ mice to B6 (CAST7) mice, which have a *Mus musculus castaneus* chromosome 7 on a B6 background (Mann et al., 2003). This cross allows the parental origin of *H19* and *Igf2* expression to be distinguished in F1 progeny. Heterozygous $H19^{hIC1/+}$ mice were compared with their wild-type littermates ($H19^{+/+}$). The $H19^{hIC1/+}$ and $H19^{+/+}$ mice were born in Mendelian ratios with no sex bias and no difference in neonatal weight (Figure 2.3A). We assayed expression and IC1 methylation in neonatal livers, where *H19* and *Igf2* are highly expressed, and detected monoallelic expression in all cases (Figure 2.3B). Consistently, total expression levels of *H19* and *Igf2* were statistically equivalent in $H19^{+/+}$ and $H19^{hIC1/+}$ livers, as measured by quantitative real-time PCR (qRT-PCR) (Figure 2.3C). DNA methylation at hIC1 on the maternal allele and endogenous mIC1 on the paternal allele was measured by bisulfite mutagenesis of genomic DNA, followed by pyrosequencing. The maternal hICI was hypomethylated, as expected (Figure 2.4A). Methylation at several other ICRs in $H19^{hIC1/+}$ livers was normal, suggesting that the general imprinting machinery is functioning normally (Figure 2.4B). Finally, hIC1 was properly hypomethylated in the oocytes of $H19^{hIC1/+}$ females (Figure 2.4C). We repeated these analyses in two sequential generations of the $H19^{hIC1}$ allele maternal transmission offspring and obtained

the same results. Overall, these data illustrate that hIC1 can functionally replace mIC1 on the maternal allele.

2.4 IC1 imprinting upon paternal transmission of the *H19^{hIC1}* allele

To investigate *H19* and *Igf2* imprinting on the paternal allele, we bred male *H19hIC1/+* mice to B6 (CAST7) mice. All live-born neonates were wild-type, similar to what was observed when breeding for germ-line transmission in chimeric mice, suggesting that paternal transmission of the *H19^{hIC1}* allele is embryonic lethal. To investigate this possibility, we isolated E15.5 conceptuses. Although the *H19$^{+/hIC1}$* conceptuses were viable, the *H19$^{+/hIC1}$* embryos and placentas were smaller and weighed significantly less compared with those of *H19$^{+/+}$* (Figure 2.5A). Anecdotally, such a size difference was not apparent at E10.5, and a trend toward a smaller size was observed at E12.5. The fetal/placental weight ratio was not different between E15.5 *H19$^{+/+}$* and *H19$^{+/hIC1}$*, demonstrating that *H19$^{+/hIC1}$* tissues were proportionately smaller (Figure 2.5B). Allele-specific RNA analysis revealed biallelic *H19* in E15.5 *H19$^{+/hIC1}$* livers and placentas, with equal expression derived from the two parental alleles (Figure 2.5C and E), suggesting complete derepression of paternal *H19*. In contrast, paternal *Igf2* expression was barely detectable, indicating complete repression of *Igf2* (Figure 2.5C and E). Consistently, qRT-PCR analyses revealed approximately 3.4-fold and 1.5-fold increases of *H19* in liver and placenta, respectively, and undetectable *Igf2* in *H19$^{+/hIC1}$* compared with *H19$^{+/+}$* embryos in both tissues (Figure 2.5D and F). Similar results were observed in E9.5 whole embryos (Figure 2.5G and H).

We next examined the extent to which methylation at hIC1 correlated with abnormal expression in heterozygous livers and placentas. hIC1 was completely unmethylated on the paternal allele, resembling the endogenous mIC1 on the maternal

allele (Figure 2.6A and B). This unusual methylation pattern was not due to a gross defect in the methylation machinery, because methylation at other ICRs was normal in *H19*$^{+/hIC1}$ embryos (Figure 2.6C).

Finally, to determine whether the hypomethylated state of hIC1 is associated with ectopic binding of CTCF on the paternal allele, we performed allele-specific chromatin immunoprecipitation (ChIP) followed by quantitative real-time PCR (ChIP–qRT-PCR) for CTCF in E12.5 mouse embryonic fibroblasts (MEFs). As expected, CTCF bound only to the unmethylated hIC1 on the maternal allele and did not bind to the methylated mIC1 on the paternal allele in *H19*$^{hIC1/+}$ MEFs. In contrast, CTCF bound to both the unmethylated mIC1 on the maternal allele and the unmethylated hIC1 on the paternal allele in *H19*$^{+/hIC1}$ MEFs (Figure 2.7). The results demonstrate that paternal hIC1 is unable to acquire or maintain the hypermethylated state of endogenous mIC1, fails to repress *H19*, and instead gains a CTCF-dependent insulator function.

Because the paternal allele in E15.5 *H19*$^{+/hIC1}$ embryos was hypomethylated, we assayed DNA methylation at earlier stages. We did not detect any methylation at hIC1 as early as the blastocyst stage (Figure 2.8).

2.5 DNA methylation at the *H19*^{hIC1} allele in the male germline

The observation that hIC1 was hypomethylated even as early in the blastocyst stage embryos suggested that either methylation was not established during spermatogenesis or methylation was established but was lost during preimplantation development. To distinguish between these possibilities, we examined DNA methylation at hIC1 in sperm of *H19*$^{hIC1/+}$ males, and observed partial methylation (Figure 2.9A and B). As positive controls, we analyzed methylation at endogenous hIC1 in human sperm samples from two fertile men as well as at endogenous mIC1 in *H19*$^{hIC1/+}$ sperm and

found that all were hypermethylated, as expected (Figure 2.9A and B). To explore whether the methylation at hIC1 in *H19*$^{hIC1/+}$ sperm could be maintained after the first cleavage division, we assayed *H19*$^{+/hIC1}$ two-cell embryos in which the zygote had undergone one round of mitosis. We found reduced methylation levels (close to one-half less) at hIC1 in two-cell embryos compared with mature sperm (Figure 2.9A). These results demonstrate that the DNA methylation is partially established at hIC1 during spermatogenesis, but is not maintained in preimplantation development.

2.6 Histone modification at the *H19*^{hIC1} allele in the male germline

To investigate factors that may inhibit complete establishment of DNA methylation at hIC1 during spermatogenesis, we examined histone modifications at hIC1. Parental allele-specific histone modifications have been described at mIC1 in both somatic and germ cells (Delaval et al., 2007; Lee et al., 2010; Singh et al., 2013; Stewart et al., 2015; Verona et al., 2008). For instance, H3K4 methylation is found preferentially on the hypomethylated maternal IC1, and H3K9me3 is found on the hypermethylated paternal IC1 in mouse and human somatic cells (Delaval et al., 2007; Nativio et al., 2011)). The antagonistic relationship between “activating marks” and DNA methylation (Ciccone et al., 2009; Ooi et al., 2007; Singh et al., 2013; Stewart et al., 2015) has been well-established. Moreover, several studies illustrated a strong relationship between “repressive marks,” such as H3K9me3 and DNA methylation (Rose and Klose, 2014).

Therefore, we hypothesized that depletion of H3K9me3, increased enrichment of H3K4me2, or both contribute to the inability to fully establish DNA methylation at hIC1. Spermatogenic cells were fractionated by the STA-PUT method, and chromatin was isolated from a round spermatid-enriched fraction (Bryant et al., 2013). ChIP–qRT-PCR analyses in round spermatids revealed that hIC1 had fivefold greater enrichment of

H3K4me2 compared with mIC1 (Figure 2.9C). Unlike previous studies that did not report significant enrichment of H3K9me3 above background at mIC1 in the male germ line (Delaval et al., 2007; Singh et al., 2013), we obtained a ChIP signal above background. This discrepancy could be attributed to the different antisera used for H3K9me3. Nevertheless, there was no difference in the enrichment of H3K9me3 between hIC1 and mIC1. Our finding that the difference in H3K4me2 between mIC1 and hIC1 is greater than the difference in H3K9me3 suggests that (i) H3K9me3 does not affect the acquisition of DNA methylation at hIC1 during spermatogenesis, and (ii) enrichment of activating histone marks at hIC1 contributes in part to the incomplete establishment of imprinting at hIC1 during spermatogenesis (Figure 2.9C).

2.7 Additional analyses upon paternal transmission of the *H19^{hIC1}* allele

Because *H19$^{+/hIC1}$* embryos display similar phenotypes to many SRS patients that present with IC1 hypomethylation including altered *H19* and *Igf2* expression and growth defects (Gicquel et al., 2005; Yamazawa et al., 2008), we hypothesized that these embryos can serve as a model for SRS. Thus, we further characterized *H19$^{+/hIC1}$* embryos and placentas to study potential mechanisms underlying SRS associated with IC1 hypomethylation.

2.7.1 Imprinted gene network (IGN) genes in *H19$^{+/hIC1}$*

We first investigated several IGN genes, focusing on seven genes (maternally expressed *Cdkn1c*, *Gtl2*, *Igf2r*, and paternally expressed *Dlk1*, *Gnas*, *Peg3*, *Slc38a4*) whose levels were previously shown to be affected by *H19* expression in *trans* (Gabory et al., 2009). In *H19$^{+/hIC1}$* livers, three of the four paternally expressed genes (*Dlk1*, *Gnas*, *Slc38a4*) were significantly upregulated, whereas in *H19$^{+/hIC1}$* placentas, two of the three maternally expressed genes (*Cdkn1c*, *Gtl2*) were downregulated compared to *H19$^{+/+}$*,

suggesting tissue-specific regulation of IGN genes (Figure 2.10). The changes were more subtle in placentas compared to livers. Overall, these results support the previously proposed homeostatic role of IGN genes in controlling fetal growth.

2.7.2 Placental morphology in *H19*$^{+/hIC1}$

Placental growth defects are prevalent among SRS individuals (Yamazawa et al., 2008). Thus, we performed histological analyses on E15.5 *H19*$^{+/hIC1}$ placentas to explore whether abnormal placentation could contribute to embryonic growth restriction, given that *H19* and *Igf2* play essential roles in placental development (Bartolomei and Ferguson-Smith, 2011; Reik et al., 2003). In addition to being smaller (~74% of *H19*$^{+/+}$), *H19*$^{+/hIC1}$ placentas displayed an increased junctional to labyrinthine zone ratio, indicative of abnormal placenta morphology (Figure 2.11A and B).

2.7.3 miR-675 in *H19*$^{+/hIC1}$

Lastly, miR-675 was analyzed in the *H19*$^{+/hIC1}$ embryos and placentas. The role of miR-675 in limiting cell proliferation has been demonstrated in various cell types *in vitro* (Keniry et al., 2012). Thus, we measured the level of miR-675-3p and miR-675-5p in E15.5 *H19*$^{+/hIC1}$ livers and placentas. Despite being more highly expressed in placentas compared to livers, both miR-675-3p and miR-675-5p were elevated only in *H19*$^{+/hIC1}$ livers but not in placentas compared to *H19*$^{+/+}$ (Figure 2.12A). These data suggest that in addition to greatly reduced *Igf2* and increased *H19* expression in *H19*$^{+/hIC1}$ placentas and embryos, increased miR-675 expression in embryos may further restrict the growth of embryos.

Keniry *et al*. proposed *Igf1r* as a potential target of miR-675-3p (Keniry et al., 2012). To support this idea, *Igf1r* is upregulated in E18.5 mouse placenta in which *H19* sequence is deleted (Keniry et al., 2012), suggesting that the concurrently deleted miR-

675 could be repressing *Igf1r*. Thus, we expected that in $H19^{+/hIC1}$ livers, where miR-675 is upregulated, *Igf1r* would be downregulated. Contrary to our hypothesis, *Igf1r* was upregulated in $H19^{+/hIC1}$ livers. In placentas, *Igf1r* level was unchanged, consistent with no significant change in miR-675 expression in this tissue (Figure 2.12B). These data suggest that the miR-675 mediated silencing of *Igf1r* does not occur in liver or that other dominant molecular phenotypes caused by IC1 hypomethylation might be masking the silencing effect of miR-675.

2.8 Testing the role of miR-675 vs *H19* in growth regulation

Potentially distinct mechanisms used by *H19* and miR-675 to suppress embryonic growth have not been investigated in a tissue-and/or temporal-specific manner. To address this, the $H19^{+/hIC1}$ animals that exhibit increased *H19* and miR-675 expression and severe growth phenotype could serve as an informative platform (Figure 2.13A). Therefore, we have designed two rescue experiments that would allow us to test the role of miR-675 independent of *H19* in growth restriction caused by IC1 hypomethylation (Figure 2.13B and C). This approach could shed light on the contribution of miR-675 and *H19* in the etiology of SRS.

2.8.1 $H19^{+/miR\text{-}675mut}$ x $H19^{hIC1/+}$

$H19^{miR\text{-}675mut}$ allele

First rescue experiment utilizes the mouse model, designated $H19^{miR\text{-}675mut}$, generated by a previous member of the Bartolomei lab, Jennifer Kalish, MD, PhD. In this mouse model, the miR-675 sequence was mutated such that the stem-loop structure of the miR is maintained while the targeting ability is impaired. This mouse model does not seem to have any apparent phenotype thus far (personal communication with Jennifer

Kalish). Importantly, *H19* expression is not affected in this model (Kalish et al., unpublished).

Mating scheme

The goal is to generate offspring from $H19^{+/miR\text{-}675mut}$ females and $H19^{hIC1/+}$ males (Figure 2.13B). This will allow us to analyze the extent to which the reduced dosage of miR-675 has an effect in relieving the molecular and/or physiological phenotypes of the $H19^{+/hIC1}$ animals. Thus, we will be able to elucidate the contribution of miR-675 in leading to the SRS-like phenotypes. These crosses have been setup and the E15.5 and E18.5 embryos and placentas will be collected.

2.8.2 $H19^{+/\Delta H19}$ x $H19^{hIC1/+}$

Generation of the *$H19^{\Delta H19}$ allele*

As a complementary approach, we generated a mouse model, designated $H19^{\Delta H19}$, in which the *H19* sequence is deleted using the Clustered Regularly Interspaced Short Palindromic Repeats (CRISPR)/Cas9 technology. To do this, two different pairs (pair A and B) of guide RNA (gRNA) were designed using the program developed by the laboratory of Dr. Feng Zhang (http://www.genome-engineering.org/crispr/?page); within a pair of gRNA, each gRNA was designed to target the 5' or the 3' end of the *H19* sequence (Figure 2.14A). The gRNAs were *in vitro*-transcribed and injected with Cas9 mRNA (Trilink) directly into zygote stage embryos in B6 background. One pair of gRNA (either pair A or pair B) was injected per embryo. This approach led to in total ~26% efficiency in generating both female and male chimeras, with pair B exhibiting a higher efficiency (~24%) than pair A (~2%). Sequencing the deleted region revealed 2.7kb to 2.8kb deletion in the chimeras (Figure 2.14B). The

chimeras successfully transmitted the mutant allele through the germline. Both female and male mutant mice were fertile, and wild-type and mutant progeny were born in the expected Mendelian ratios with no sex bias. The mutant allele is currently maintained in B6 background via paternal transmission.

Previous mouse models deleting the *H19* sequence (Leighton et al., 1995b; Ripoche et al., 1997) left a transcription unit at the deleted site— NeoR cassette—that could potentially interfere with the imprinting mechanism at the locus. The other *H19*-deletion mouse (Schmidt et al., 1999) left a loxP site at the locus. Importantly, the $H19^{\Delta H19}$ allele we generated does not introduce any exogenous sequence at the locus, eliminating the possibility of imprinting regulation being affected.

Characterization of the $H19^{+/\Delta H19}$ and the $H19^{\Delta H19/+}$ animals

Day 0 neonatal weight was analyzed in the maternal transmission ($H19^{\Delta H19/+}$) and the paternal transmission ($H19^{+/\Delta H19}$) animals. There was no significant weight difference between $H19^{+/\Delta H19}$ compared to wild-type siblings ($H19^{+/+}$) (Figure 2.15A); yet, $H19^{\Delta H19/+}$ were significantly heavier compared to $H19^{+/+}$ (i.e. $H19^{\Delta H19/+}$ displayed on average 13.8% increase in body weight compared to $H19^{+/+}$) (Figure 2.15B). This result is similar to the observation made in the previous *H19*-deletion mouse models, where they noticed 4-12% increase in body weight in day 3-5 neonates in various genetic backgrounds (Ripoche et al., 1997; Schmidt et al., 1999). Thus, our mouse model supports the role of *H19* being a maternally expressed growth suppressor.

Nevertheless, molecular analyses of these mice remain to be completed. Various tissues of the neonates were collected including brain, tongue, liver, kidney, and heart. Select tissues will be analyzed for parameters including allele-specific and total

expression of *H19* and *Igf2* and DNA methylation at IC1 to address the necessity of *H19* in the maintenance of imprinting at the *H19/Igf2* locus. In addition, germ cells of these mice will be analyzed to address the effect of *H19* deletion in methylation establishment at the IC1.

Mating scheme

Similar to the approach proposed for the $H19^{miR\text{-}675mut}$ allele, the goal is to generate offspring from $H19^{+/\Delta H19}$ females and $H19^{hIC1/+}$ males (Figure 2.13C). These crosses have been setup and the E15.5 and E18.5 embryos and placentas will be collected. This strategy will address the extent to which reducing the dosage of both *H19* and miR-675 alters the SRS-like phenotypes in the $H19^{+/hIC1}$ animals.

2.9 Discussion

Using a mouse model replacing endogenous mIC1 with hIC1, we show that the ability of hIC1 to functionally replace mIC1 depends upon the parental origin of the hIC1 allele.

Maternally transmitted hIC1 properly carries out imprinting regulation at the endogenous mouse locus, suggesting that the IC1 imprinting on the maternal allele is largely conserved between mouse and human (Figure 2.16). Paternal transmission of hIC1, in contrast, leads to loss of *H19* and *Igf2* imprinting; *H19* displays biallelic and increased expression and *Igf2* is silenced (Figure 2.17). Offspring inheriting hIC1 paternally also exhibit severe growth restriction. Other studies have shown that *Igf2* null neonates are born smaller but viable (Baker et al., 1993; DeChiara et al., 1990), suggesting that prenatal lethality of $H19^{+/hIC1}$ is not solely due to loss of *Igf2*. Notably, ectopic expression of *H19* caused late-gestation lethality (Brunkow and Tilghman, 1991).

Thus, changes in both *H19* and *Igf2* may synergistically contribute to the severe growth restriction and prenatal lethality of $H19^{+/hIC1}$.

In addition to changes in *H19* and *Igf2*, miR-675 and IGN gene levels are altered in $H19^{+/hIC1}$ embryos and placentas (Figure 2.17). To our knowledge, this is the first report showing that complete biallelic insulation at the endogenous *H19/Igf2* locus could lead to changes in miR-675 or other growth-regulating imprinted genes *in vivo*. Given that the maternally expressed imprinted genes tend to suppress growth, whereas paternally expressed imprinted genes promote growth, the seemingly disparate changes in IGN gene expression between $H19^{+/hIC1}$ livers and placentas both encourage growth. This result reaffirms the previously proposed homeostatic role of IGN genes to control embryonic and placental growth. Despite these potentially compensatory changes, however, $H19^{+/hIC1}$ embryos are still severely growth-restricted and die prenatally.

Whether the increased level of miR-675 or *H19* in $H19^{+/hIC1}$ liver contributes to the embryonic growth restriction phenotype needs to be further investigated. We have setup experiments to specifically address this question as discussed in Chapter 2.8.1 and 2.8.2. Surprisingly, miR-675 is only increased in livers, but not in placentas. It will be interesting to assess the expression of miR-675 later in gestation, such as E18.5-19.5, when the highest level of miR-675 is observed in both liver and placenta (Keniry et al., 2012). However, it is possible that miR-675 is differently regulated in liver compared to placenta.

The upregulation of *Igf1r* transcript, observed in a tissue where miR-675 was upregulated, is unexpected. This result does not invalidate *Igf1r* as a potential target of miR-675 in placenta (Keniry et al., 2012). Nevertheless, it is possible that the miR-675 regulation of *Igf1r* is cell-type specific. Given that $H19^{+/hIC1}$ tissues display changes in the

expression of *Igf2* and other IGN genes, upregulation of the *Igf1r* transcript perhaps reflects a response to the altered IGF2-associated signaling pathway.

Previous studies illustrated that abnormal *H19* and *Igf2* expression is linked to both placental and embryonic growth defects. Deletion of a placenta-specific *Igf2* transcript resulted in growth restriction of embryos in late gestation (Constância et al., 2002). In a mouse model in which *H19* is deleted and *Igf2* expression is increased, both placenta and fetus are overgrown at E19 (Angiolini et al., 2011; Leighton et al., 1995b). In humans, placental growth defects are common among individuals with BWS and SRS (Armes et al., 2012; Yamazawa et al., 2008). We observed that $H19^{+/hIC1}$ placentas are not only smaller but have abnormal placental morphology. While the contribution of an abnormal placenta to fetal growth defects is unclear, it is noteworthy that *H19* is more highly expressed in labyrinthine zone compared to junctional zone (Keniry et al., 2012), and that *Igf2* null mice display a disproportionate reduction of labyrinthine zone compared to junctional zone (Coan et al., 2008). These observations suggest a potential major growth-suppressing effect of increased *H19* and silenced *Igf2* expression in the labyrinthine zone.

We also show that hIC1 is partially methylated in the male germline of $H19^{hIC1/+}$ mice. This phenotype contrasts that of other mouse models that carry mIC1 mutations; in these mice, methylation is properly established at non-mutated CpGs in the male germline (Engel et al., 2004, 2006). This result suggests that interspecies communication between mouse and human in establishing IC1 methylation is ineffective. Based on our finding that hIC1 is abnormally enriched with activating H3K4me2 marks in the male germ cells, it is tempting to speculate that somatic histone modification marks carried from the maternal allele are not completely erased in the male germ cells (note

that hIC1 was necessarily transmitted maternally to generate offspring). Consequently, the establishment of DNA methylation at hIC1 is inhibited. This finding adds to the growing consensus that H3K4 methylation marks are inhibitory to de novo DNA methylation in the germline, whereas repressive histone marks do not play major role in methylation establishment at ICRs (Ciccone et al., 2009; Delaval et al., 2007; Lee et al., 2010; Singh et al., 2013; Stewart et al., 2015).

Finally, we show that the partially established methylation at hIC1 in the male germline is not properly maintained during preimplantation development. We also illustrate that CTCF ectopically binds to the hIC1 on the paternal allele in somatic cells. Similar results are described in a previous mouse model in which CpGs within the CTCF binding sites at the mIC1 were mutated to abrogate methylation, while retaining the CTCF-binding motifs intact. There, although methylation was properly established in the male germ cells at the mIC1, it was not maintained during preimplantation development (Engel et al., 2004). These data suggest that CTCF binding inhibits maintenance of DNA methylation in somatic cells, although the mechanism remains unknown. Alternatively, hIC1 might lack properties that allow the mouse imprint maintenance machinery to properly recognize the sequence. It is also possible that hIC1 contains inhibitory signals that block accessibility and/or activity of the mouse imprint maintenance machinery.

2.10 Contributions

This chapter contains direct quotes and figures from Hur *et al*. published in 2016 in Proceedings of the National Academy of Sciences (PNAS) (Hur et al., 2016). The target vector for the *H19*^{hIC1} mouse was made by a collaborative effort between Dr. Folami Ideraabdullah, a former member of the lab, currently at the University of North Carolina at Chapel Hill, and Andrea Freschi, currently in the laboratory of Dr. Andrea

Riccio at the Second University of Naples, Italy. Members of the laboratory of Dr. Shelley Berger at the time, including Dr. Lacey Luense and Ms. Angela Hines, performed the STA-PUT experiments. Dr. Catherine May in the laboratory of Dr. Klaus Kaestner provided guidance in generating the *H19*$^{\triangle H19}$ allele using the CRISPR/Cas9 technology. Dr. Joanne Thorvaldsen provided advice and guidance in performing experiments.

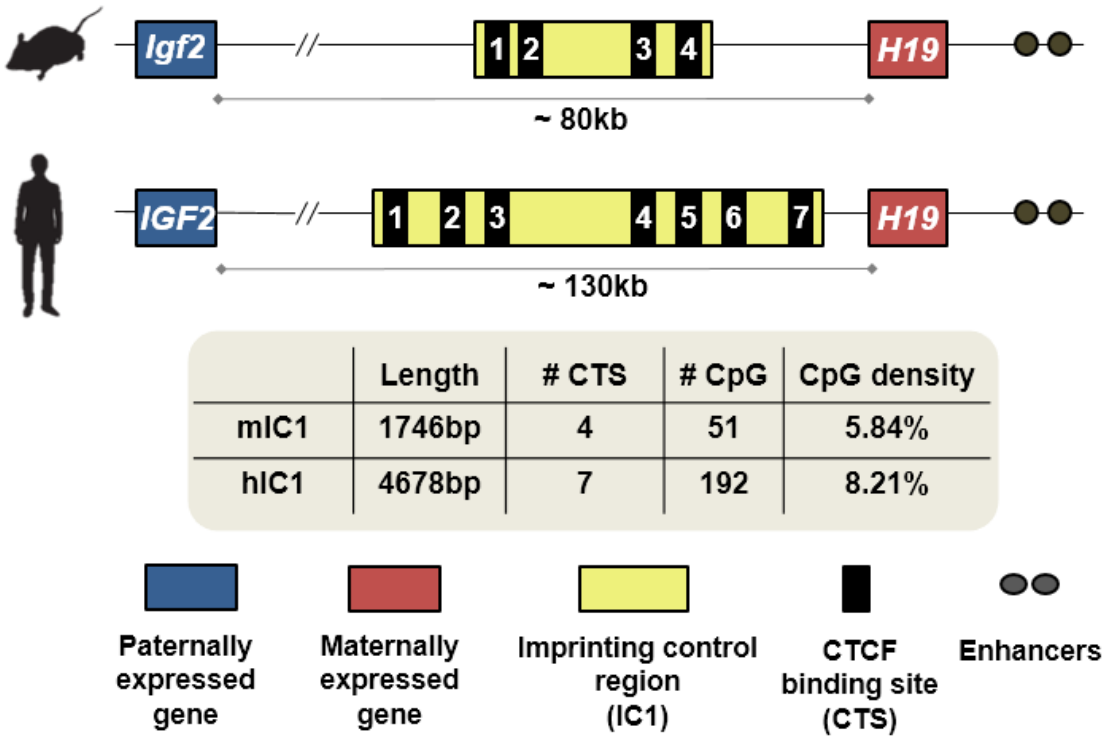

	Length	# CTS	# CpG	CpG density
mIC1	1746bp	4	51	5.84%
hIC1	4678bp	7	192	8.21%

Figure 2.1 Comparison between mouse and human IC1. Mouse IC1 (top) has four CTSs and is ~2kb long. Human IC1 (bottom) has seven CTSs and is ~5kb long. Except for the CTCF-binding motifs, overall sequence homology between the two IC1 is low (Jinno et al., 1996; Jones et al., 2002). The number of CpG sites and CpG density at IC1 are noted in the table. Approximate distance between *H19* and *IGF2* in both mouse and human are indicated. CTSs are numbered for convenience. Human and mouse drawings were adapted from Renfree *et al*. (Renfree et al., 2013).

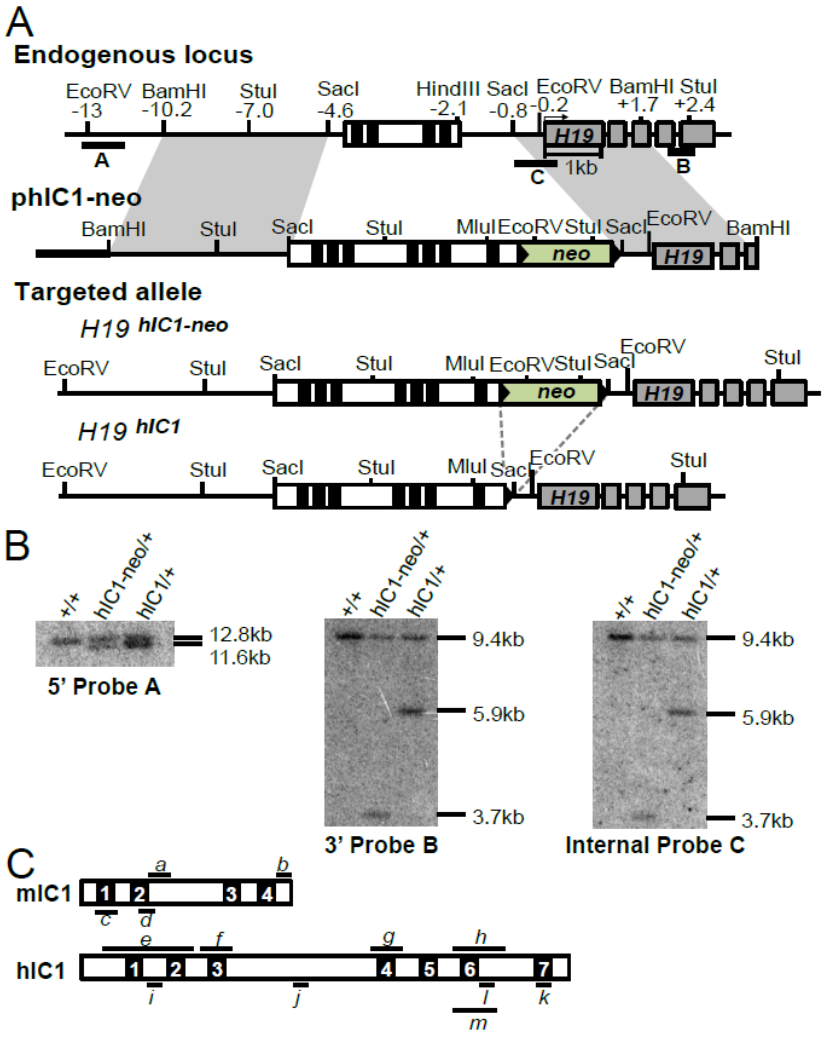

Figure 2.2 Targeting strategy to generate the *H19^{hIC1}* allele. *(A)* Schematics of the endogenous locus, targeting vector (phIC1-neo), correctly targeted allele (*H19$^{hIC1\text{-}neo}$*), and targeted allele after excision of the neoR cassette (*H19^{hIC1}*). Depicted are the IC1 (white rectangle) with CTCF binding sites (black blocks within the IC1), *H19* exons (gray rectangles), pBluescriptIIKS sequence (bold line), neoR cassettes (green rectangles), loxP sites (black arrowheads), and endogenous mouse DNA (thin line). Restriction sites and their relative positions (in kb) to the *H19* transcription start sites are indicated above the endogenous locus. Probes (A, B, and C) used for Southern blot analyses are shown as thick lines below the endogenous locus. *(B)* Southern blot analysis to confirm correct targeting of the alleles. Genomic DNA from the wild-type mouse (+/+), knock-in mouse before neoR excision (hIC1-neo/+), and knock-in mouse after neoR excision (hIC1/+) was either digested with EcoRV-MluI and hybridized to external 5'probe A or digested with StuI and hybridized to external 3'probe B or to internal probe C. *(C)* Depiction of mIC1 (top) and hIC1 (bottom) highlighting PCR analyzed regions (*a*-*m*). IC1s are illustrated in the orientation shown in Fig 2.2A, with each CTCF binding site (CTS) numbered. *a*: bisulfite treatment followed by sequencing for mIC1; *b,c*: chromatin immunoprecipitation followed by quantitative real-time PCR (ChIP-qRT-PCR) for mIC1; *d*: pyrosequencing for mIC1; *e*-*h*: bisulfite treatment followed by sequencing for hIC1; *i*-*k*: ChIP-qRT-PCR for hIC1; *l*: pyrosequencing for hIC1; *m*: bisulfite treatment followed by sequencing for hIC1 (used for oocytes).

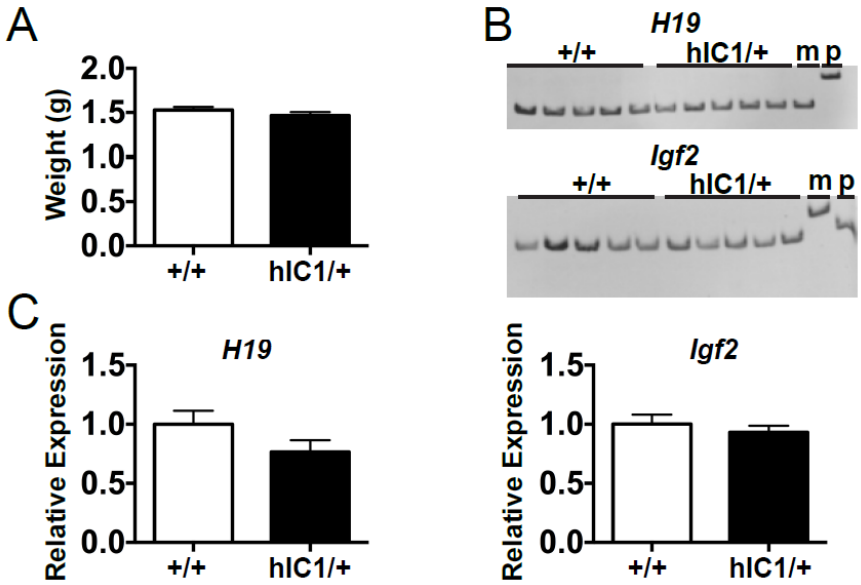

Figure 2.3 Weight and expression analyses of maternal transmission of the *H19^{hIC1}* allele. *(A)* Neonatal (P0) weight of wildtype (+/+) and heterozygous (hIC1/+) mutant offspring. *(B)* Allele-specific expression of *H19* and *Igf2* in neonatal liver analyzed by restriction fragment length polymorphism (RFLP). Genotypes (+/+ and hIC1/+) and maternal (m) and paternal (p) allele controls are indicated above each gel. *(C)* Total expression of *H19* and *Igf2* in neonatal liver analyzed by qRT-PCR. *(A,C)* Two-tailed Student's T-test with equal variance; no significant differences were observed. *(A-C)* +/+: n=11, hIC1/+: n=12 (from three litters). Bars represent the mean ± SEM; error bars in *(A)* are too small to be seen on the graph.

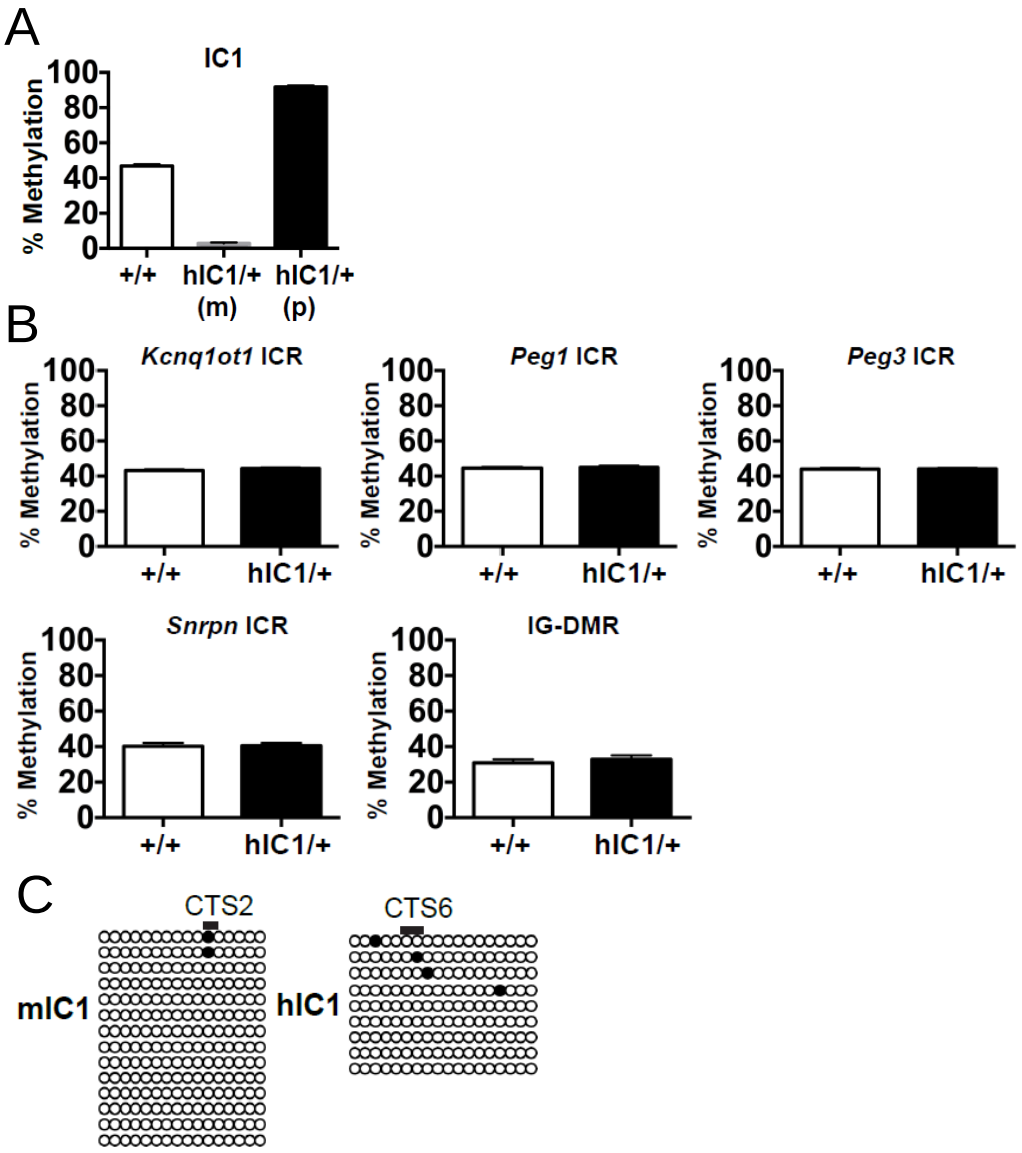

Figure 2.4 Methylation analyses of maternal transmission of the *H19^{hIC1}* allele. *(A)* Percent methylation at IC1 in neonatal liver measured by pyrosequencing. Maternal (m) and paternal (p) alleles in hIC1/+ are shown separately as different primers were used; assay *d* was used for the +/+ and hIC1/+(p); assay *l* was used for the hIC1/+(m) (Figure 2.2*C*). (*B*) Methylation levels of *Kcnq1ot1*, *Peg1*, *Peg3*, *Snrpn*, *Dlk1/Gtl2* (IG-DMR) ICRs were measured by pyrosequencing in neonatal liver. *(C)* IC1 methylation in oocytes analyzed by bisulfite treatment followed by sequencing. Assay *a* was used for mIC1; assay *m* was used for hIC1 (Figure 2.2*C*). Empty and filled circles indicate unmethylated and methylated cytosines in CG dinucleotides, respectively. Each horizontal row of circles denotes individual strands of cloned DNA. Cytosines in CG dinucleotides that are conserved between mouse and human and located within CTS are depicted as black lines above the clones and marked as CTS 2 and 6 (Bell and Felsenfeld, 2000). *(A,B)* +/+: n=11, hIC1/+: n=12 (from three litters). (*B*) Two-tailed Student's T-test with equal variance; no significant differences were observed. Bars represent the mean ± SEM; error bars in *(A)* and *(B)* are too small to be seen on the graph.

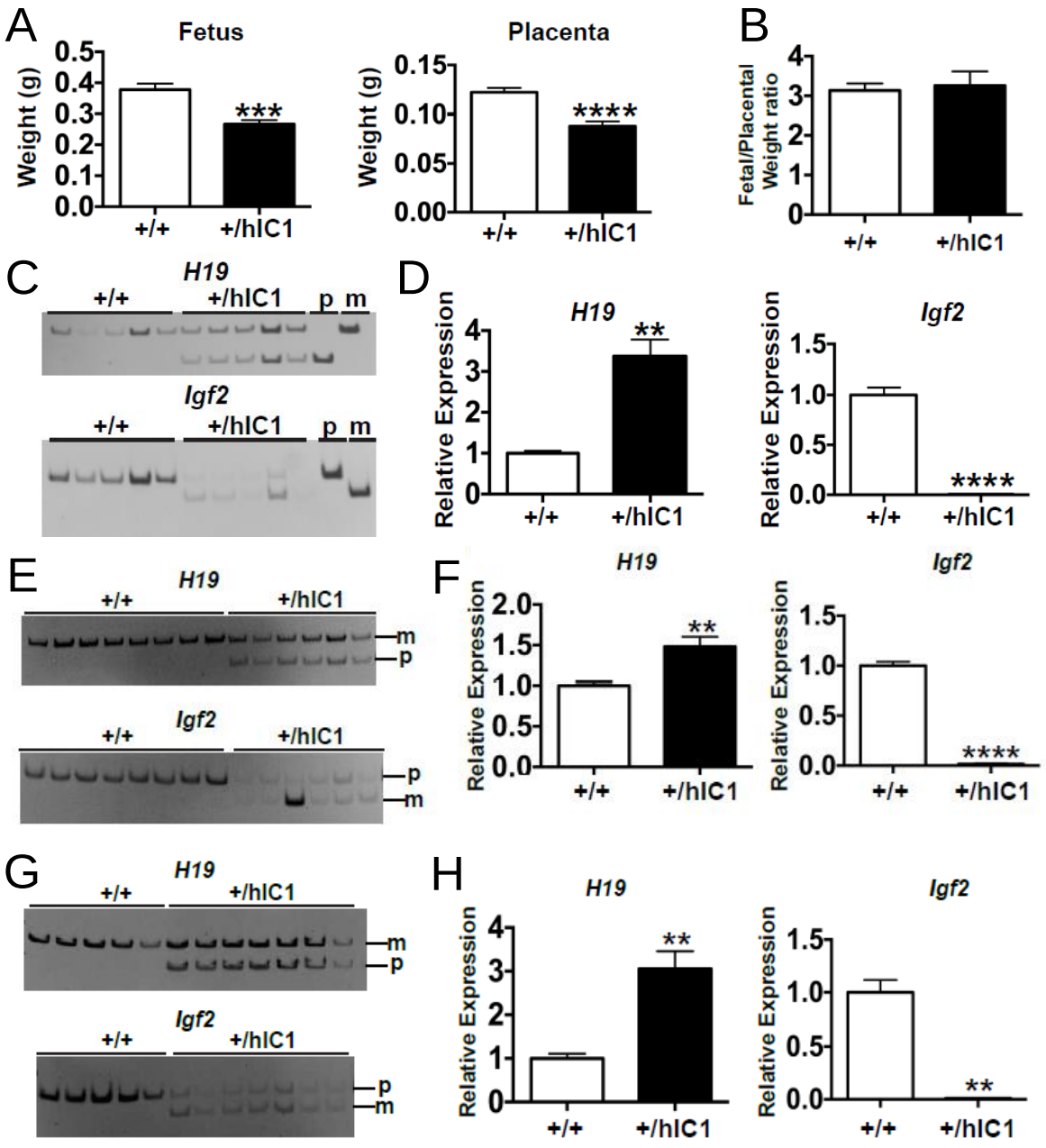

Figure 2.5 Weight and expression analyses of paternal transmission of the *H19^{hIC1}* allele. *(A)* E15.5 fetal and placental weight of wild-type (+/+) and heterozygous (+/hIC1) mutant offspring. *(B)* Fetal/placental weight ratio of E15.5 samples. Allele-specific expression of *H19* and *Igf2* in (*C*) E15.5 liver, (*E*) E15.5 placenta, and (*G*) E9.5 whole embryo analyzed by RFLP. PCR cycle numbers varied between +/+ and +/hIC1 for *Igf2* (see Table 5.1). Total expression of *H19* and *Igf2* in *(D)* E15.5 liver, (*F*) E15.5 placenta, and (*H*) E9.5 whole embryo analyzed by qRT-PCR. Two-tailed Student's T-test with (*A*) equal variance and (*D,F,H*) unequal variance; ** ($P < 0.01$); *** ($P < 0.001$); **** ($P < 0.0001$). *(A,B,D,F)* +/+: n=8, +/hIC1: n=6 (from two litters). (*H*) +/+: n=5, +/hIC1: n=7 (from two litters). Bars represent the mean ± SEM; error bars in *(D,F,H)* are too small to be seen on the graph.

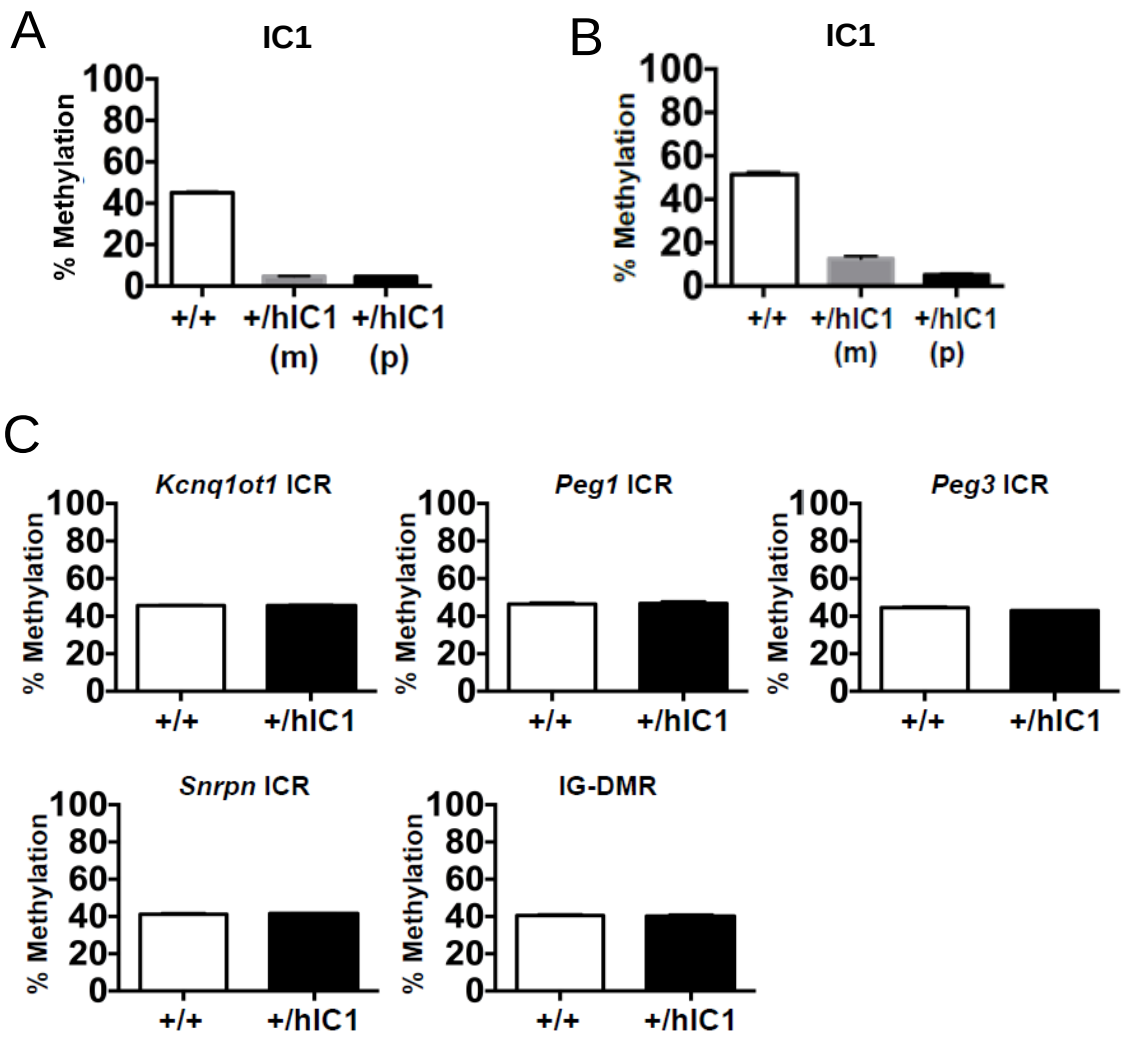

Figure 2.6 Methylation analyses of paternal transmission of the *H19^{hIC1}* allele. Percent methylation at IC1 in (*A*) E15.5 liver and (*B*) E15.5 placenta measured by pyrosequencing; assay *d* was used for the +/+ and +/hIC1(m); assay *l* was used for the +/hIC1(p) (Figure 2.2*C*). (*C*) Methylation levels of *Kcnq1ot1*, *Peg1*, *Peg3*, *Snrpn*, *Dlk1/Gtl2* (IG-DMR) ICRs were measured by pyrosequencing in E15.5 liver. *(A,B,C)* +/+: n=8, +/hIC1: n=6 (from two litters). Error bars in (*A-C*) are too small to be seen on the graph. (*C*) Two-tailed Student's T-test with equal variance; no significant differences were observed. Bars represent the mean ± SEM. (*A,B,C*) error bars are too small to be seen on the graph.

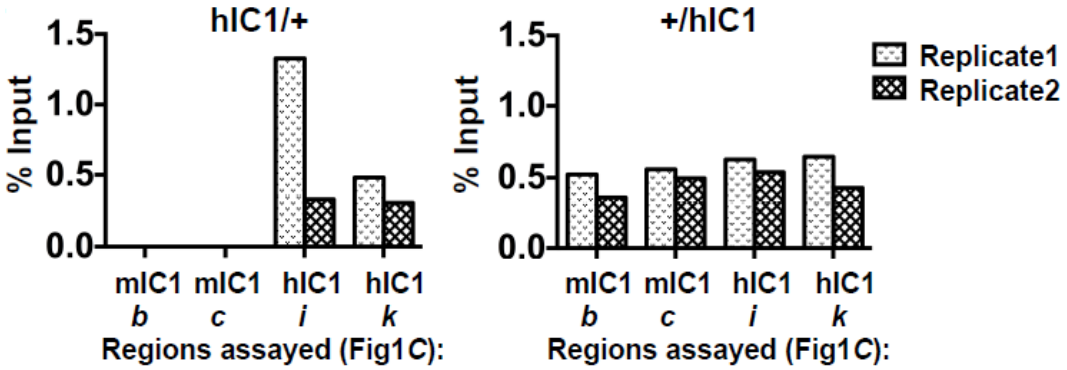

Figure 2.7 CTCF-binding analyses of paternal transmission of the *H19^{hIC1}* allele. CTCF binding at mIC1 and hIC1 in heterozygous (hIC1/+ and +/hIC1) E12.5 MEFs analyzed by ChIP-qRT-PCR; assays *b*, *c*, *i*, *k* were used (Figure 2.2*C*); results from two biological replicates are shown separately; y-axis denotes percent input of CTCF IP normalized to non-specific IgG (percent input CTCF - percent input IgG).

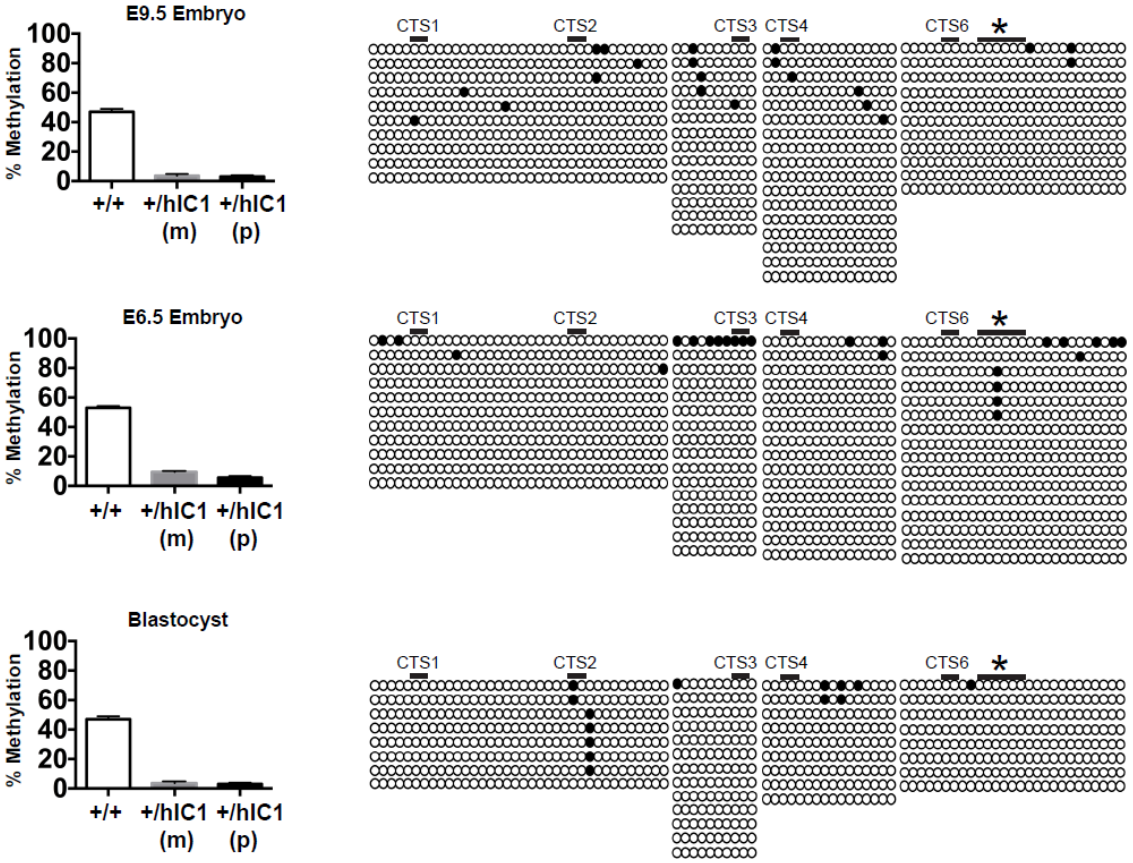

Figure 2.8 Methylation at IC1 in *H19*$^{+/hIC1}$ embryos during development. Bar graphs summarize the DNA methylation status of E9.5 whole embryo (+/+: n=5, +/hIC1: n=7, two litters), E6.5 whole embryo (+/+: n=5, +/hIC1: n=7, two litters), and blastocysts (+/+: n=6, +/hIC1: n=9, four litters) measured by pyrosequencing. Assay *d* was used for the +/+ and +/hIC1(m) and assay *l* was used for the +/hIC1(p) (Figure 2.2*C*). On the right, methylation at hIC1 was analyzed by bisulfite treatment followed by sequencing in one representative +/hIC1 sample from each developmental stage; assays *e-h* were used (Figure 2.2*C*). Cytosines in CG dinucleotides that are conserved between mouse and human and located within CTS are depicted as black lines above the clones and marked as CTS 1,2,3,4, and 6 (Bell and Felsenfeld, 2000). Cytosines measured by pyrosequencing are marked with an asterisk. Bars represent the mean ± SEM.

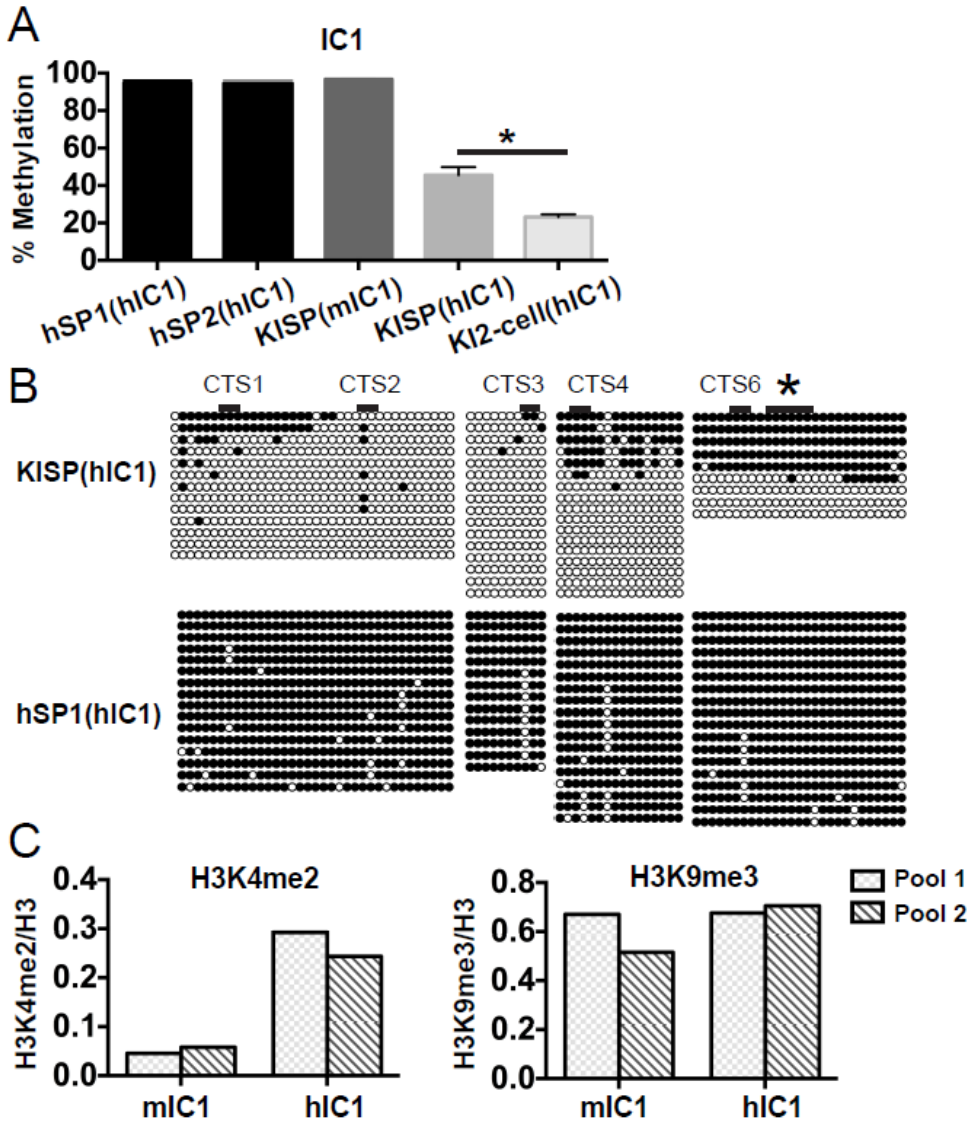

Figure 2.9 Incomplete establishment of imprinting at the hIC1 in knock-in male germ cells. *(A)* Percent methylation at IC1 measured by pyrosequencing; assays *d* and *l* were used (Figure 2.2*C*). From left to right, results at the endogenous hIC1 in mature sperm samples from fertile men (hSP1, hSP2), at the endogenous mIC1 and the targeted hIC1 in knock-in sperm (KISP) from adult mice, and at the targeted hIC1 in pools of *H19*$^{+/hIC1}$ two-cell stage embryos (KI2-cell) are shown. KISP: n=6 mice, KI2-cell pools: n=3. Two-tailed Student's T-test with equal variance; * (P<0.05). Bars represent the mean ± SEM; error bar of the KISP(mIC1) is too small to be seen on the graph. *(B)* Methylation at hIC1 in KISP and hSP1 analyzed by bisulfite treatment followed by sequencing; assays *e-h* are used (Figure 2.2*C*). Cytosines in CG dinucleotides that are conserved between mouse and human and located within CTS are depicted as black lines above the clones and marked as CTS 1,2,3,4, and 6 (Bell and Felsenfeld, 2000). Cytosines measured by pyrosequencing are marked with an asterisk. *(C)* ChIP-qRT-PCR for H3K4me2 and H3K9me3 at the mIC1 and hIC1 in knock-in round spermatids; assays *b* and *j* were used (Figure 2.2*C*). Two independent pools of round spermatids were generated as detailed in Chapter 5.6, and the results from each pool are shown separately. Y-axis denotes the ChIP signal of each histone mark normalized to that of total H3 (e.g. percent input H3K4me2/percent input total H3).

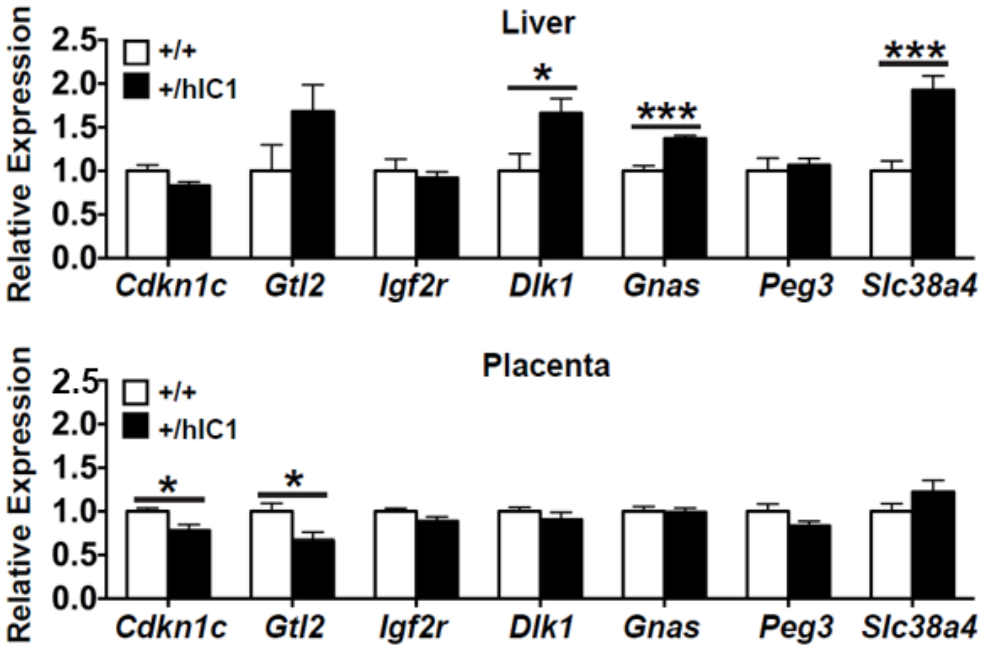

Figure 2.10 Changes in levels of imprinted gene network (IGN) genes in *H19*$^{+/hIC1}$ embryos and placentas. For the y-axis, the mean value of +/+ is arbitrarily set as 1. *(A,B)* +/+: n=8, +/hIC1: n=6 (from two litters). White bars: +/+, black bars: +/hIC1. P-value was calculated using two-tailed Student's T-test with equal variance; * ($P < 0.05$); *** ($P < 0.001$). Bars represent the mean ± SEM.

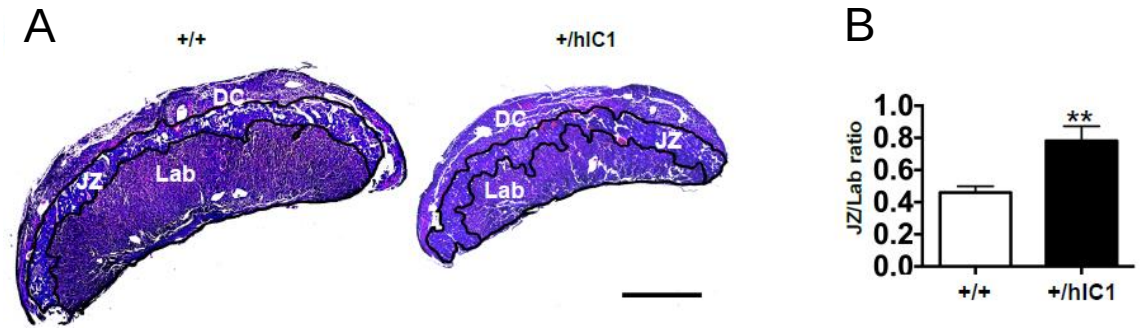

Figure 2.11 Analyses of *H19*$^{+/hIC1}$ placentas. (*A*) Representative cross-sections of E15.5 +/+ and +/hIC1 placentas stained with haematoxylin and eosin. Black lines outline the decidua (DC), junctional zone (JZ), and labyrinthine zone (Lab). Scale bar represents 1000μm. (*B*) Stereological analysis of the junctional zone (JZ) area to labyrinth zone (Lab) area ratio in E15.5 +/+ and +/hIC1 placentas. (*B*) +/+: n=5, +/hIC1: n=4 (from one litter). Two-tailed Student's T-test with equal variance; ** (P<0.01). Bars represent the mean ± SEM.

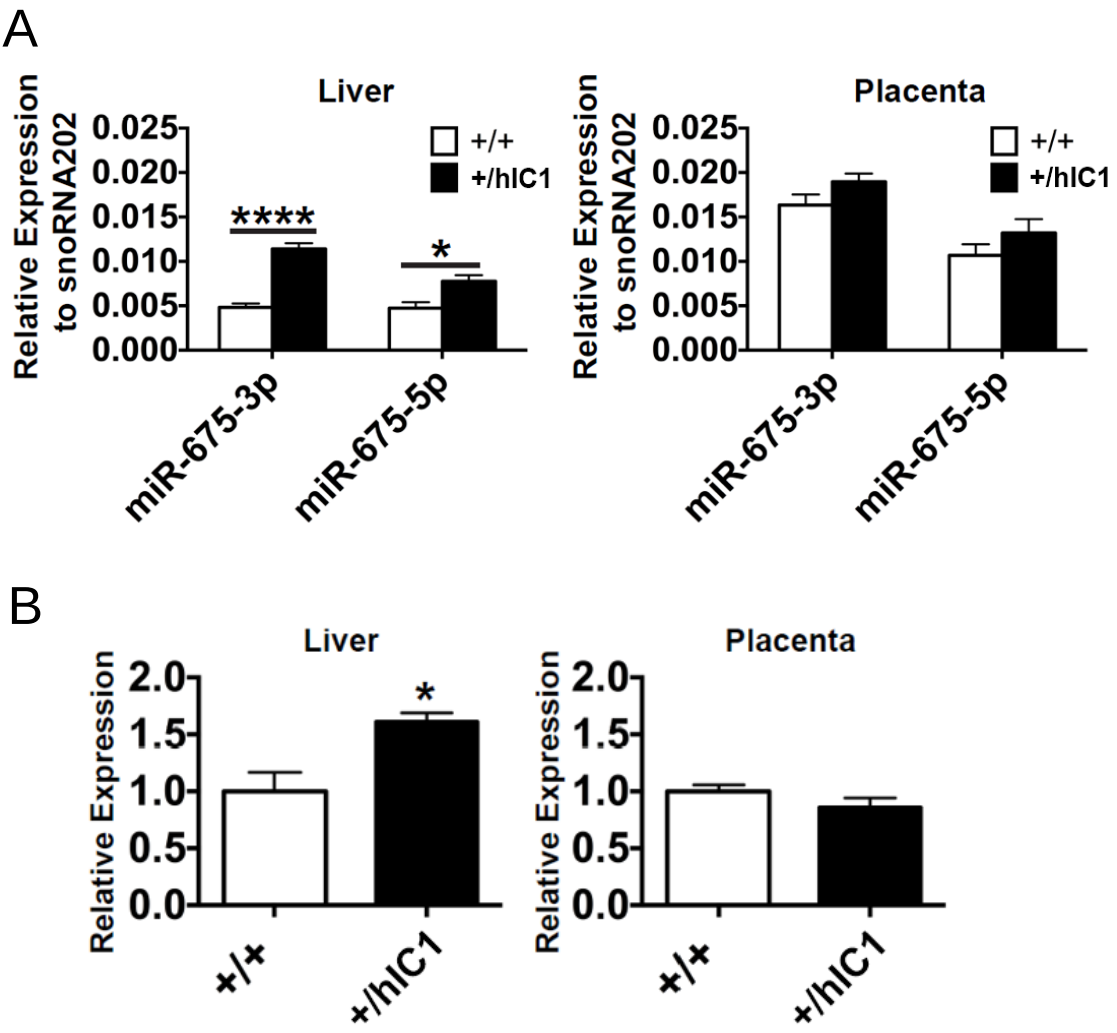

Figure 2.12 Analyses of miR-675 and *Igf1r* in *H19*$^{+/hIC1}$ embryos and placentas. (*A*) Total expression of miR-675-3p and miR-675-5p in E15.5 livers and placentas, normalized to the level of snoRNA202. (*B*) Total expression of *Igf1r* in E15.5 livers and placentas. (*A,B*) +/+: n=8, +/KI: n=6 (from two litters). White bars: +/+, black bars: +/hIC1. (*A,B*) P-value was calculated using two-tailed Student's T-test with equal variance; * ($P < 0.05$); **** ($P < 0.0001$). Bars represent the mean ± SEM.

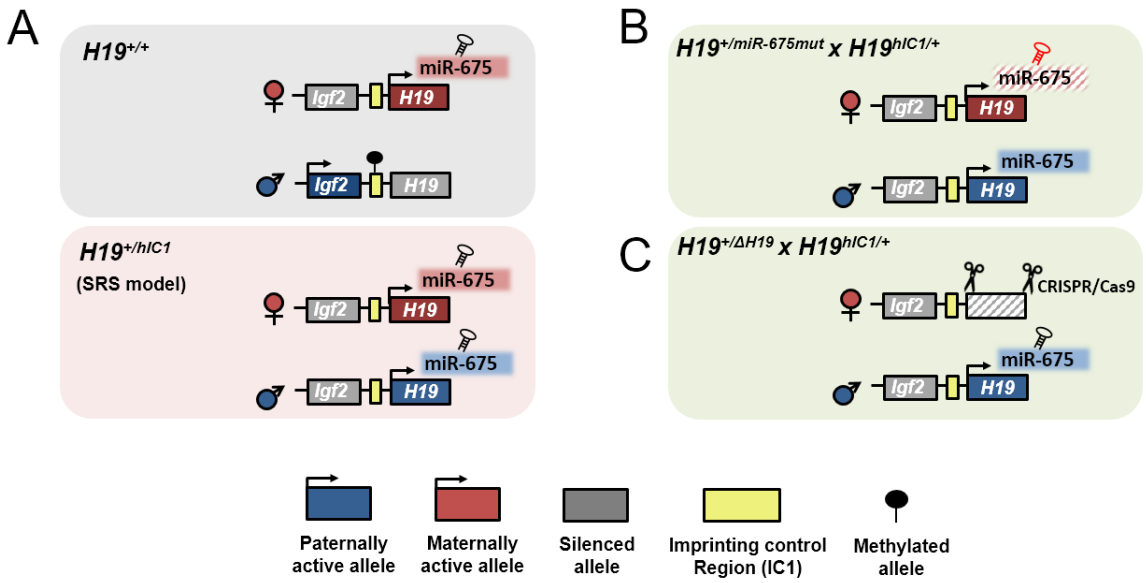

Figure 2.13 Strategies to address the specific role of miR-675 and *H19* in growth regulation. (*A*) Top, *H19/Igf2* regulation in the wild-type ($H19^{+/+}$). Bottom, *H19/Igf2* regulation upon paternal transmission of the $H19^{hIC1}$ allele ($H19^{+/hIC1}$). (*B*) A schematic of a cross between $H19^{+/miR\text{-}675mut}$ female and $H19^{hIC1/+}$ male. (*C*) A schematic of a cross between $H19^{+/\Delta H19}$ female and $H19^{hIC1/+}$ male. (*B,C*) Mutant or deletion alleles are indicated with striped boxes. The parent-of-origin of the allele is indicated with a female(♀) or male (♂) symbol.

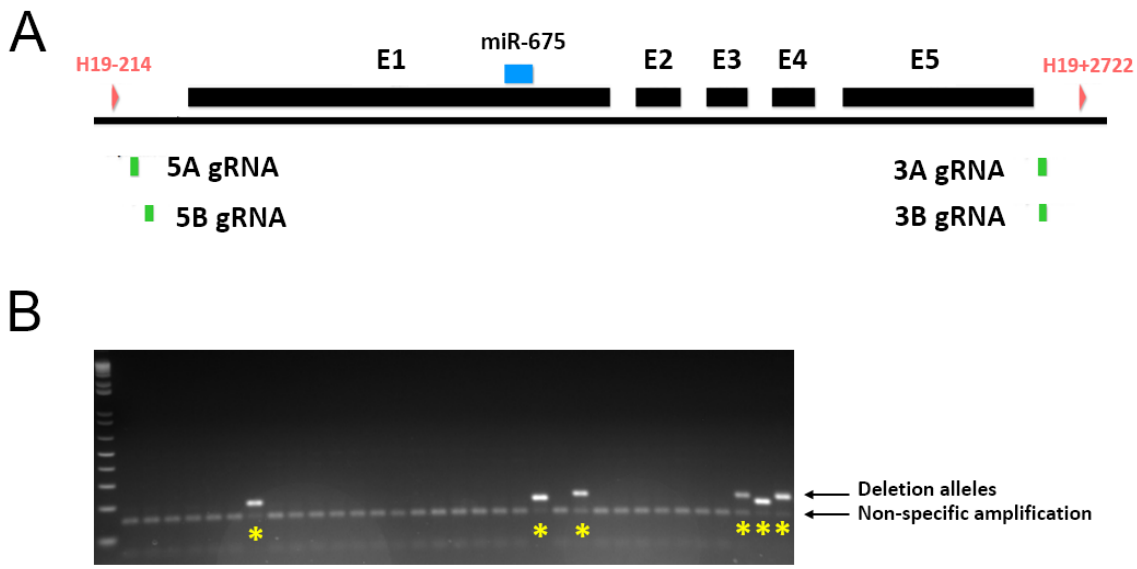

Figure 2.14 CRISPR/Cas9 gRNA designs for deleting the *H19* sequence. (*A*) Shown is the endogenous mouse *H19* (~2.5kb) sequence that is composed of five exons (E). Two pairs of gRNA were designed: pair A (5A gRNA-3A gRNA) and pair B (5B gRNA-3B gRNA). Either pair A or pair B was injected into zygote stage embryos. A set of primer (H19-214 and H19+2722) that was used to genotype the deletion allele is indicated in pink. (*B*) A representative genotyping gel of chimeras. Injection of either pair A or pair B generated chimeras with correct deletions. When the *H19* sequence is successfully deleted, the H19-214 and H19+2722 primer set amplifies ~200-250bp fragments (size may vary depending on the indels generated). The amplified fragments were gel-isolated and sequenced to confirm the deletions. Left most lane: 1kb+ ladder (Invitrogen); lanes indicated with yellow asterisks: deletion alleles, otherwise: wild-type alleles. The non-specific PCR band is indicated.

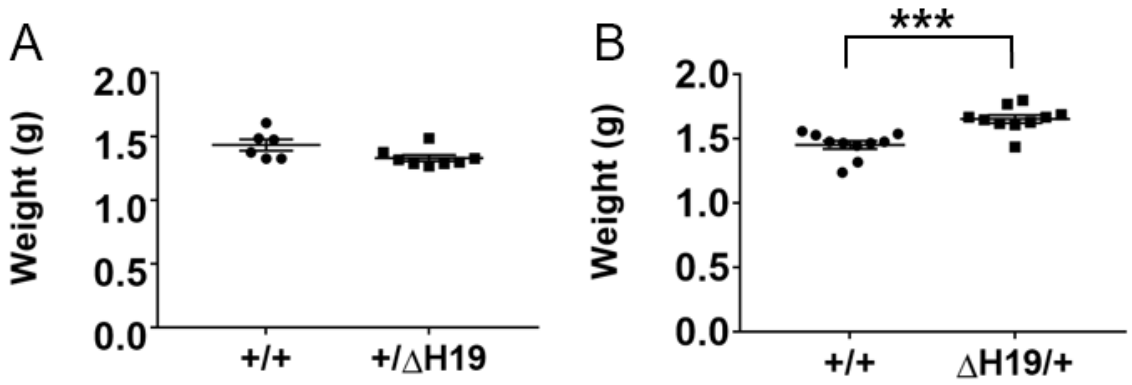

Figure 2.15 day 0 neonatal weight analyses of the *H19$^{\Delta H19}$* allele. (*A*) Paternal transmission of the *H19$^{\Delta H19}$* allele. +/+: n=6, +/△H19: n=8 (from two litters). (*B*) Maternal transmission of the *H19$^{\Delta H19}$* allele. +/+: n=10, △H19/+: n=10 (from three litters). (*A,B*) At least two different chimeric founders (i.e. founder with different length of deletion) were used to generate litters. Each dot or square on the graph represents individual pup. P-value was calculated using two-tailed Student's T-test with equal variance; *** ($P < 0.001$), otherwise, not significant.

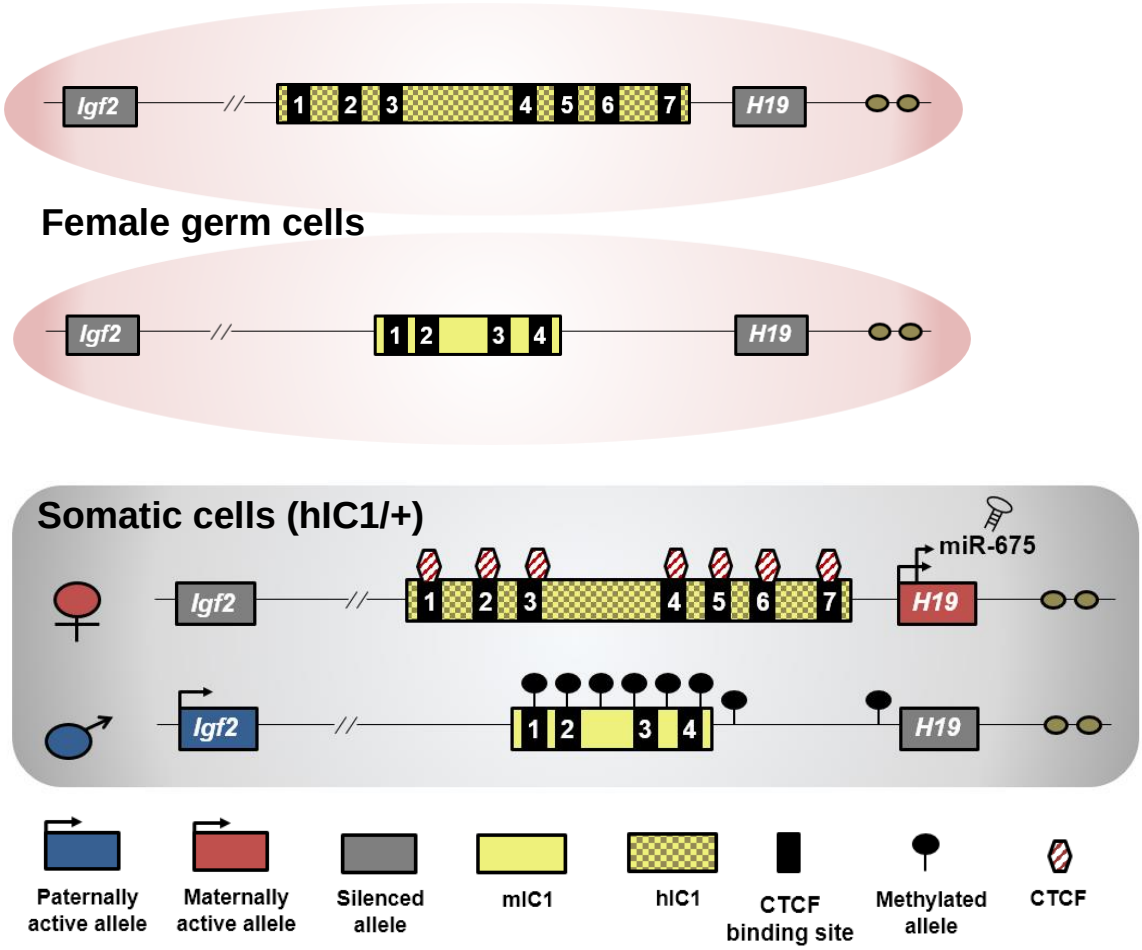

Figure 2.16 Model for maternal transmission of the *H19*^{hIC1} allele. During the female germ cell development, both hIC1 and mIC1 are properly hypomethylated. Once an egg carrying hIC1 is fertilized with a sperm carrying mIC1 and develops into hIC1/+ somatic cells, the CTCF-dependent insulator is properly formed on the maternal hIC1. This leads to the correct imprinted expression of the *H19/Igf2* locus. The parent-of-origin of the allele is indicated with a female(♀) or male (♂) symbol.

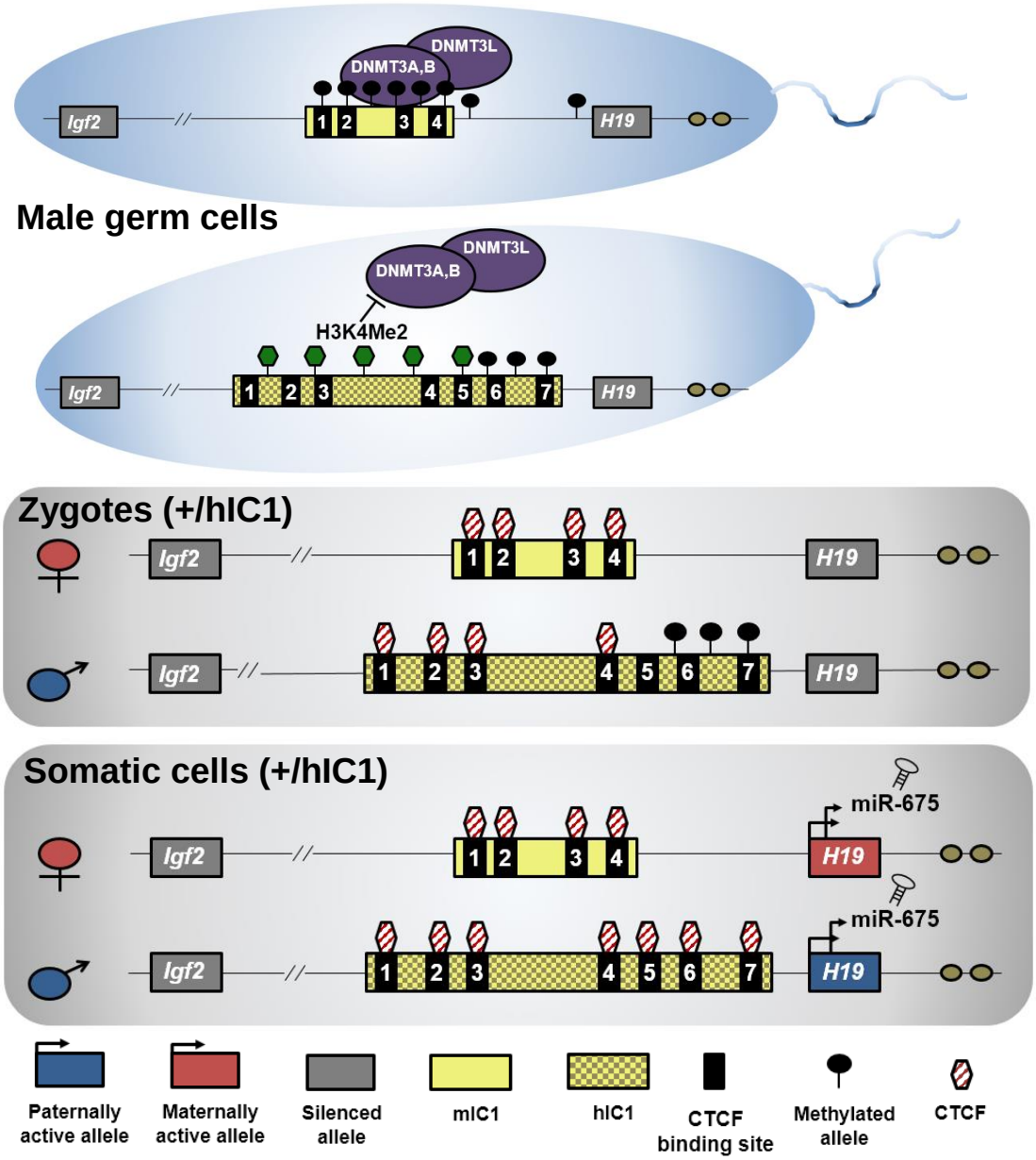

Figure 2.17 Model for paternal transmission of the *H19^{hIC1}* allele. During male germ cell development, unlike mIC1, hIC1 is unusually enriched with H3K4me2, which is inhibitory to the *de novo* DNA methyltransferase machinery. This leaves some regions of hIC1 (that are enriched with H3K4me2) hypomethylated. Once a sperm carrying hIC1 fertilizes an egg carrying mIC1 and develops into a zygote, CTCF binds to the unmethylated CTCF-binding sites at the hIC1. As the zygote undergoes cell division and develops into +/hIC1 somatic cells, the partially established methylation marks at hIC1 are not maintained, leading to a fully hypomethylated state of hIC1. Ultimately, biallelic insulation at the locus is established, resulting in loss of imprinting. The parent-of-origin of the allele is indicated with a female(♀) or male (♂) symbol.

CHAPTER 3.
PATIENT-DERIVED HUMAN CELL BASED MODEL

3.1 Background and study rationale

Patient samples expand our knowledge in imprinting. Investigating various human mutations associated with imprinting disorders can provide additional insights into how imprinting is regulated in human, which can be translated into therapeutic strategies. Importantly, understanding mechanisms underlying mutations such as pUPD11, that are harder to engineer in other model systems, can tremendously benefit from analyzing the patient samples. However, these resources have limitations. First, mosaicism is prevalent among BWS population: pUPD11 patients are mosaic for the genetic mutations (Kalish et al., 2014), and individuals with IC1 microdeletions or OCT4-binding mutations carry mosaic epimutations (Beygo et al., 2013; Demars et al., 2010; Habib et al., 2014; Poole et al., 2012; Prawitt et al., 2005; Sparago et al., 2004). The mosaic background of an individual can obscure the extent to which the specific genetic/epigenetic mutation is sufficient to drive the phenotype of the patient. Second, easily accessible yet disease non-relevant tissues, such as fibroblasts and blood, are not the ideal surrogates to investigate the disease etiology. Thus, developing patient-derived models that are devoid of mosaicism in the context of the disease-relevant cell types is necessary.

iPSC technology allows derivation of clonal cell lines, where each cell line has a uniform genetic and epigenetic background. Subsequently, these cell lines can be differentiated into cell type of interest (Unternaehrer and Daley, 2011). These merits of iPSC technology have led various common and rare disorders to be modeled *in vitro*, including imprinting disorders such as Angelman syndrome and Prader-Willi syndrome (Chamberlain et al., 2010; Cruvinel et al., 2014; Stelzer et al., 2014).

Previous reports have suggested a link between the imprinted genes and pluripotency of stem cells, although no concrete consensus has been reached (Chang et

al., 2014; Stadtfeld et al., 2010, 2012). The correct imprinted status of the *DLK1-DIO3* locus (Figure 3.1) has received a wide attention as a molecular marker for assessing the quality of stem cells (Benetatos et al., 2014). Hypermethylation and/or aberrant silencing of the maternally expressed long non-coding RNAs and microRNAs at the *DLK1-DIO3* locus have been linked to poor developmental potential of mouse iPSCs (Stadtfeld et al., 2010; Stadtfeld et al., 2012), suboptimal pluripotency in mouse ESCs (Liu et al., 2010), and inefficient neural lineage differentiation potential of human ESCs (Mo et al., 2015).

In contrast, Christodoulou *et al*. showed that mouse iPSCs with hypermethylated *Dlk1-Dio3* locus had similar differentiation capacity into definitive endoderm compared to mouse ESCs with normal *Dlk1-Dio3* methylation (Christodoulou et al., 2011). Chang *et al*. noted that hypomethylation of the *Zrsr1* imprinted gene, but not hypermethylation of the *Dlk1-Dio3* locus, is correlated with poor quality of mouse iPSCs (Chang et al., 2014). Thus, the extent to which the *DLK1-DIO3* locus hypermethylation affects iPSC quality requires further investigation.

Other ICRs have infrequently exhibited stochastic aberrant DNA methylation in both mouse and human pluripotent stem cells (Nazor et al., 2012; Nishino et al., 2011; Sun et al., 2012; Takikawa et al., 2013). Overall, these studies emphasize the need for careful examination of the stability of imprinted genes in the pluripotent stem cells. Such inspection is especially crucial for the cell lines that will be used for therapeutic or disease-modeling of imprinting disorders.

Here, we present derivation of the iPSCs from pUPD11 BWS patient fibroblasts (Figure 3.2). We show that genetically-matched pUPD11 and non-pUPD11 iPSCs can be derived from mosaic samples. We primarily analyzed DNA methylation at various imprinted regions in our cell lines, and show that while other regions exhibit proper methylation profile, the *DLK1-DIO3* locus is aberrantly methylated. Although the

significance underlying this molecular phenomenon remains to be determined, the derived cell lines are useful resources that can be further differentiated into clinically-relevant endodermal and mesodermal lineages to examine molecular mechanisms leading to BWS.

3.2 Derivation of iPSCs from mosaic pUPD11 fibroblasts

Skin samples from four male patients were collected during surgical procedures and used to generate fibroblast cell lines. pUPD11 breakpoints as well as extent of mosaicism of pUPD11 for all patients were determined using genome-wide single-nucleotide polymorphism (SNP) microarray analysis (Figure 3.3 and data not shown). To demonstrate that two populations of cells, designated isogenic pUPD11 and non-pUPD11 iPSCs, can be derived from mosaic fibroblast cell lines, we reprogrammed fibroblasts from these patients using either polycistronic STEMCCA lentivirus (Sommer et al., 2009) or episomal plasmids (Okita et al., 2011). As a sex- and cell-type- matched control, we reprogrammed one male fibroblast cell line (IMR91) using episomal plasmids (Figure 3.3). Most of the iPSC-like colonies were isolated, and the clones that thrived for at least three passages were counted and noted in Figure 3.3. All fibroblast cell lines and representative iPSC lines had a normal karyotype (data not shown). The iPSCs expressed similar levels of pluripotency markers and all three embryonic germ layer markers upon differentiation into embryoid bodies (EBs) as measured by qRT-PCR and immunofluorescence (Figure 3.4, 3.5A, and 3.5B), regardless of the reprogramming strategy or the extent of pUPD11 in the parental fibroblasts. To determine which iPSCs had pUPD11 versus biparental chromosome 11, we used microsatellite fragment analyses or restriction fragment length polymorphisms (Table 5.4). Notably, the percent of pUPD11 iPSC clones derived relative to the total number of iPSC clones was

reflective of the percent pUPD11 in the initial fibroblasts (Figure 3.3). We did not obtain any pUPD11 iPSCs from patient 2 fibroblasts (Figure 3.3), likely due to the low level of pUPD11 in the initial fibroblasts. These results demonstrate that pUPD11 and non-pUPD11 iPSCs can be derived from a mosaic patient fibroblast sample.

3.3 Analyses of the pUPD11-relevant ICRs and imprinted genes

DNA methylation status at IC1 and IC2 is the most widely used molecular marker to diagnose BWS (Mussa et al., 2016). Thus, it is essential that iPSCs derived to model BWS display normal and intact methylation profile at both ICRs. To determine that pUPD11 and non-pUPD11 iPSCs reflect the DNA methylation status of the parental fibroblasts, IC1 and IC2 methylation levels were measured. For IC1 methylation analyses, we performed pyrosequencing for patient 1 and 2 cell lines. Due to the presence of SNPs in the pyrosequencing primer binding site for patient 3 and 4 cell lines, combined bisulfite restriction analysis (COBRA) was used. IC2 methylation for all patient lines was analyzed using COBRA. Because pUPD11 iPSCs have two copies of the paternal contribution of the IC1 (Figure 1.8), they exhibited ~100% methylation as expected, and non-pUPD11 iPSCs displayed the expected ~50% methylation (Figure 3.6A). To validate the COBRA results, IC1 methylation in the patient 3 and 4 fibroblast cell lines and select non-pUPD11 and pUPD11 iPSCs was determined using bisulfite treatment followed by direct sequencing. The sequencing results replicated the COBRA results (Figure 3.6B). Because the paternally inherited IC2 is normally unmethylated, as expected, all pUPD11 iPSCs analyzed showed no detectable methylation at IC2 (Figure 3.7), whereas non-pUPD11 iPSCs showed normal methylation. Therefore, IC1 and IC2 methylation status is appropriate for the parent-of-origin and is maintained after the derivation and culture of iPSCs.

To investigate whether DNA methylation is stably maintained across multiple passages, select patient 1 and 2 iPSCs were cultured over prolonged periods. All iPSCs maintained stable IC1 methylation pattern in later passages (Figure 3.8), demonstrating that the reprogramming and/or culture conditions for iPSCs does not perturb IC1 methylation in our study.

Next, we evaluated expression of imprinted genes in the pUPD11 region. Because *H19* and *Igf2* are lowly expressed in the mouse blastocysts (Lee et al., 1990; Poirier et al., 1991), we did not expect to observe high levels of expression of these genes in iPSCs. Consistently, expression of both genes was low in iPSCs. Therefore, we differentiated iPSCs into EBs to examine *H19* and *IGF2* RNA levels. pUPD11 EBs displayed no expression of *H19*, whereas non-pUPD11 EBs expressed *H19*. Furthermore, pUPD11 EBs expressed higher levels of *IGF2* compared to the non-pUPD11 EBs (Figure 3.9). These results demonstrate that *H19* and *IGF2* mRNA in EBs appropriately reflect their non-pUPD11 versus pUPD11 statuses of their counterpart iPSCs.

3.4 Analyses of DNA methylation at other ICRs

We also analyzed imprinted loci outside of the pUPD11 region. First, we analyzed DNA methylation at the *SNRPN* ICR, implicated in Prader-Willi syndrome (Cassidy et al., 2012) using pyrosequencing. All iPSCs showed normal methylation levels at the *SNRPN* ICR similar to the level detected in the parental fibroblasts (Figure 3.10). Hence, reprogramming strategies employed in the current study lead to stable methylation status at the *SNRPN* ICR.

Next, we examined the *DLK1-DIO3* locus using pyrosequencing. Here, we analyzed two DMRs—the intergenic differentially methylated region (IG-DMR), which

serves as the locus ICR, and the *MEG3*-DMR, a paternally methylated sequence that reflects the *MEG3* imprinted expression (Figure 3.1) (Benetatos et al., 2014). Consistent with previous reports, many iPSC clones were abnormally hypermethylated at the *DLK1-DIO3* locus, in contrast to their initial parental fibroblasts, which were normally methylated (Figure 3.11A). To address whether prolonged culture had additional effects on DNA methylation stability at the locus, select patient 1 and 2 iPSCs were cultured over prolonged periods. Some clones (i.e. patient 1 clone 43, patient 2 clones 68 and 76) became hypermethylated over extended culture at one or both DMRs (Figure 3.11B), suggesting that aberrant methylation can manifest during prolonged culture. We also observed that different aliquots of the same iPSC line thawed independently exhibited variable DNA methylation patterns (data not shown). Nevertheless, some clones (i.e. patient 1 clone 9 and patient 2 clone 61) maintained normal methylation for 7-10 passages (Figure 3.11B). Overall, these results suggest that the *DLK1-DIO3* locus is especially sensitive to DNA methylation perturbation during iPSC reprogramming and/or culture.

3.5 The effect of vitamin C in ICR methylation

Several groups have advocated the use of vitamin C (VC) supplementation during iPSC reprogramming for enhancing the efficiency of reprogramming and/or generating high-quality mouse and human iPSCs (Chen et al., 2013; Esteban et al., 2010; Stadtfeld et al., 2012; Xu et al., 2015). To this end, we reprogrammed the IMR91 fibroblast cell line with (+VC) or without VC (-VC) in parallel experiments; 18+VC and 17-VC IMR91 iPSC clones were isolated (Figure 3.3). The efficiency of expanding viable clones was the same regardless of VC exposure. IC1, IC2, and *SNRPN* ICR maintained normal methylation levels in the IMR91 iPSCs regardless of VC treatment (Figure 3.12A

and B). Interestingly, we noticed that VC leads to an initial, average, lower methylation level at both IG-DMR and *MEG3*-DMR in iPSCs (Figure 3.13A). All clones examined, however, became hypermethylated at IG-DMR and *MEG3*-DMR in later passages, irrespective of the VC treatment (Figure 3.13B).

3.4 Discussion

In this study, we report the establishment of iPSC models of BWS. We derived both pUPD11 and non-pUPD11 iPSCs from three BWS patient fibroblast cell lines that have distinct pUPD11 regions and differing levels of mosaicism for pUPD11 in the parental fibroblasts. In each reprogramming experiment, the non-pUPD11 iPSCs serve as internal controls for pUPD11 iPSCs, as the cell lines are isogenic except for the pUPD11 regions. The use of matched iPSCs to study human diseases diminishes potential background effects caused by genetic variations between individuals. To our knowledge, these lines are the first iPSC models of BWS, thus a valuable tool to study the mechanisms of IC1 and IC2 imprinting in BWS.

Importantly, we showed that the proportion of the pUPD11 iPSC lines relative to the total iPSC lines reflects the percent of pUPD11 cells in the patient fibroblasts. These results suggest that during reprogramming, the pUPD11 cells do not have growth advantages, even though the growth-promoting gene, *IGF2*, is overrepresented and the growth-suppressing genes, *CDKN1C* and *H19* are repressed in these cells. Lack of a growth advantage is likely due to relatively low expression of the genes during the reprogramming process and propagation of iPSCs, as we showed that *H19* and *IGF2* expression is low in the iPSCs yet increased upon differentiation into EBs. Similarly, *CDKN1C* is significantly upregulated upon human ESCs differentiation into EBs (Bhattacharya et al., 2005).

We examined DNA methylation at five DMRs in the iPSCs: IC1, IC2, *SNRPN* ICR, IG-DMR, and *MEG3*-DMR, and showed that methylation was properly maintained at IC1, IC2 and *SNRPN* ICR. However, we observed a prevalence of hypermethylation at the *DLK1-DIO3* locus in the iPSCs, as reported by others (Benetatos et al., 2014). To what extent the *DLK1-DIO3* locus hypermethylation affects human iPSC quality remains unclear. Mo *et al*. inferred that hypermethylation at the *DLK1-DIO3* locus results in inefficient ectodermal differentiation (Mo et al., 2015). However, EB samples differentiated from the non-pUPD11 and pUPD11 iPSCs with hypermethylated *DLK1-DIO3* locus expressed similar levels of the ectodermal markers compared to the EB sample (patient 1, pUPD11 clone 9) differentiated from the iPSCs with a normal *DLK1-DIO3* methylation. The discrepancy between the two studies may be attributed to the different cell sources (human ESCs vs iPSCs) and culture techniques. Nevertheless, appropriate expression of germ lineage markers in all EBs analyzed suggests that our iPSCs have normal differentiation potential into all three germ lineages independent of the methylation status at the *DLK1-DIOS* locus.

We showed that the VC supplementation during iPSC reprogramming was associated with a significantly lower methylation level at the *DLK1-DIO3* locus in the early passage iPSCs compared to the iPSCs derived without VC supplementation, consistent with the results obtained by Stadtfeld *et al*. where addition of VC during reprogramming suppressed hypermethylation at the *Dlk1-Dio3* locus in mouse iPSCs (Stadtfeld et al., 2012). However, in our study, the iPSCs in the +VC group became hypermethylated over extended culture. Whether the mouse iPSCs with normal *Dlk1-Dio3* methylation in the study by Stadtfeld *et al*. maintained their methylation over extended culture is unclear. However, it is possible that VC affects the mouse and

human *DLK1-DIO3* locus differently, through its influence on multiple epigenetic regulators such as histone demethylases and DNA demethylases (Blaschke et al., 2013; Chen et al., 2013; Eid and Abdel-Rehim, 2016; Gao et al., 2015; Shi et al., 2010; Wang et al., 2011).

3.5 Contributions

The work described in this chapter is a collaborative effort. Dr. Jennifer Kalish collected the patient samples, performed SNP array, and provided general advice for the project. Dr. Montserrat Anguera provided pivotal guidance in deriving and characterizing iPSCs. Dr. Joanne Thorvaldsen performed iPSC reprogramming. Dr. Dong Hun Woo, currently at the NEXEL Co., Ltd, Seoul, Korea, provided STEMCCA lentivirus. Suhee Chang, from the laboratory of Dr. Marisa Bartolomei, Carolyn Lye, currently at the Yale medical school, and Alice Yu, from the laboratory of Dr. Jennifer Kalish, assisted in various aspects of iPSC characterization. Dr. Joanne Thorvaldsen and Suhee Chang have significantly contributed in expanding and analyzing iPSCs.

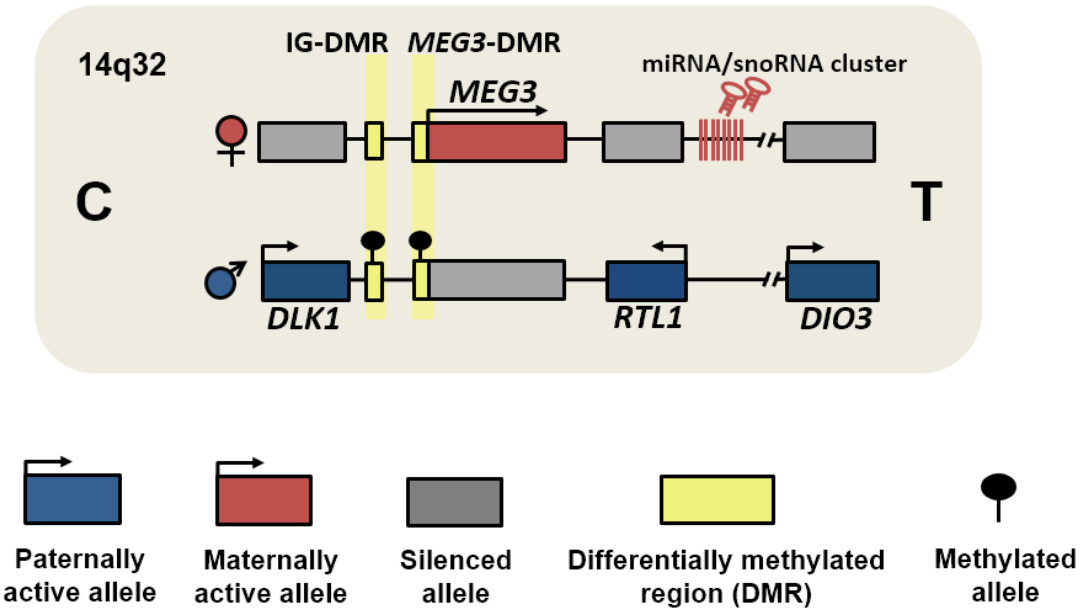

Figure 3.1 *DLK1-DIO3* imprinted locus in human 14q32. On the maternal allele (♀), lncRNA *MEG3* as well as a large cluster of miRNAs and snoRNA are active. On the paternal allele (♂), protein-coding genes including *DLK1, RTL1,* and *DIO3* are expressed. The IG-DMR serves as the ICR for the locus, and DNA methylation at the *MEG3*-DMR is established in the somatic cells. Both IG-DMR and *MEG3*-DMR are methylated on the paternal allele. Centromeric (C) and telomeric (T) ends are indicated. Not drawn to scale.

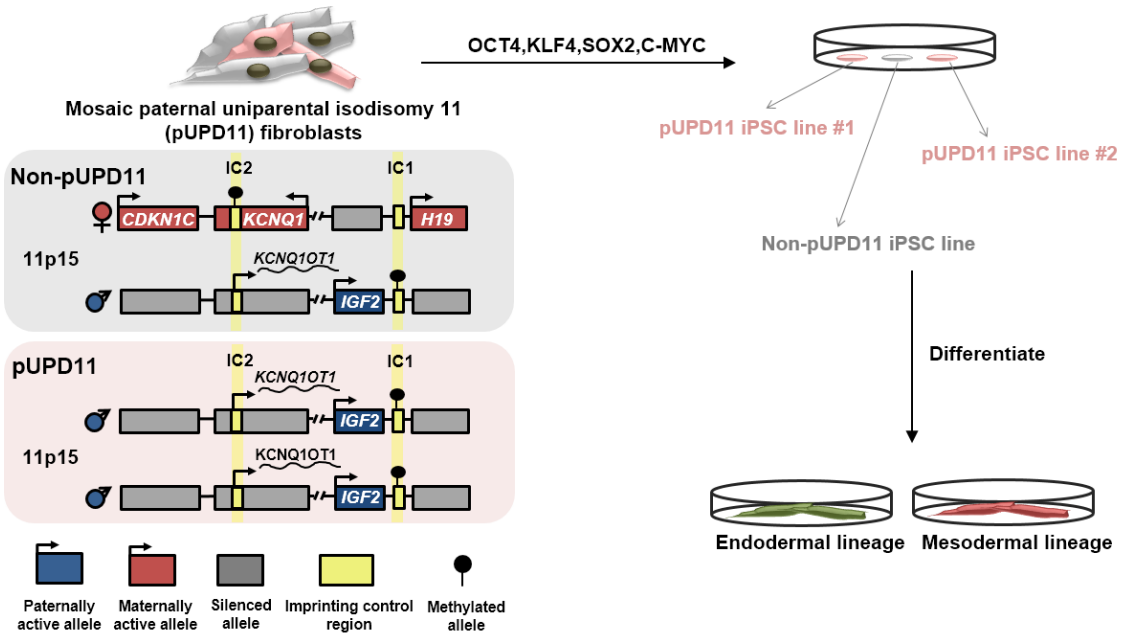

Figure 3.2 A schematic of pUPD11 fibroblasts reprogramming. Mosaic pUPD11 fibroblasts consist of both non-pUPD11 (represented in grey) and pUPD11 (represented in pink) cells. When these fibroblasts are reprogrammed using the four Yamanaka factors (OCT4, KLF4, SOX2, C-MYC) (Takahashi and Yamanaka, 2006), cell lines that are purely non-pUPD11 or pUPD11 are derived. These iPSCs can be differentiated into lineage of interest, such as endoderm or mesoderm.

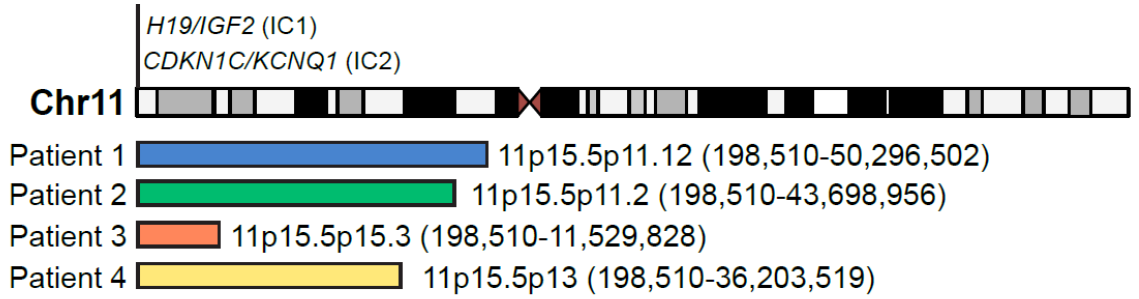

	% pUPD11 in skin	Method of Reprogramming	Vitamin C	Total number iPSC clones derived	Number non-pUPD11 clones	Number pUPD11 clones
Patient 1	60-65%	STEMCCA lentivirus	-	13	6	7
Patient 2	5-10%	Episomal plasmids	-	38	38	0
Patient 3	30%	Episomal plasmids	+	12	9	3
Patient 4	20-25%	Episomal plasmids	+	15	12	3
IMR91	NA	Episomal plasmids	-/+	35	NA	NA

Figure 3.3 Summary of iPSC reprogramming in this study. A schematic illustrating chromosome 11 with relative locations of IC1 and IC2 as well as regions of pUPD11 (colored retangles) of each pUPD11 fibroblast cell line (Patient 1, 2, 3, 4). pUPD11 break points are indicated next to regions of pUPD11 (Human Genome Build 37, hg19, 2009). Percent pUPD11 in the parental fibroblasts, methods of reprogramming, use of vitamin C during reprogramming, and numbers of total, non-pUPD11, and pUPD11 iPSC clones derived, of four pUPD11 fibroblast cell lines and one control fibroblast cell line (IMR91) are summarized. NA: not applicable.

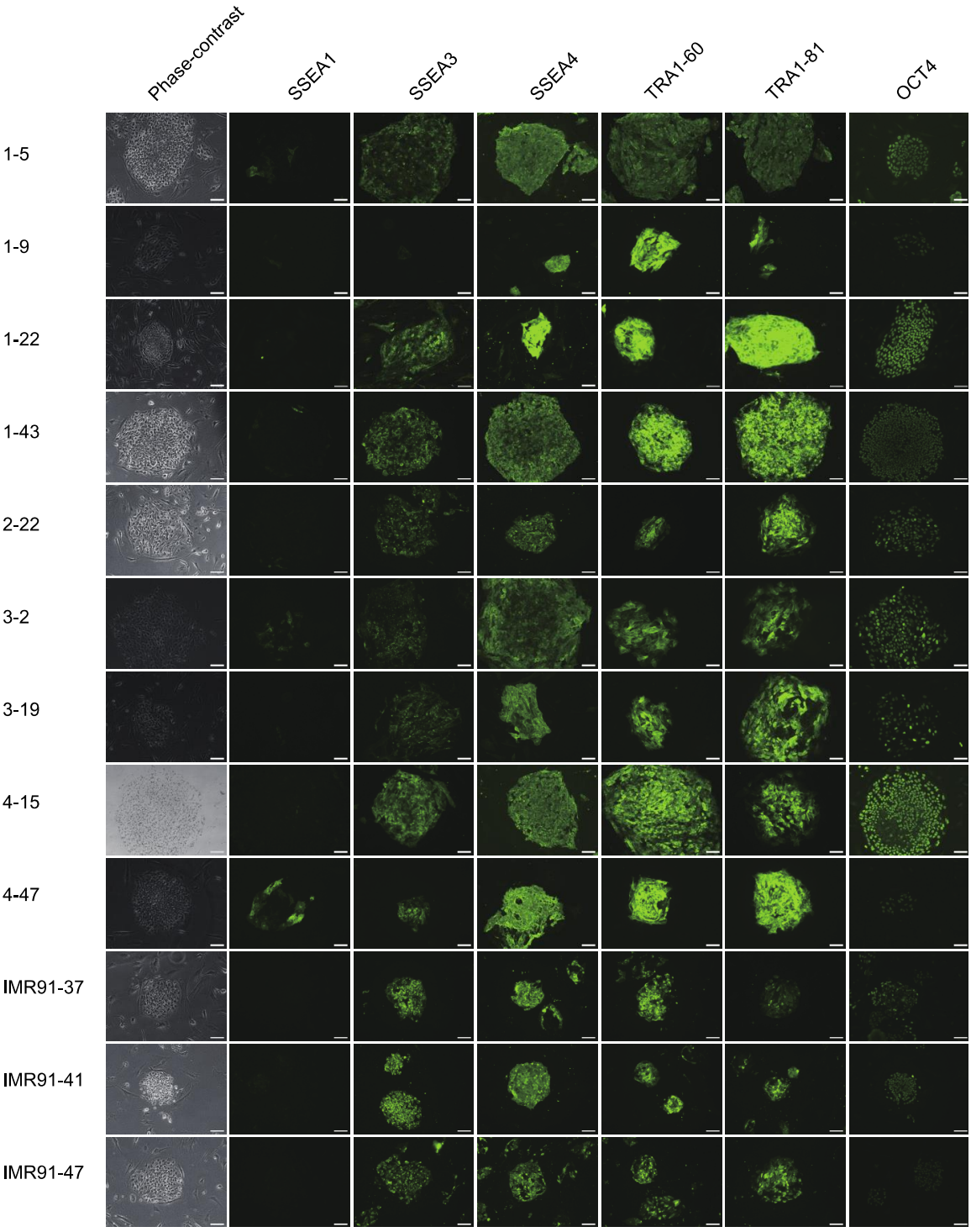

Figure 3.4 Phase-contrast and immunofluorescence images of human iPSCs. Expression of pluripotency markers (SSEA3, SSEA4, TRA1-60, TRA1-81 and OCT4) in select iPSC clones. SSEA1 was used as a negative control cell surface marker for iPSCs. Scale bars, 100μm.

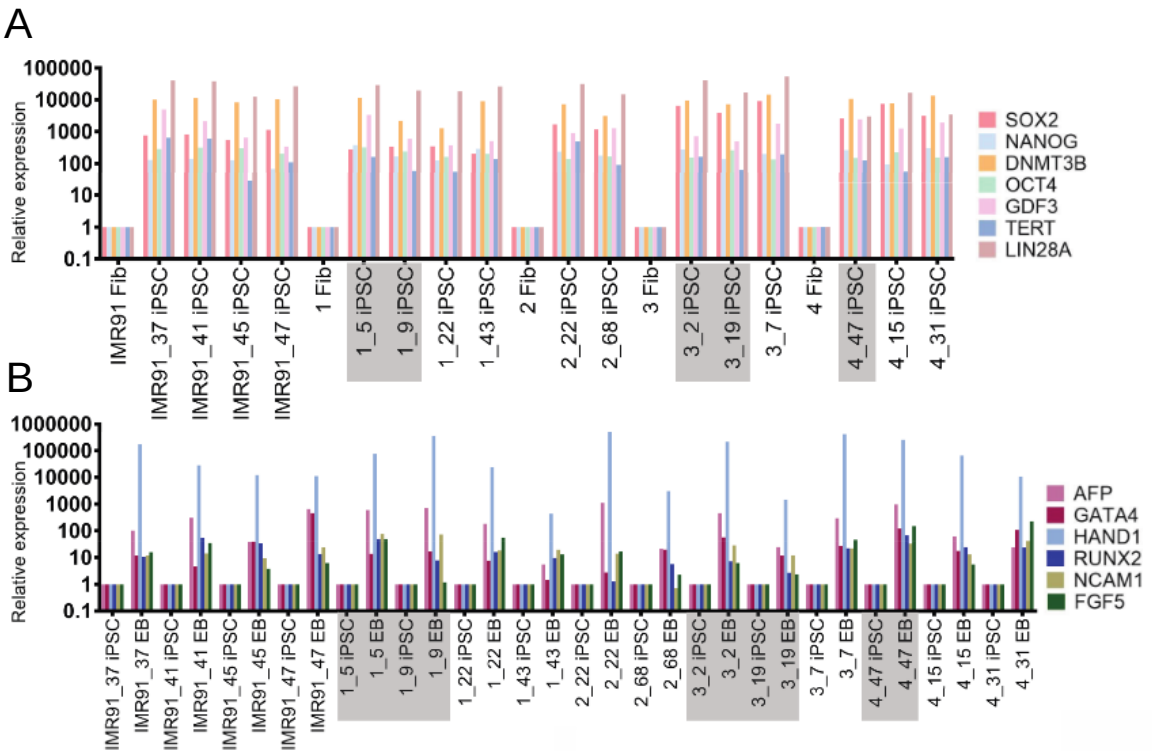

Figure 3.5 Expression of pluripotency markers in iPSCs and expression of germ lineage markers, *H19*, and *IGF2* in EBs. (*A*) Expression of pluripotency markers in the iPSCs was measured by qRT-PCR. Expression in the iPSCs were normalized to expression in the respective parental fibroblasts (set to 1). Fib: fibroblasts. (*B*) Expression of germ lineage markers in the EBs measured by qRT-PCR. Endoderm markers: *AFP* and *GATA4*; mesoderm markers: *HAND1* and *RUNX2*; ectoderm markers: *NACM1* and *FGF5*. Expression in the EBs were normalized to expression in the counterpart iPSCs (set to 1). (*A,B*) Labels on X-axis denote patient number/IMR91 followed by clone number (i.e. 1_5: patient 1 clone 5, IMR91_37: IMR91 clone 37). Y-axis is in log base 10 scale. pUPD11 clones are highlighted in grey boxes; otherwise, non-pUPD11.

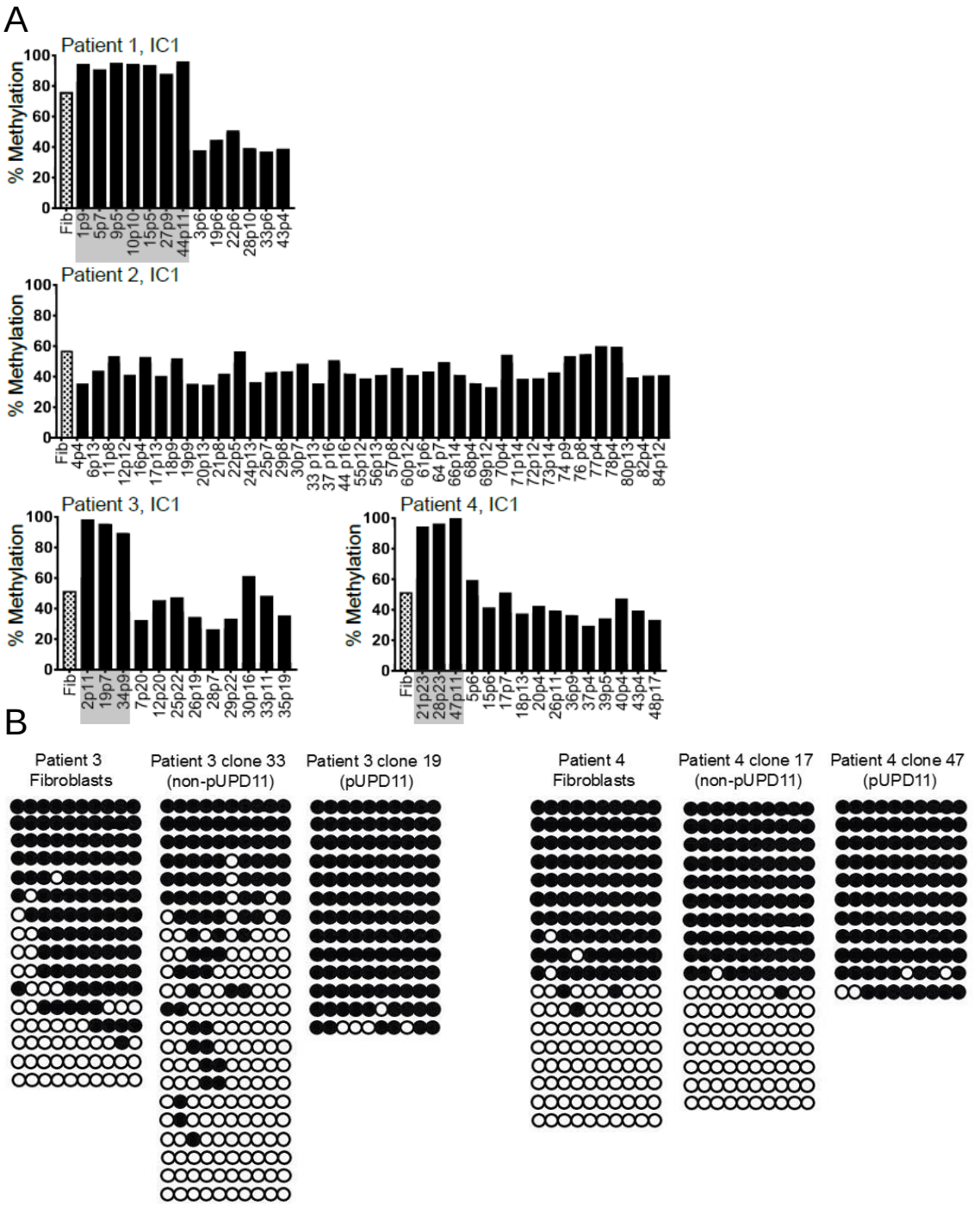

Figure 3.6 Methylation at IC1 in iPSCs and fibroblasts. (*A*) Methylation at IC1 was measured by pyrosequencing (in patient 1 and 2 cell lines) and COBRA (in patient 3 and 4 cell lines). Each graph includes results from the parental fibroblast cell line (dotted bar) and hiPSCs derived from the respective fibroblast cell line (solid bars). Labels on X-axis denote clone number followed by passage number (i.e. 1p9: clone number 1 at passage 9). pUPD11 clones are highlighted in grey boxes; otherwise, non-pUPD11. (*B*) IC1 methylation of patient 3 and 4 fibroblasts and iPSCs measured by bisulfite treatment followed by direct sequencing.

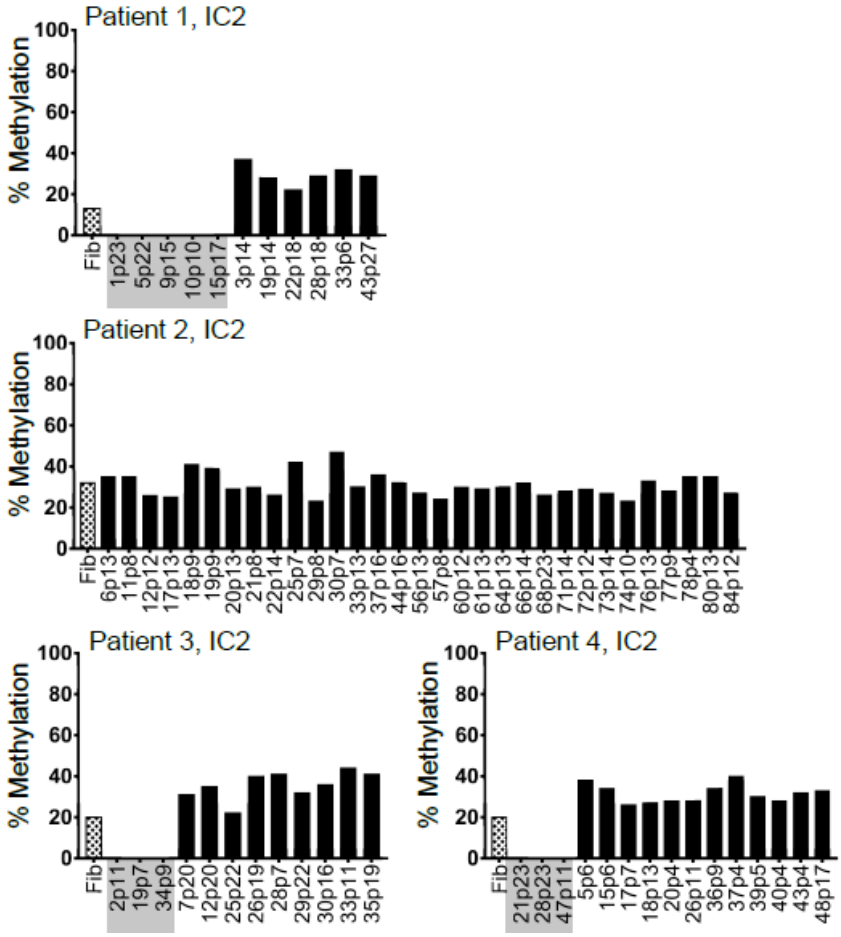

Figure 3.7 Methylation at IC2 in iPSCs and fibroblasts. All samples were analyzed by COBRA. Bars for the pUPD11 iPSCs are too small to be seen on the graph. Each graph includes results from the parental fibroblast cell line (dotted bar) and hiPSCs derived from the respective fibroblast cell line (solid bars). Labels on X-axis denote clone number followed by passage number (i.e. 1p9: clone number 1 at passage 9). pUPD11 clones are highlighted in grey boxes; otherwise, non-pUPD11.

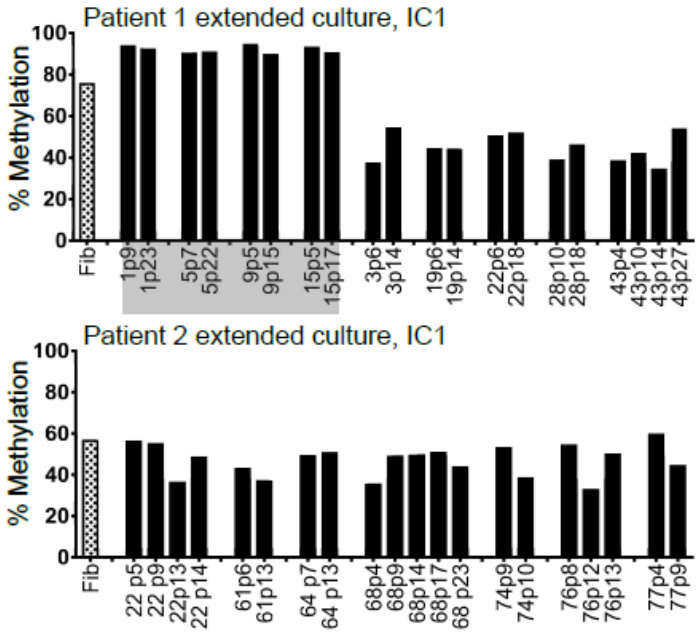

Figure 3.8 Methylation at IC1 in select patient 1 and 2 iPSCs during extended culture. Bars are grouped by clones. Each graph includes results from the parental fibroblast cell line (dotted bar) and hiPSCs derived from the respective fibroblast cell line (solid bars). Labels on X-axis denote clone number followed by passage number (i.e. 1p9: clone number 1 at passage 9). pUPD11 clones are highlighted in grey boxes; otherwise, non-pUPD11.

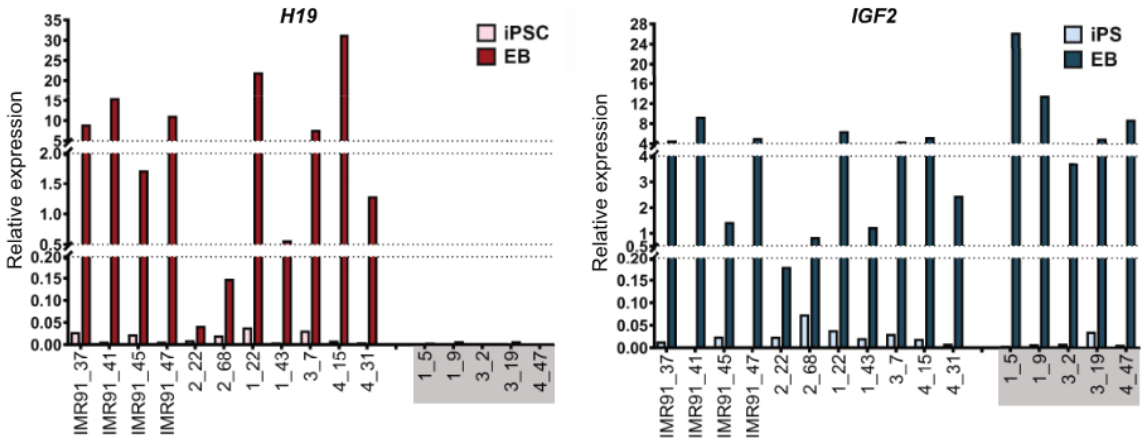

Figure 3.9 Expression of *H19* and *IGF2* in iPSCs and EBs measured by qRT-PCR. *H19* expression (left graph) in the iPSCs are indicated in light red bars and EBs in dark red bars. *IGF2* expression (right graph) in the iPSCs are indicated in light blue bars and EBs in dark blue bars. Note scale breaks on the y-axes for both graphs. Bars for the pUPD11 clones as well as some iPSCs on the left graph are too small to be seen. Some bars for the iPSCs on the right graph are too small to be seen. Labels on X-axis denote patient number/IMR91 followed by clone number (i.e. 1_5: patient 1 clone 5, IMR91_37: IMR91 clone 37). pUPD11 clones are highlighted in grey boxes; otherwise, non-pUPD11.

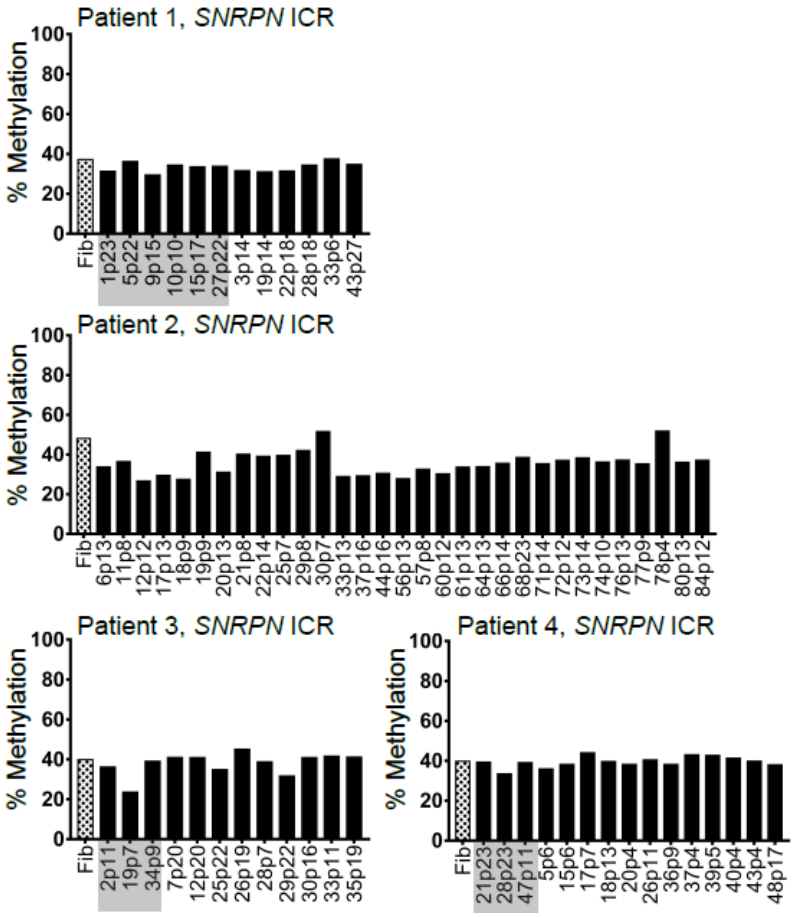

Figure 3.10 Methylation at *SNRPN* ICR in iPSCs and fibroblasts. All samples were analyzed by pyrosequencing. Each graph includes results from the parental fibroblast cell line (dotted bar) and hiPSCs derived from the respective fibroblast cell line (solid bars). Labels on X-axis denote clone number followed by passage number (i.e. 1p9: clone number 1 at passage 9). pUPD11 clones are highlighted in grey boxes; otherwise, non-pUPD11.

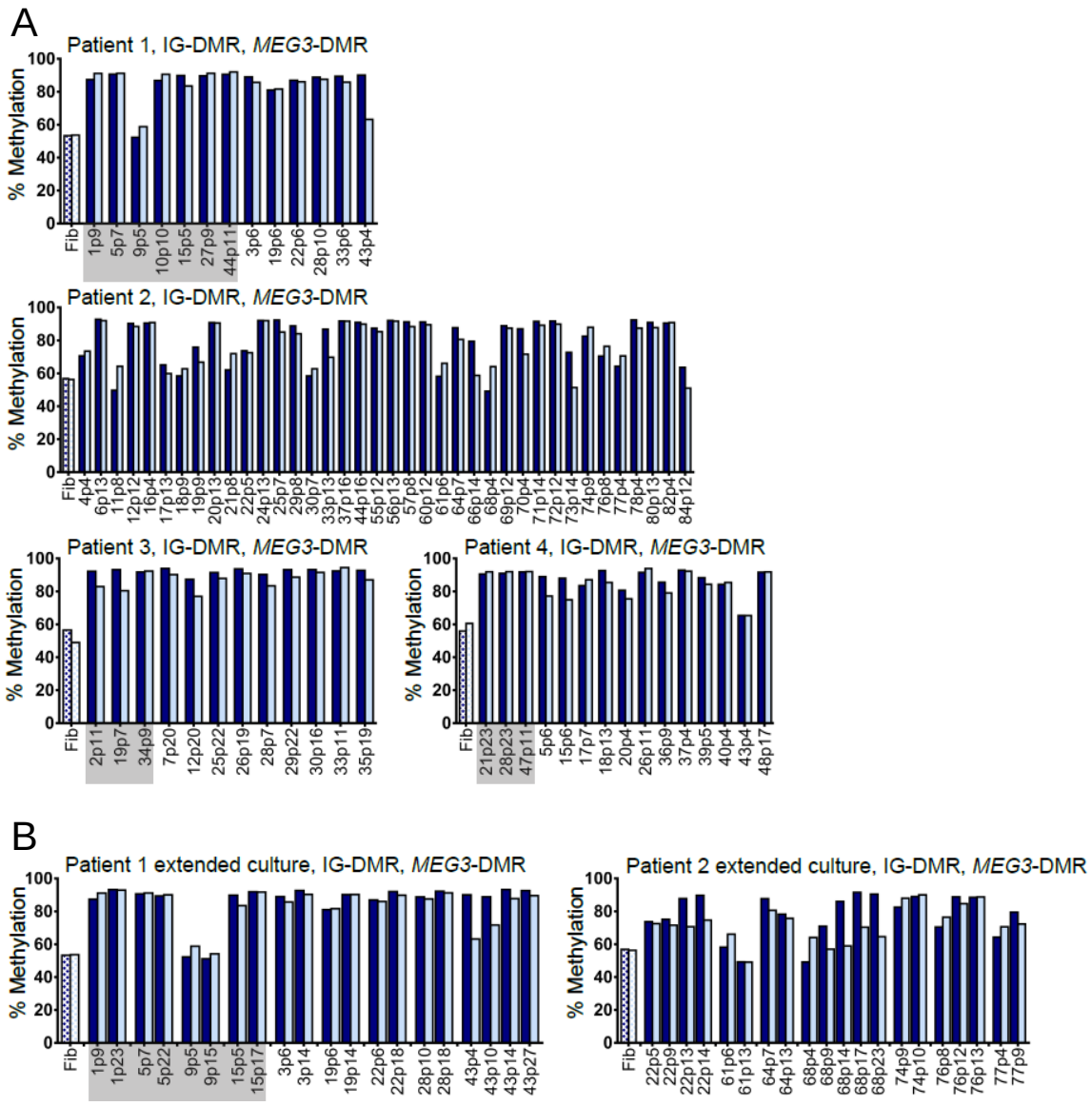

Figure 3.11 Methylation at IG-DMR and *MEG3*-DMR in iPSCs and fibroblasts. Methylation at IG-DMR and *MEG3*-DMR were analyzed by pyrosequencing. (*A*) Methylatoin at IG-DMR and MEG3-DMR in all patient cell ilnes (*B*) Methylation at IG-DMR and *MEG3*-DMR in select patient 1 and 2 iPSCs during extended culture. Bars are grouped by clones. (*A,B*) pUPD11 clones are highlighted in grey boxes; otherwise, non-pUPD11. Methylation at IG-DMR is indicated in dark blue bars and *MEG3*-DMR in light blue bars. Each graph includes results from the parental fibroblast cell line (dotted bar) and hiPSCs derived from the respective fibroblast cell line (solid bars). Labels on X-axis denote clone number followed by passage number (i.e. 1p9: clone number 1 at passage 9). pUPD11 clones are highlighted in grey boxes; otherwise, non-pUPD11.

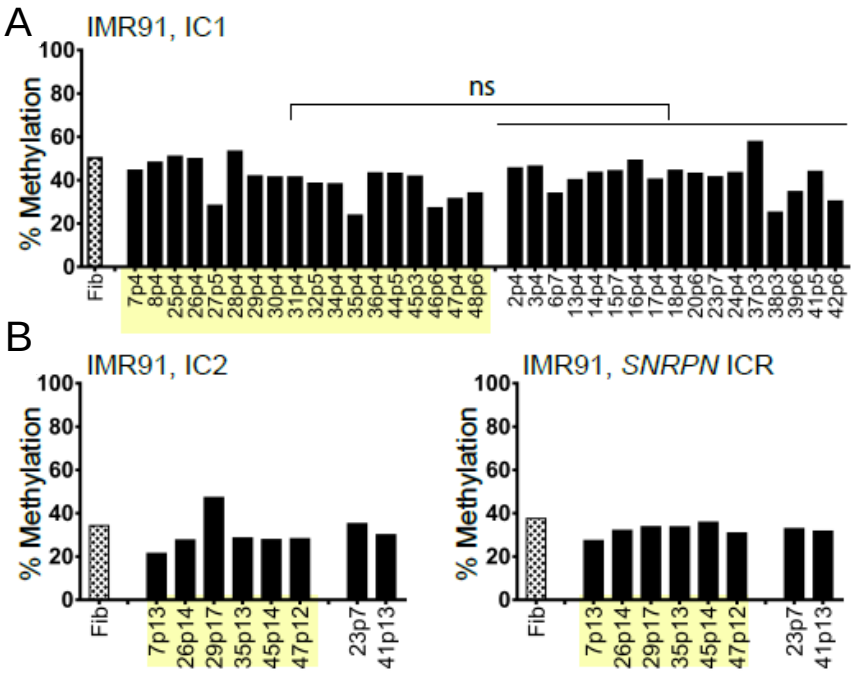

Figure 3.12 IC1, IC2, and *SNRPN* ICR methylation in IMR91 iPSCs derived from +VC or -VC reprogramming. (*A*) Methylation at IC1 was measured by pyrosequencing. ns, not significant; two-tailed student's t test with unequal variance. (*B*) Methylation at IC2 and *SNRPN* ICR was measured by COBRA and pyrosequencing, respectively. (*A,B*) iPSCs derived from +VC reprogramming are highlighted in yellow boxes; otherwise, derived from -VC reprogramming. Each graph includes results from the parental fibroblast cell line (dotted bar) and hiPSCs derived from the respective fibroblast cell line (solid bars). Labels on X-axis denote clone number followed by passage number (i.e. 1p9: clone number 1 at passage 9).

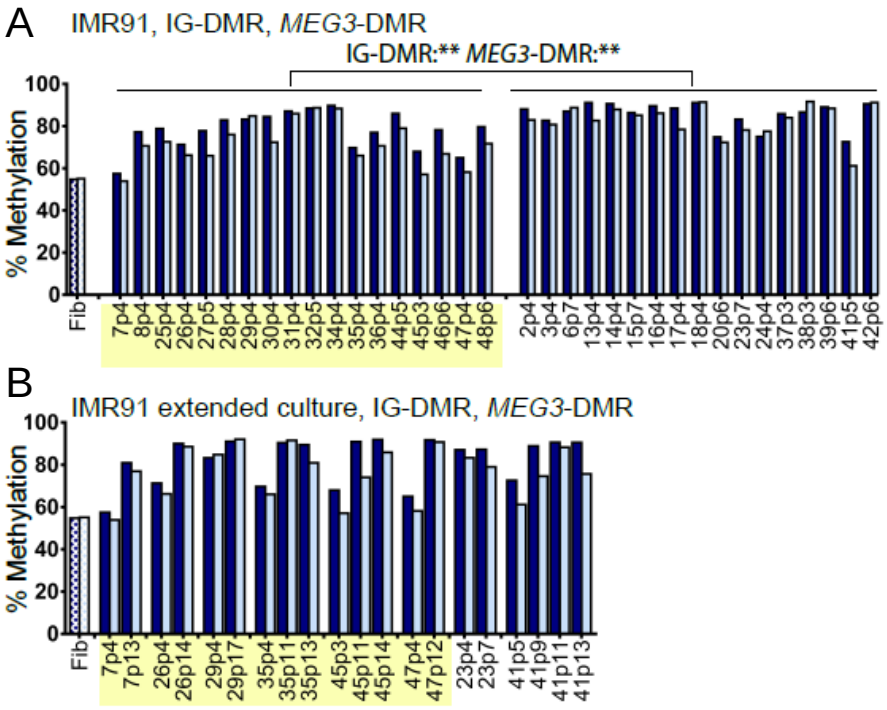

Figure 3.13 *DLK1-DIO3* locus methylation in IMR91 iPSCs derived from +VC or -VC reprogramming. (*A*) Methylation at IG-DMR and *MEG3*-DMR was measured by pyrosequencing. **, p<0.01; two-tailed student's t test with unequal variance. (*B*) Methylation at IG-DMR and *MEG3*-DMR in select iPSCs during extended culture. Bars are grouped by clones. (*A,B*) iPSCs derived from +VC reprogramming are highlighted in yellow boxes; otherwise, derived from -VC reprogramming. Methylation at IG-DMR is indicated in dark blue bars and *MEG3*-DMR in light blue bars. Each graph includes results from the parental fibroblast cell line (dotted bar) and hiPSCs derived from the respective fibroblast cell line (solid bars). Labels on X-axis denote clone number followed by passage number (i.e. 1p9: clone number 1 at passage 9).

CHAPTER 4.
FUTURE DIRECTIONS

4.1 Humanized mouse model

Disease modeling of BWS

IC1 alterations associated with BWS manifest clinical phenotypes when the mutant allele is maternal in origin (Figure 1.7). It is thought that the disrupted insulator function of IC1 on the maternal allele leads to biallelic expression of *IGF2* and reduced *H19* expression, contributing to the overgrowth phenotype. Interestingly, however, these alterations exhibit mosaic gain of methylation at IC1, suggesting that not all cells are aberrantly DNA methylated (Sparago et al., 2004; Prawitt et al., 2005; Beygo et al., 2013; Poole et al., 2012; Demars et al., 2010; Abi Habib et al., 2014). In addition, the penetrance of BWS clinical features ranges from no apparent phenotypes to severe growth defects (Beygo et al., 2013; Abi Habib et al., 2014). Thus, it is challenging to address if the genetic lesions are sufficient to cause abnormal IC1 hypermethylation, deregulation of *H19/IGF2* imprinting, and/or development of BWS. The correlation between methylation changes and genetic lesions suggest heritability of pathological epigenotype, making the molecular investigation of these mutations particularly important.

In this study, we showed that maternal transmission of hIC1 can functionally replace mIC1, by properly regulating imprinted expression and hIC1 methylation. Thus, our finding poses the exciting possibility of modeling IC1 mutations associated with BWS (Figure 1.7) in mouse via maternal transmission. This endeavor has been initiated in collaboration with the laboratory of Dr. Andrea Riccio. Mouse models with 1.8kb and 2.2kb IC1 microdeletions (Figure 1.7) were generated in a similar manner to the $H19^{hIC1}$ allele, and both alleles are currently being analyzed. Preliminary data suggest that maternal transmission of both alleles leads to biallelic *Igf2* expression, gain of

methylation at IC1, and overgrowth phenotype (personal communication with Dr. Andrea Riccio). It will be interesting to compare the phenotypes of mice inheriting the two microdeletion alleles. Of note, Beygo *et al*. reported that individuals with 2.2kb deletion exhibit less severe clinical phenotypes compared to those with 1.8kb deletion (Beygo et al., 2013).

Disease modeling of SRS

Despite IC1 hypomethylation being the most common epimutation found among SRS individuals (Figure 1.6) (Yamazawa et al., 2008), the molecular mechanism underlying the phenotype remains elusive. Obstacles in addressing this question include mosaicism of the epimutation in patients as well as lack of a suitable genetic model system. We suggest that the paternal transmission of hIC1 in a mouse can be used to study molecular mechanisms underlying SRS associated with IC1 hypomethylation. To this end, pursuing the rescue experiments with the $H19^{\Delta H19}$ and the $H19^{miR\text{-}675mut}$ alleles (Chapters 2.8.1 and 2.8.2) will elucidate the extent to which *H19* lncRNA and miR-675 contribute to the SRS-like phenotype. In addition, identifying tissue-specific (i.e. embryonic endodermal and mesodermal tissues and extraembryonic tissues) pathways altered by IC1 hypomethylation may shed light on whether the phenotypes underlying SRS are due to an altered physiology of one particular tissue or due to a combinatorial change in multiple tissues.

Investigating the species-specific regulation of the *H19/Igf2* locus

Evidence of incomplete histone reprogramming at hIC1 suggests that the mechanism regulating histone reprogramming at IC1 in the germline has diverged between mouse and human. In this regard, it would be interesting to determine if an IC1

ortholog of a species more closely related to mouse could recapitulate the wild-type epigenetic pattern upon paternal transmission. This approach will provide insights into the extent to which mechanisms regulating the ICR reprogramming in the germline are conserved across mammalian evolution. Of note, recent studies have identified different features of germline epigenetic reprogramming between mouse and human. Interestingly, DNA methylation erasure at ICRs starts earlier in development in human (before PGCs colonize the genital ridges) compared to mouse (upon PGCs colonization of the genital ridges) (Gkountela et al., 2015; Guo et al., 2015; Hackett et al., 2013; Tang et al., 2015). The precise timing of DNA methylation establishment in the human germ cells remains to be determined. Nonetheless, differences in the length of gestation or the timing of developmental cues might account for the incomplete reprogramming of hIC1 in mouse.

It is also possible that in the normal human context, the maternal hIC1 has a novel regulatory function (that is not present in mouse) of silencing the *IGF2* expression and enhancing *H19* expression. This human-specific function of the maternal hIC1 may be incompatible with the mouse system, acting dominantly on the mouse paternal allele. Such a neomorphic allele could recruit unknown transcription factors or form a specific three-dimensional chromatin conformation and/or an epigenetic landscape by recruiting chromatin modifying enzymes, leading to a preferential expression of *H19*, while silencing *Igf2* expression. This hypothesis could be tested by generating an allele where hIC1 is inserted next to the endogenous mIC1. Imprinted expression of *H19* and *Igf2* and DNA methylation and histone modification at the locus can be measured. If hIC1 has a dominant effect in abrogating the normal function of the mIC1 on the paternal allele, this could suggest a neomorphic function of hIC1 (or potentially a novel regulatory role of

endogenous hIC1), although the possibility of hIC1 acting as a dominant CTCF-dependent insulator compared to mIC1 cannot be excluded. If having an intact mIC1 at the endogenous locus preserves the normal imprinting function and male germline reprogramming of the hIC1 sequence, this will argue against the idea of hIC1 acquiring a neomorphic function. This result would rather suggest that the insertion of hIC1 can be influenced by the surrounding sequence or epigenetic landscape at the locus.

Male germ cell analyses

Given the well-described antagonistic relationship between the activating histone modification marks and DNA methylation (Chapter 1.1.2), we speculate that the abnormal enrichment of H3K4me2 at the hIC1 is inhibitory to the complete establishment of DNA methylation. However, it is equally possible that the hypomethylated state of DNA has attracted H3K4me2 at hIC1 by an unknown mechanism. More detailed time course analyses of DNA methylation and H3K4me2 enrichment in the PGCs and early stage male germ cells, such as spermatogonia, will provide insights into such an hypothesis.

Alternatively, there might exist an inherent difference between mIC1 and hIC1 in acquisition of methylation. A non-coding transcript is detected at mIC1 during methylation acquisition in the male germ cells (Henckel et al., 2012), suggesting a potential role of transcription in methylation establishment at mIC1. Whether the same holds true at the endogenous hIC1 remains to be determined. Nevertheless, it would be worth investigating whether the expression of the non-coding transcript is disrupted in the male germ cells upon replacement of the mIC1 with hIC1. This result will support the growing agreement that transcription plays an important role in DNA methylation establishment at the ICRs, at least in mouse.

4.2 Patient-derived human cell based model

Lineage-specific differentiation of the iPSCs

The iPSCs derived exhibit stable and expected DNA methylation status at the pUPD11-relevant ICRs—IC1 and IC2. We also verified that pUPD11 EBs express higher levels of *IGF2* compared to the non-pUPD11 EBs. To characterize pUPD11 in a disease-relevant context, we plan to differentiate select iPSC lines into hepatocytes. This work is ongoing in collaboration with the CHOP human ES/iPS cell core facility. The stability of methylation at IC1 and IC2 and the expression of *H19* and *Igf2* during different stages of differentiation will be carefully monitored. Ultimately, our goal is to perform RNA-sequencing in the cell lines to identify molecular pathways affected by pUPD11. Comparing gene expression profiles of different pUPD11 lines may shed light on the contribution of non-imprinted genes within the UPD region in the BWS disease etiology. Moreover, the non-pUPD11 iPSCs can be engineered to model other IC1 mutations (Figure 1.7). Establishment of these genetically-matched cell lines will facilitate deconstructing the genotype-phenotype relationship in BWS.

DLK1-DIO3 hypermethylation

The significance of hypermethylation of the *DLK1-DIO3* locus in iPSCs is unclear. Different parental cell sources, culture conditions, and passaging techniques used in the reprogramming experiments make it difficult to identify the source for this hypermethylation (Nazor et al., 2012). Several groups have investigated the mechanisms underlying the *DLK1-DIO3* hypermethylation, and found the involvement of post-translational histone modifying enzymes, DNA methyltransferases, long non-coding RNAs, and maternal factors (Kaneko et al., 2014; McDonald et al., 2016; Stadtfeld et al., 2010, 2012; Stelzer et al., 2014; Xu et al., 2015). Of note, individuals with pUPD14, in

which maternally expressed non-coding RNAs are repressed and paternally expressed protein-coding genes are upregulated, display postnatal growth and mental retardation and skeletal defects (Rocha et al., 2008). These suggest that the regulation at this locus is complex and its effect in human iPSC quality merits further investigation.

The effect of VC in *DLK1-DIO3* hypermethylation

In the IMR91 fibroblasts reprogramming experiment with and without VC, failure to maintain the *DLK1-DIO3* methylation might be attributed to the insufficient dosage or duration of VC treatment. It will be interesting to see whether further culturing the human iPSCs with VC could revert the *DLK1-DIO3* hypermethylation. Of note, culturing the mouse iPSCs with VC for 15 passages did not revert the *Dlk1-Dio3* hypermethylation (Stadtfeld et al., 2012), suggesting that VC is mainly effective in the early stage of mouse iPSC reprogramming at this locus. Nevertheless, dose-response and time-course experiments of the VC supplementation during human iPSC reprogramming/culture will elucidate the extent to which VC protects the human *DLK1-DIO3* locus from becoming hypermethylated.

4.3 Conclusions

Study of genomic imprinting is meaningful in understanding mammalian development and human health. In addition, the unique but conserved regulation of genomic imprinting can provide insights into mammalian evolution at both molecular and physiological level. Proper regulation of genomic imprinting requires correct epigenetic reprogramming in the germline as well as stable maintenance of the imprinted state in the somatic cells. Therefore, comprehensive knowledge on mechanisms of genomic imprinting requires studies in various cell types including embryonic, extraembryonic, and germ cell lineages, at various developmental stages. Similarly, it is likely that

mechanisms underlying alterations associated with human imprinting disorders are highly context-and stage-dependent. Because it is not always feasible to perform experiments in the desired cell types of the right developmental stage, especially with human samples, developing and taking advantage of various model systems is crucial in the study of genomic imprinting. The use of the humanized mouse model and the patient-specific iPSCs to interrogate mechanisms of imprinting, described in this dissertation, represents an example of such an endeavor. Continuous efforts in developing diverse models, by recognizing the limitations while maximizing the benefits of each model system, are instrumental to the field of imprinting.

CHAPTER 5.
MATERIALS AND METHODS

5.1 Generation of *H19^{hIC1}* mouse

Targeting vector

To generate the phIC1-neo target vector, first the backbone KpnI site was removed from the Δ3.8kb-5' target vector (Thorvaldsen et al., 2002), leaving a unique KpnI site between the 5' homology arm and the NeoR cassette. Into this KpnI site, we cloned the 4.8kb hIC1 sequence (from NsiI to EcoRI) isolated from human genome library that was engineered to contain KpnI sites (at the NsiI and XhoI sites) without destroying the endogenous sites (Stratagene) (Stadnick et al., 1999). The phIC1-neo target vector was designed to replace both the endogenous mouse IC1 and 1.3 kb G-rich repeat sequence with the hIC1 sequence, to make the distance between the targeted hIC1 and the *H19* promoter equivalent to what is observed at the orthologous human locus. We have previously shown that the G-rich repeat sequence is dispensable for normal *H19/Igf2* imprinting in mouse (Thorvaldsen et al., 2002).

ESC targeting, mouse breeding, and genotyping

phCI1-neo target vector was linearized and electroporated into E14 ESCs (Kühn et al., 1991) as described previously (Thorvaldsen et al., 2002). G418-resistant positive clones were isolated and correct targeting was validated by Southern blot analyses using the same external probes as described previously (Thorvaldsen et al., 2002) with following changes. gDNA was digested with EcoRV-MluI and hybridized to the 5'probe A. The internal probe C was isolated by PCR amplification of a WT B6 mouse gDNA using primers 5'-ATTCCTCTCCAACCCTAGCTCAG-3' and 5'-GGATCTGCCAAGGTGCTATTGC-3' and hybridized to gDNA digested with StuI (Figure 2.2A and B). Correctly targeted clones were injected into B6 blastocysts by the Transgenic and Chimeric Mouse Facility at the University of Pennsylvania. Obtained

chimeras were mated to B6 mice. Germline transmission of the targeted allele was confirmed within the agouti progeny by isolating gDNA from ear punch samples and performing Southern blot analysis as described above and PCR-based genotyping with primers PGNeo0.2 and HSEQR1 (Tables 5.1 and 5.2). All studies adhered to procedures approved by the Institutional Animal Care and Use Committee at the University of Pennsylvania.

Germline transmission of the *H19*$^{hIC1\text{-}neo}$ was verified by PCR-based genotyping as described above. To excise the neoR cassette (flanked by loxP sites), heterozygote female mice with *H19*$^{hIC1\text{-}neo}$ allele were crossed to B6 male mice that express *Cre* recombinase under the control of the adenovirus EIIa promoter (EIIA-Cre) (Jackson laboratories). NeoR excision was verified using Southern blot analysis and PCR-based genotyping with primers HIC1SEQF1 and TV23armSEQR1 (Figures 2.2A and B and Tables 5.1 and 5.2). Mice lacking the NeoR cassette (*H19*^{hIC1}) were maintained by crossing the *H19*$^{hIC1/+}$ female mice to wild-type B6 male mice and selecting for progeny carrying the *H19*^{hIC1} allele as determined by PCR analysis. For all comparisons, heterozygous knock-in offspring and embryos were compared with their wild-type littermates. Both males and females were included. For all genotypes, the maternal allele is listed first and the paternal allele second.

5.2 Generation of *H19*$^{\Delta H19}$ mouse

gRNA design

gRNA sequences were designed using the program (http://www.genome-engineering.org/crispr/?page) and are shown below. PAM sequences are underlined. 3A and 3B target 3'end, and 5A and 5B target 5'end of the *H19* gene.

	Pair A		Pair B
3A	CTTCAATATAATGCGACTCA TGG	3B	CAATATAATGCGACTCATGG GGG
5A	AACGTGCGCTGGAACGATAC AGG	5B	ATCAGTACATGGCCCCGCCG GGG

gRNA generation and injection

All procedures were done per guidance of Dr. Catherine May in the laboratory of Dr. Klaus Kaestner. The protocol provided by Dr. Catherine May was modified from Yang *et al*. (Yang et al., 2014). For sgRNA preparation, px335 plasmid (Addgene #42335) was PCR amplified using the primer sets:

Forward: 5'-TTAATACGACTCACTATAGGNNNNNNNNNNNNNNNNNNNgttttagagctagaaatagc-3'
Reverse: 5'-AGCACCGACTCGGTGCCACT-3'

The underlined 20 nucleotides of the forward primer were substituted with each gRNA sequence excluding the PAM sequence. Reverse primer is universal for all PCR reactions. PCR reaction was setup using the Phusion high-fidelity DNA polymerase (NEB, cat. No. M0530). To get enough materials for *in vitro* transcription, 2-3 PCR reactions were setup per gRNA.

Component	**Amount (µl/reaction)**
5X Phusion HF Buffer	20
10mM dNTPs	2
10uM Primer Mix	5
DNA Polymerase	1
Template DNA (pX335), 10 ng	2
H2O	70
Total Volume	100

Cycle number	**Denature**	**Anneal & Extend**	**Final Extend**
1	98 °C, 30s		
2-34	98 °C, 30s	72 °C, 20s	
35			72 °C, 1 min
Hold at 4 °C			

PCR products were ran on a 2% agarose gel. Once ~117bp products are verified, PCR products are gel-purified using the Qiagen Gel Extraction kit according to the

manufacturer's instruction. One column was used to pool the same PCR product and DNA was eluted in 15µl RNAse free water. *In vitro* transcription of gRNA was setup using the gel-purified product as templates. T7 High Yield RNA Synthesis kit (NEB, E2040S) was used according to the kit protocol. More than 2 tubes of reactions per gRNA were setup to increase the yield.

Component	**Amount (µl/reaction)**
10X Reaction Buffer	1.5
ATP	1.5
GTP	1.5
UTP	1.5
CTP	1.5
Template DNA (500 ng)	X
T7 RNA polymerase Mix	1.5
Nuclease-free H2O	X
Total	20

Reactions were incubated at 37°C overnight. Transcribed gRNA was purified using the MEGAclear kit (Life Technologies) according to the kit protocol. To prevent the injection needles from being clogged during microinjection, the eluted gRNA was spun twice at top speed at 4°C for 20min, with each spin followed by transfer of suspension to a new tube. The eluted gRNA was concentrated according to the protocol so that the final concentration is around 1-2µg/µl. RNA quality and quantity were checked using a bioanalyzer. Injection mix was prepared as follow:

Component	**Stock Concentration**	**Stock Vol. (ul)**	**Final Concentration**
sgRNA (Left)	500 ng/µl	3	50 ng/µl
sgRNA (Right)	500 ng/µl	3	50 ng/µl
Cas9 mRNA	1 µg/µl	3	100 ng/µl
Injection buffer*		21	
Total		30	

*Injection buffer: 10 mM Tris / 0.1 mM EDTA, pH 7.5 prepared with sterile water.

The injection mix was spun at top speed at 4°C for 20min, and the suspension was transferred to a new tube for injection. Either pair A or pair B was injected per zygote stage embryo by the Transgenic and Chimeric Mouse Facility at the University of Pennsylvania.

Mouse breeding and genotyping

Obtained chimeras and germ line transmission animals were PCR-genotyped for the *H19*$^{\triangle H19}$ allele using primers (Figure 2.14 and Tables 5.1 and 5.2). The *H19*$^{\triangle H19}$ allele is maintained/backcrossed in B6 background via paternal transmission.

5.3 Gene Expression Analysis

Sample collection and processing

All mouse tissue samples were flash-frozen in liquid nitrogen and stored at -80°C. Tissues were processed using the polytron homogenizer for the neonatal liver and tongue samples, or syringes and needles for the embryonic liver and placenta samples.

iPSCs were manually dislodged from plates using pipette tips or cell scrapers and EBs were dissociated using 0.25% Trypsin-EDTA. iPSCs were pelleted and stored at -80°C. The dissociated EB samples were pelleted, put in 1ml of TRIzol, incubated at room temperature for 10min, then stored at -80°C.

RNA isolation and cDNA synthesis

RNA from mouse tissues, iPSCs, and EBs was isolated using TRIzol according to the manufacturer's instructions. RNA was precipitated using glycogen and 100%

isopropanol. Isolated RNA was treated with DNase (Promega) to remove genomic DNA contamination and cDNA was synthesized using Superscript III reverse transcriptase (Invitrogen) and random primers (Roche).

Allele-specific expression

10ng of cDNA was used for allele-specific expression assay. Allele-specific expression of *H19* and *Igf2* was determined by RT-PCR followed by restriction digestion using RFLP between the B6 and CAST alleles. *H19* RT-PCR fragment was digested with Cac8I, and *Igf2* RT-PCR fragment was digested with MluCI for 3 hours at 37°C. Primers and PCR conditions are listed in Tables 5.2 and 5.3.

Total expression

5ng of cDNA was used for qRT-PCR assay. Power SYBR Green mater mix (Applied Biosystems) and primers in final concentration of 0.2μM were used on an ABI 7300 machine. Each sample was run in triplicate, and the mean value of triplicate is plotted in graphs. For each primer set, reaction efficiency (E) was calculated using standard curve, and E^-Ct value of each gene was normalized to E^-Ct values of housekeeping genes.

For analyses in mouse samples, total expression levels of *H19*, *Igf2, Igf1r*, and IGN genes were measured relative to the geometric mean of expression levels of *Arbp*, *Nono*, and *Rpl13a*. For the y-axis on the graph, the mean value of +/+ is arbitrarily set as 1. For analyses in human samples, total expression levels of pluripotency markers, EB markers, *H19*, and *IGF2* were measured relative to the geometric mean of expression levels of *GAPDH* and *PPIG*.

Total expression levels of miR-675-3p and miR-675-5p were determined relative to the level of snoRNA202 by using a separate RT kit (TaqMan MicroRNA Reverse

Transcription Kit, Thermo Fisher Scientific), qRT-PCR primers (Assay Id 001232, 001941, 001940, Thermo Fisher Scientific), and a PCR master mix (TaqMan Universal PCR Master Mix, catalog number 4304437, Thermo Fisher Scientific) according to manufacturer's protocol. Primers and PCR conditions for all expression analyses are listed in Tables 5.1, 5.2, and 5.7.

5.4 DNA Methylation Analysis

Sperm sample collection and preparation

H19$^{hIC1/+}$ mouse mature sperm was collected from cauda epididymis and vas deferens from minimum 8 weeks old, primed male mice. For the human sperm samples, discarded semen samples were obtained from the University of Pennsylvania Fertility Clinic following routine semen analysis. As all samples were discarded and de-identified, the University of Pennsylvania Institutional Review Board determined this study was exempt from requiring informed consent. Semen samples were washed with PBS to remove seminal fluid. The resulting human sperm were somatic cell lysed (0.1% SDS, 0.5% Triton-X-100) for 30min on ice, counted, and stored at -80°C until further use.

gDNA isolation

Collected mouse neonatal and embryonic tissues, human fibroblasts, iPSCs, and EBs were first digested with 12µl of 20mg/ml proteinase K (Sigma-Aldrich) in 500µl lysis buffer (50mM Tris, pH8.0, 100mM EDTA, 0.5% SDS) overnight at 55°C. For both mouse and human sperm, 500µl sperm-specific lysis buffer (20mM Tris-HCl pH8.0, 20mM EDTA, 4% SDS, 200mM NaCl) was used and 5µl of 2-mercaptoethanol (Sigma-Aldrich) was added, in addition to the 12µl of 20mg/ml proteinase K.

For all samples, gDNA was isolated using Phenol:Chloroform:Isoamyl Alcohol (Sigma-Aldrich P3803) and ethanol precipitation with 7.5M ammonium acetate. All isolated gDNA samples were resuspended in water and stored at-20°C or resuspended in 1xTE and stored at 4°C.

Bisulfite treatment

For mouse neonatal and embryonic tissues, mouse and human sperm samples, and iPSCs, 250-1000ng of gDNA was subjected to bisulfite mutagenesis using the Epitect kit (Qiagen) according to the manufacturer's protocol. Pools of 120-200 oocytes were collected from 25-28 days old heterozygote (*H19*$^{hIC1/+}$) female mice and pools of 40-50 two-cell embryos were collected by crossing *H19*$^{hIC1/+}$ male mice to superovulated WT B6 female mice. Blastocyst was individually collected (single blastocyst was used as a single data point). Oocytes, two-cell embryos, and blastocysts were subjected to bisulfite mutagenesis using the Epitect plus kit (Qiagen) according to manufacturer's protocol.

20-25ng bisulfite-mutagenized DNA (for mouse neonatal and embryonic tissues, mouse and human sperm samples, and iPSCs), 24-100 oocytes, ~18 two-cell embryos, or half blastocyst equivalent of bisulfite-mutagenized DNA was used per PCR for pyrosequencing, cloning and sequencing, and COBRA.

Pyrosequencing was performed as previously described (de Waal et al., 2014). PCR for cloning and sequencing for the mIC1 was performed using nested PCR and PCR beads as previously described (de Waal et al., 2014). PCR for cloning and sequencing for the hIC1 was performed using PyroMark PCR Kit (Qiagen). For all cloning and sequencing experiments, StrataClone, PCR cloning Kit (Agilent

Technologies) was used. For COBRA, the amplified PCR products were digested with appropriate restriction enzymes (HPYCH4IV for IC1, RsaI for IC2) for 3 hours at 37°C; enzymes were then inactivated for 10 min at 65°C; bands were resolved using 12% polyacrylamide gel and were quantified using ImageJ. For all PCR-based methylation analyses, minimum of two rounds of PCR was performed per analysis, when enough DNA was available. Primers, PCR conditions, and relevant restriction enzymes used for all methylation analyses are listed in Tables 5.1, 5.3, 5.5, and 5.6.

5.5 Histology

Histology was performed as previously described (de Waal et al., 2015).

5.6 Mouse Spermatogenic Cell Fractionation

Round spermatid fraction of mouse spermatogenic cells were collected using STA-PUT in two independent replicates and purity of each fraction was verified as described in (Bryant et al., 2013, 2015) and per guidance of Dr. Lacey Luense. Each collection used both testes of 12 heterozygous (*H19*$^{hIC1/+}$) primed male mice. Purity of each pool was measured as 87% (pool 1) and 86% (pool 2).

5.7 Isolation of mouse embryonic fibroblasts (MEFs)

MEFs were isolated from individual day 12.5 embryos in a B6 background as previously described (Verona et al., 2008).

5.8 Chromatin Immunoprecipitation (ChIP)-qRT-PCR Analysis

ChIP was carried out as previously described in (Bryant et al., 2015) and as per guidance of the protocol from the laboratory of Dr. Shelly Berger. Round spermatids and MEFs were cross-linked using 1% formaldehyde in Phosphate-buffered saline (PBS) for 10 min at room temperature. The reaction was quenched using glycine at final

concentration of 125mM for 5 min at room temperature. Cells were spun down at 1500rpm for 5min, washed with cold PBS(1X), and flash frozen in liquid nitrogen and stored at -80°C until processed for ChIP. After cell lysis, lysates were sonicated using Covaris S220 sonicator for 20 min with 5% duty cycle, 140 W of peak incident power, 200 cycles per burst, and 6°C bath temperature. 1/10 volume of 10% triton X-100 in PBS was added to the sonicated lysate, and the lysate was spun at 14000rpm for 10 min at 4°C. Supernatant was saved. Protein content of the lysate was measured by the bicinchoninic acid assay. For each IP, ~200µg of protein and 30µl of Dynabeads Protein G (Thermo Fisher Scientific), with 2.5 to 5µg of IgG (Santa Cruz Biotechnology sc-2027), H3 (Abcam ab1791), and H3K9me3 (Abcam ab8898), 5µl of H3K4me2 (EMD Millipore 07-030), or 10µl of CTCF (EMD Millipore 07-729) were used. Following elution of ChIP DNA, qRT-PCR was performed as described in Chapter 5.3 using the Power SYBR Green master mix and the ABI 7300 machine. For qRT-PCR, two different sets of primer pairs were used for assays *b* and *j* (Figure 2.2C) and a mean value of the two primer sets was plotted on the graph. All other assays used one set of primer pair. Each ChIP signal was calculated as percent input of each IP normalized to non-specific IgG (percent input IP - percent input IgG). ChIP-qRT-PCR primers are listed in Table 5.3.

5.9 Patient clinical features and genetic testing

Clinical information, clinical testing results, and fibroblast samples were collected from the Children's Hospital of Philadelphia BWS registry/repository (IRB #13-010658). All four patients presented with hyperinsulinism, macrosomia, macroglossia, omphalocele, and hemihyperplasia. Genome-wide single nucleotide polymorphism (SNP) microarray analysis was carried out using the Illumina CRC BeadChip as previously described (Conlin et al., 2010).

5.10 iPSC generation and culture

***** All reagents are from Life Technologies, unless otherwise specified first time mentioned.

Fibroblast derivation and culture

Skin samples were collected during surgical procedures and fibroblasts were dissociated using collagenase Type 2 (Worthington) in RPMI 1640 (1.6 g in 200 ml) for 30 minutes. In preparation for reprogramming, Patient 1, 2, 3 and 4 fibroblasts and normal human fetal male fibroblasts IMR-91 (Coriell Institute for Medical Research) were cultured in fibroblast media (RPMI with 20% fetal bovine serum (Hyclone SH30070.03), 1X penicillin/streptomycin, 1X GlutaMAX)) and fed every 2 days.

Viral Reprogramming

Patient 1 fibroblasts were reprogrammed with the infection of the inducible stem cell cassette (STEMCCA) and reverse tetracycline-controlled transactivator (rtTA) virus (Sommer et al., 2009) as previously described (Anguera et al., 2012; Woo et al., 2016). $5x10^4$ Patient 1 fibroblasts were seeded onto one well of a 6-well plate. The following day, in fibroblast media, cells were infected with STEMCCA (100µl) and rtTA (80µl) viruses prepared by (Woo et al., 2016). Two days after infection, the media was replaced with fresh fibroblast media. The following day, cells were passaged onto three 10 cm gelatinized (0.1% gelatin) plates in fibroblast media with 2µg/ml doxycycline (Sigma 9891) and transferred to low oxygen (5%CO_2, 4%O_2) incubator (a portion of infected cells were also plated onto 12-well plates -/+ 2µg/ml doxycycline (Sigma 9891) to test for efficiency of infection by measuring OCT4 induction by immunohistochemistry, by

method described below.) For subsequent days of reprogramming, cells were fed daily with WIBR hES media (DMEM/F12 with 15% fetal bovine serum, 5% Knockout™ Serum Replacement, 0.1875% Sodium Bicarbonate, 1X nonessential amino acids, 1X penicillin/streptomycin, 1X GlutaMAX, 0.1mM 2-mercaptoethanol, 10ng/ml βFGF (R&D Systems)) and freshly added 2μg/ml doxycycline, as described (Woo et al., 2016).

Episomal reprogramming

Patient 2, 3, and 4 fibroblasts and IMR91 fibroblasts (Coriell Institute for Medical Research Cell Repository) were reprogrammed with episomal plasmids as previously described (Bershteyn et al., 2014; Okita et al., 2011). To reprogram, we electroporated 600,000 cells with plasmids (1μg of each) CXLE-hOCT3/4-shp53, pCXLE-sSK, pCXLE-HUL, and pCXLE-EGFP plasmid (Okita et al., 2011) (Addgene) using the Neon® Transfection System 100-ml-kit according to manufacturer's instruction. Conditions for electroporation were 1,650 V, 10ms, and three pulses (Bershteyn et al., 2014). As described by (Okita et al., 2011), pCXLE-EGFP was used to monitor the efficiency of electroporation and gradual loss of plasmid/eGFP expression with prolonged culture. Cells were recovered in fibroblast media and plated onto 10 cm and 6 cm gelatinized plates and incubated in a standard high oxygen incubator. The following day, media was changed to the WIBR hES media, and plates were moved to a low oxygen incubator and fed daily for 6 days. During initial 7 days of reprogramming of the patient fibroblast 3 and 4 and IMR91 fibroblasts, the WIBR hES media was supplemented with 37.5μg/ml Vitamin C (VC) (Sigma 49752), based on analysis of (Chung et al., 2010) and considering the amount of VC already in the Knockout™ Serum Replacement (Stadtfeld

et al., 2012). On the 7th day after electroporation, fibroblasts were expanded onto multiple 6 cm and 10 cm gelatinized plates and fed daily with WIBR hES media, analogous to our viral reprogramming method (Woo et al., 2016).

Picking and culturing iPSCs

Colonies were picked between day 18 and 28 of reprogramming into media with 50% WIBR hES media and 50% serum free iPSC media (DMEMF12 with 20% Knockout™ Serum Replacement, 1X nonessential amino acids, 1X penicillin/streptomycin, 1X GlutaMAX, 0.1mM b-mercaptoethanol, 10ng/ml βFGF (R&D Systems)). Colonies were picked and passaged onto gelatin coated 6-well plates that were plated with 125,000 Mitomycin C treated CF1 mouse embryonic fibroblasts(MEFs)/well. Clones were weeded and fed every 1-2 days with serum free iPSC media. iPSCs were manually passaged every 5-7 days. On the days of picking, passaging wells with <5 colonies, and thawing iPSCs, 0.5mM ROCK inhibitor (StemMACS™Thiazovivin) was routinely added to media; ROCK inhibitor was removed the following day by changing to fresh media.

5.11 EB generation

***** All reagents are from Life Technologies, unless otherwise specified first time mentioned.

iPSCs were differentiated to EBs as previously described (Anguera et al., 2012). iPSCs were dislodged from MEF feeder cells using pipette tips or cell scrapers and transferred to low attachment plates (Corning) in 50% WIBR hES media and 50% EB differentiation media (DMEMF12 with 20% fetal bovine serum, 1X nonessential amino acids, 1X penicillin/streptomycin, 1X GlutaMAX, 0.1mM 2-mercaptoethanol). ROCK

inhibitor was added for the first day of EB differentiation at final concentration of 0.5mM and removed the next day by changing to fresh EB differentiation media. After 7 days, EBs were transferred to gelatin-coated plates and cultured for 7 days. Media was changed every other day. EBs were collected on day 14.

5.12 PCR Genotyping of fibroblasts and iPSC clones

Microsatellite marker AFM217YB10 was used to genotype parental alleles of patient 1 and 2 gDNA. Single Nucleotide Polymorphisms (SNP) rs3741216 (T/A) in patient 3 and rs10840159 (A/G) in patient 4 were used for genotyping iPSC clones, facilitated by restriction enzyme digest of polymorphisms. See Table 5.4 for details.

5.13 Characterization of iPSCs

Immunofluorescence staining

Cells were fixed in 4% paraformaldehyde (Electron Microscopy Sciences) for 20min at room temperature, permeabilized in 0.1% Triton-X100 (EMD), blocked with 3% bovine serum albumin (Calbiochem), and incubated overnight at 4°C in following primary antibodies: SSEA1 (1:100, Millipore), SSEA3 (1:100, Millipore), SSEA4 (1:100, Millipore), TRA1-60 (1:100, Millipore), TRA1-81 (1:100, Millipore) and Oct4 (1:250, Novus biologicals). Cells were then incubated with appropriate secondary antibodies: Alexa Fluor 488 goat anti-mouse IgG (1:1000, Life Technologies), Alexa Fluor goat anti-mouse IgM (1:1000, Life Technologies) and FITC-goat α-rabbit IgG (1:1000, Novus biologicals) for 30min at room temperature.

Karyotyping

Cells were treated with 0.2ug/ml Colcemid (Sigma) for 4 hours at 37°C, collected using 0.25% Trypsin and lysed in 0.56% (w/v) KCl for 25min at room temperature. Cells were fixed in methanol:acetic acid (3:1) solution, spread to slides, stained with Giemsa (Sigma).

Table 5.1 PCR conditions for the *H19^{hIC1}* allele

Gene/ region assayed	Tissue	Genotype	PCR conditions	Annealing Temp (°C) (T^A)	Cycle number (#)
Genotyping					
-	All	All	2min denaturation at 94°C; # cycles of 15sec at 94°C, 15sec at T^A, and 20sec at 72°C; 2min extension at 72°C	58-60	35
Allele-specific expression					
H19	P0 liver; P0 tongue; E15.5 liver; E15.5 placenta; E9.5 embryo	WT, KI*	2min denaturation at 95°C; # cycles of 15sec at 95°C, 10sec at T^A, and 20sec at 72°C; 5min extension at 72°C	60	26-30
Igf2	P0 liver; P0 tongue	WT, KI		58	27-29
	E15.5 liver; E15.5 placenta; E9.5 embryo	WT			26-28
	E15.5 placenta; E15.5 placenta E9.5 embryo	KI			31-33
Pyrosequencing					
hIC1 (CTS6)	All	All	15min denaturation at 95°C; # cycles of 30sec at 95°C, 30sec at T^A, and 30sec at 72°C; 5min extension at 72°C	55	45
All mouse ICRs except for *Snrpn* ICR			15min denaturation at 95°C; # cycles of 15sec at 95°C, 30sec at T^A, and 15sec at 72°C; 10min extension at 72°C	55	45
Mouse *Snrpn* ICR				58	
Bisulfite sequencing					
mIC1	All	All	1st round: 2min denaturation at 94°C; # cycles of 30sec at 94°C, 30sec at T^A, and 30sec at 72°C; 5min extension at 72°C	50	40
			2nd round: 2min denaturation at 94°C; # cycles of 30sec at 94°C, 30sec at T^A, and 30sec at 72°C; 5min extension at 72°C	58	35
hIC1 CTS1/2	All	All	15min denaturation at 95°C; # cycles of 30sec at 95°C, 30sec at T^A, and 30sec at 72°C; 5min extension at 72°C	58	45
hIC1 CTS3				60	41
hIC1 CTS4				58	41
hIC1 CTS6				55	45

*KI: hIC1 knock-in

Table 5.2 Genotyping and expression analyses primers for mouse studies

Gene/region Assayed	Primer name	Sequence	Reference
Genotyping			
PGNeo0.2		CCACTTGTGTAGCGCCAAGTGCC	Thorvaldsen et al., 2002
HSEQR1		CCACAGAGTCAGCATCCAC	
HIC1SEQF1		CCTTCACGGCTTTGACACTC	This study
TV23armSEQR1		GTCAACCGGAGGCACAGTAT	
H19-214		TTGTGGTGAGGCTGTCTTTG	
H19+2722		CCTATTCCCCATTCCATCCT	
Allele-specific expression			
H19	HE2	TGATGGAGAGGACAGAAGGG	De Waal et al., 2014
	HE4	TTGATTCAGAACGAGACGGAC	
Igf2	Igf2-18	ATCTGTGACCTCTTGAGCAGG	
	Igf2-20	GGGTTGTTTAGAGCCAATCAA	
Total expression			
Arbp	ArbpqPCRF	TCCCACTTACTGAAAAGGTCAAG	This study
	ArbpqPCRR	TCCGACTCTTCCTTTGCTTC	
Nono	NonoqPCRF	GCTCGTGAGAAGCTGGAGAT	Plasschaert and Bartolomei, 2014
	NonoqPCRR	TTCTTGACGTCTCATCAAATCC	
Rpl13a	Rpl13aqPCRF	ATCCCTCCACCCTATGACAA	
	Rpl13aqPCRR	GCCCCAGGTAAGCAAACTT	
H19	H19qPCRF	GTCTCGAAGAGCTCGGACTG	This study
	H19qPCRR	ACTGGCAGGCACATCCAC	
Igf2	Igf2qPCRF	CGCTTCAGTTTGTCTGTTCG	Weaver et al., 2010
	Igf2qPCRR	GCAGCACTCTTCCACGATG	
Cdkn1c	Cdkn1cqPCRF	TCTCGGGGATTCCAGGAC	This study
	Cdkn1cqPCRR	ACGTTTGGAGAGGGACACC	
Gtl2	Gtl2qPCRF	TTGCTGTTGTGCTCAGGTTC	This study
	Gtl2qPCRR	ATCCTGGGGTCCTCAGTCTT	
Igf2r	Igf2rqPCRF	GCACAGAATCCAGACTAGCATTACA	Varrault et al., 2006
	Igf2rqPCRR	CCTCCTTATCAGCTTTAAATATGTCTTTCTT	
Dlk1	Dlk1qPCRF	CGGGAAATTCTGCGAAATAG	This study
	Dlk1qPCRR	TGTGCAGGAGCATTCGTACT	
Gnas	Gnasexon1aqPCRF	AGCGCGAGGCCAACAAAA	Varrault et al., 2006
	Gnasexon1aqPCRR	GTGCGTGGCCCGGTAGA	
Peg3	Peg3qPCRF	GGTGTGTGCGTAGAGTGCTG	This study
	Peg3qPCRR	TCCTCTTGCCAGTTGTCTCC	
Slc38a4	Slc38a4qPCRF	TCACACTGCTGTTTCCAAGG	Bloise et al., 2012
	Slc38a4qPCRR	CAGCCGGAAGAATGAAAATC	
Igf1r	Igf1rqPCRF	GTGGGGGCTCGTGTTTCTC	Keniry et al., 2012
	Igf1rqPCRR	GATCACCGTGCAGTTTTCCA	

Table 5.3 Methylation anlyses and ChIP-qRT-PCR primers for the *H19^{hIC1}* allele

Region assayed	Primer name	Sequence	Reference
Pyrosequencing			
hIC1	hH19pyroseq2F	Qiagen Assay name ADS003 Catalog No PMC0007406	
	hH19pyroseq2R-biotinylated		
	hH19pyroseq2 seq		
For mouseIC1, Kcnq1ot1 ICR, Peg1 ICR, Peg3 ICR, Snrpn ICR, and IG-DMR, primers are described in (de Waal et al., 2014).			
Bisulfite sequencing			
mIC1	BMsp2t1	GAGTATTTAGGAGGTATAAGAATT	de Waal et al., 2014
	BHha1t3	ATCAAAAACTAACATAAACCCCT	
	BMsp2t2	GTAAGGAGATTATGTTTATTTTTGG	
	BHha1t4	CCTCATTAATCCCATAACTAT	
hIC1 CTS1/2	CTS1F	GTATTTTTGGAGGTTTTTTATTTAG	Beygo et al., 2013
	CTS2R	TCCCATAAATATTCTATCCCTCACTA	
hIC1 CTS3	CTS3F	GGGAGATGAGATATTTTGGTGATAATG	
	CTS3R	CCCCATCCAAAAAAAACTTAAAC	
hIC1 CTS4	CTS4F	TATAGGGTTTTTGGTAGGTTTA	
	CTS4R	CCATAAATATCCTATCCCTAATA	
hIC1 CTS6	CTS6F	GTAGGGTTTTTGGTAGGTATAGAGT	Takai et al., 2001
	CTS6R	CACTAAAAAAAACAATTATCAATTC	
hIC1 CTS6 (used for oocytes)	hH19pyroseq2F	Qiagen Assay name ADS003 Catalog No PMC0007406 Non-biotinylated reverse primer was used	
	hH19pyroseq2R non-biotin		
ChIP-qRT-PCR			
mIC1	mIC1chIPF2-assay *b*	AATGCCTGATCCCTTTGTTG	This study
	mIC1chIPR2-assay *b*	TACATATTGCTCGGCAGACG	
	mIC1chIPF3-assay *b*	AGCTTTGAGTACCCCAGGTTCA	Delaval et al., 2007
	mIC1chIPR3-assay *b*	GCCTCTGCTTTTATGGCTATGG	
	mIC1chIPF4-assay *c*	CTCTTTAGGTTTGGCGCAAT	This study
	mIC1chIPR4-assay *c*	GCCCTATTCTTGGACGTCTG	
hIC1	hIC1chIPF1-assay *j*	CTGATTCCAGCAGCACAGAG	This study
	hIC1chIPR1-assay *j*	GTGTGAGCCTGACAGTGCAT	
	hIC1chIPF2-assay *j*	GGTCCCAGTCATGATCACCT	
	hIC1chIPR2-assay *j*	CTGAAGCTGGGACAGGAGAG	
	hIC1chIPF4-assay *i*	CCCGAGGGTTGTCAGAGATA	
	hIC1chIPR4-assay *i*	CTCCCCAACCTTCAACAATG	
	hIC1chIPF5-assay *k*	ACAGAATCGGTTGTGGCTGT	
	hIC1chIPR5-assay *k*	AGCCTTGGGTCACCTTCAG	

Table 5.4 Genotyping assays for iPSCs

Patient cell lines[a]	Forward	Reverse	Restriction Enzyme	Polymorphism Assayed
Patient 1	GGGGCATCTGTGGCTA	TCCGGTTTGGTTCAGG	Not applicable	AFM217YB10
Patient 2	GGGGCATCTGTGGCTA	TCCGGTTTGGTTCAGG	Not applicable	AFM217YB10
Patient 3	AACACCTTAGGCTGGTGG	TCGGAGCTTCCAGACTAG	MseI[b]	rs3741216 This study
Patient 4	AACACCTTAGGCTGGTGG	TCGGAGCTTCCAGACTAG	MscI[b]	rs10840159

[a] PCR conditions to assay Patients 1 and 2 microsatellite repeat marker: 94°C 2min, (94°C 30s, 57°C 30s, 72°C 30s)x35 cycles, 72°C 5min. To assay Patients 3 and 4 SNPs, PCR conditions are: 94°C 4min, (94°C 90s, 60°C 60s, 72°C 90s)x31 cycles.
[b]The common (maternal) allele of patient 3 gDNA is digested with MseI at rs3741216 (T/A); the common (maternal) allele of patient 9 gDNA is digested with MscI at rs10840159 (A/G).

Table 5.5 PCR conditions for methylation analyses of iPSCs

Gene/ region assayed	Restriction enzyme	PCR conditions	Annealing Temp (°C) (T^A)	Cycle number (#)
Pyrosequencing				
hIC1 (CTS6) and *SNRPN* ICR	Not applicable	15min denaturation at 95°C; # cycles of 30sec at 95°C, 30sec at T^A, and 30sec at 72°C; 5min extension at 72°C	55	45
IG-DMR and MEG3-DMR			58	45
Bisulfite sequencing				
hIC1 CTS3	Not applicable	15min denaturation at 95°C; # cycles of 30sec at 95°C, 30sec at T^A, and 30sec at 72°C; 5min extension at 72°C	60	41
COBRA				
IC1 (CTS3)	HPYCH4IV	15min denaturation at 95°C; # cycles of 30sec at 95°C, 30sec at T^A, and 30sec at 72°C; 5min extension at 72°C	60	41
IC2	RsaI			

Table 5.6 Methylation analyses primers for iPSCs

Region assayed	Primer name	Sequence	Reference
Pyrosequencing			
hIC1	hH19pyroseq2F	Qiagen Assay name ADS003 Catalog No PMC0007406	
	hH19pyroseq2R-biotinylated		
	hH19pyroseq2 seq		
IG-DMR Assay1	CG4Assay1F	5'Biotin- ATTATTGAATTGGGTTTGTTAGTAGT	Kameswaran et al., 2014
	CG4Assay1R	ATCAAAACAACTCAAATCCTTTATAAC	
	CG4Assay1seq	CCTTTATAACAAATTAAAATATATC	
IG-DMR Assay2	CG4Assay2F	GTTTTATTATTGAATTGGGTTTGTTAGTA	
	CG4Assay2R	5'Biotin- ATCAAAACAACTCAAATCCTTTATAAC	
	CG4Assay2seq	AATTGGGTTTGTTAGTAG	
MEG3-DMR Assay1	CG7Assay1F	5'Biotin- ATTATAGGGTGTTGGTTATGG	
	CG7Assay1R	CCCCAAATTCTATAACAAATTACTCT	
	CG7Assay1seq	CAACAAAAAAAAAAAAAAAAAATTC	
MEG3-DMR Assay2	CG7Assay2F	5'Biotin- TTAGATTGTAGTAAAGAAGGGAGGAAAAAA	
	CG7Assay2R	CCCCCACACATTATACCTAAATTC	
	CG7Assay2seq	ATTATACCTAAATTCACCCT	
SNRPN ICR	SNRPN F	5'Biotin- AGGGAGTTGGGATTTTTGTATT	White et al., 2006
	SNRPN R	CCCCAAACTATCTCTTAAAAAAAAC	
	SNRPN seq1	ACACAACTAACCTTACCC	
	SNRPN seq2	CCAACCTACCTCTAC	
Bisulfite sequencing			
hIC1 CTS3	CTS3F	GGGAGATGAGATATTTTGGTGATAATG	Beygo et al., 2013
	CTS3R	CCCCATCCAAAAAAAACTTAAAC	
COBRA			
IC1 (CTS3)	CTS3F	GGGAGATGAGATATTTTGGTGATAATG	Beygo et al., 2013
	CTS3R	CCCCATCCAAAAAAAACTTAAAC	
IC2	IC2F	GGTAGGATTTTGTTGAGGAGTTTT	This study
	IC2R	CACACCCAACCAATACCTCATA	

Table 5.7 qRT-PCR primers for iPSCs and EBs

Gene	Forward	Reverse	Reference
Differentiation markers for embryonic body			
AFP	AGCTTGGTGGTGGATGAAAC	CCCTCTTCAGCAAAGCAGAC	Teo et al., 2011
GATA4	TCCCTCTTCCCTCCTCAAAT	TCAGCGTGTAAAGGCATCTG	Park et al., 2008
HAND1	TGCCTGAGAAAGAGAACCAG	ATGGCAGGATGAACAAACAC	This study, designed using Pubmed primer blast
RUNX2	CACTCACTACCACACCTACC	GTCGCCAAACAGATTCATCC	Cai et al., 2006
NCAM1	ATGGAAACTCTATTAAAGTGAACCTG	TAGACCTCATACTCAGCATTCCAGT	Park et al., 2008
FGF5	CGCTATGTCTTCCTCTTCTGC	CAAAACACTTAACATATTGGCTTCG	Higgins et al., 2014
Pluripotency markers			
OCT4	CGACCATCTGCCGCTTTG	GCCGCAGCTTACACATGTTCT	Anokye-Danso et al., 2011
SOX2	ACAGCAAATGACAGCTGCAAA	TCGGCATCGCGGTTTTT	
NANOG	CCAAAGGCAAACAACCCACTT	CGGGACCTTGTCTTCCTTTTT	
DNMT3B	GGAAATTAGAATCAAGGAAATACGA	AATTTGTCTTGAGGCGCTTG	This study, designed using Roche Universal ProbeLibrary program
GDF3	CGCTTTCTCCCAGACCAA	GGCAGACAGGTTAAAGTAGAGGAG	
TERT	GCCTTCAAGAGCCACGTC	CCACGAACTGTCGCATGT	
LIN28A	AAGCGCAGATCAAAAGGAGA	CTGATGCTCTGGCAGAAGTG	
H19, IGF2, GAPDH, and PPIG			
H19	GCAAGAAGCGGGTCTGTTT	GCTGGGTAGCACCATTTCTT	Hiura et al., 2013
IGF2	ACACCCTCCAGTTCGTCTGT	GAAACAGCACTCCTCAACGA	
GAPDH	GTCGTGGAGTCCACTGGCGTC	TCATGAGTCCTTCCACGATAC	
PPIG	GAAGAGTGCGATCAAGAACCCATGAC	GTCTCTCCTCCTTCTCCTCCTATCTTT	Cheng et al., 2012

BIBLIOGRAPHY

Abramowitz, L.K., and Bartolomei, M.S. (2012). Genomic imprinting: Recognition and marking of imprinted loci. Curr. Opin. Genet. Dev. *22*, 72–78.

Al Adhami, H., Evano, B., Le Digarcher, A., Gueydan, C., Dubois, E., Parrinello, H., Dantec, C., Bouschet, T., Varrault, A., and Journot, L. (2015). A systems-level approach to parental genomic imprinting: The imprinted gene network includes extracellular matrix genes and regulates cell cycle exit and differentiation. Genome Res. *25*, 353–367.

Andrews, S.C., Wood, M.D., Tunster, S.J., Barton, S.C., Surani, M.A., and John, R.M. (2007). Cdkn1c (p57Kip2) is the major regulator of embryonic growth within its imprinted domain on mouse distal chromosome 7. BMC Dev. Biol. *7*, 53.

Angiolini, E., Coan, P.M., Sandovici, I., Iwajomo, O.H., Peck, G., Burton, G.J., Sibley, C.P., Reik, W., Fowden, A.L., and Constância, M. (2011). Developmental adaptations to increased fetal nutrient demand in mouse genetic models of Igf2-mediated overgrowth. FASEB J. *25*, 1737–1745.

Anguera, M.C., Sadreyev, R., Zhang, Z., Szanto, A., Payer, B., Sheridan, S.D., Kwok, S., Haggarty, S.J., Sur, M., Alvarez, J., et al. (2012). Molecular signatures of human induced pluripotent stem cells highlight sex differences and cancer genes. Cell Stem Cell *11*, 75–90.

Anokye-Danso, F., Trivedi, C.M., Juhr, D., Gupta, M., Cui, Z., Tian, Y., Zhang, Y., Yang, W., Gruber, P.J., Epstein, J.A., et al. (2011). Highly efficient miRNA-mediated reprogramming of mouse and human somatic cells to pluripotency. Cell Stem Cell *8*, 376–388.

Azzi, S., Blaise, A., Steunou, V., Harbison, M.D., Salem, J., Brioude, F., Rossignol, S., Habib, W.A., Thibaud, N., Neves, C. Das, et al. (2014). Complex Tissue-Specific Epigenotypes in Russell-Silver Syndrome Associated with 11p15 ICR1 Hypomethylation. Hum. Mutat. *35*, 1211–1220.

Baker, J., Liu, J.P., Robertson, E.J., and Efstratiadis, a. (1993). Role of insulin-like growth factors in embryonic and postnatal growth. Cell *75*, 73–82.

Barlow, D.P. (1993). Methylation and Imprinting: From Host Defense to Gene Regulation?. Science. *260*, 309–310.

Bartholdi, D., Krajewska-Walasek, M., Ounap, K., Gaspar, H., Chrzanowska, K.H., Ilyana, H., Kayserili, H., Lurie, I.W., Schinzel, A., and Baumer, A. (2009). Epigenetic mutations of the imprinted IGF2-H19 domain in Silver-Russell syndrome (SRS): results from a large cohort of patients with SRS and SRS-like phenotypes. J.Med.Genet. *46*, 192–197.

Bartolomei, M.S., and Ferguson-Smith, A.C. (2011). Mammalian genomic imprinting. Cold Spring Harb. Perspect. Biol. *3*, 1–17.

Bartolomei, M.S., Zemel, S., and Tilghman, S.M. (1991). Parental imprinting of the mouse H19 gene. Nature *351*, 153–155.

Bell, A.C., and Felsenfeld, G. (2000). Methylation of a CTCF-dependent boundary controls imprinted expression of the Igf2 gene. Nature *405*, 482–485.

Benetatos, L., Vartholomatos, G., and Hatzimichael, E. (2014). DLK1-DIO3 imprinted cluster in induced pluripotency: landscape in the mist. Cell. Mol. Life Sci. *71*, 4421–4430.

Bergman, D., Halje, M., Nordin, M., and Engström, W. (2013). Insulin-like growth factor 2 in development and disease: A mini-review. Gerontology *59*, 240–249.

Bershteyn, M., Hayashi, Y., Desachy, G., Hsiao, E.C., Sami, S., Tsang, K.M., Weiss, L.A., Kriegstein, A.R., Yamanaka, S., and Wynshaw-Boris, A. (2014). Cell-autonomous correction of ring chromosomes in human induced pluripotent stem cells. Nature *507*, 99–103.

Beygo, J., Citro, V., Sparago, A., De crescenzo, A., Cerrato, F., Heitmann, M., Rademacher, K., Guala, A., Enklaar, T., Anichini, C., et al. (2013). The molecular function and clinical phenotype of partial deletions of the IGF2/H19 imprinting control region depends on the spatial arrangement of the remaining CTCF-binding sites. Hum. Mol. Genet. *22*, 544–557.

Bhattacharya, B., Cai, J., Luo, Y., Miura, T., Mejido, J., Brimble, S.N., Zeng, X., Schulz, T.C., Rao, M.S., and Puri, R.K. (2005). Comparison of the gene expression profile of undifferentiated human embryonic stem cell lines and differentiating embryoid bodies. BMC Dev. Biol. *5*, 22.

Bian, C., and Yu, X. (2014). PGC7 suppresses TET3 for protecting DNA methylation. Nucleic Acids Res. *42*, 2893–2905.

Blaschke, K., Ebata, K.T., Karimi, M.M., Zepeda-Martínez, J. a, Goyal, P., Mahapatra, S., Tam, A., Laird, D.J., Hirst, M., Rao, A., et al. (2013). Vitamin C induces Tet-dependent DNA demethylation and a blastocyst-like state in ES cells. Nature *500*, 222–226.

Bloise, E., Lin, W., Liu, X., Simbulan, R., Kolahi, K.S., Petraglia, F., Maltepe, E., Donjacour, A., and Rinaudo, P. (2012). Impaired placental nutrient transport in mice generated by in vitro fertilization. Endocrinology *153*, 3457–3467.

Bourc'his, D., and Bestor, T.H. (2004). Meiotic catastrophe and retrotransposon reactivation in male germ cells lacking Dnmt3L. Nature *431*, 96–99.

Bourc'his, D., Xu, G.L., Lin, C.S., Bollman, B., and Bestor, T.H. (2001). Dnmt3L and the establishment of maternal genomic imprints. Science (80-.). *294*, 2536–2539.

Brunkow, M.E., and Tilghman, S.M. (1991). Ectopic expression of the H19 gene in mice causes prenatal lethality. Genes Dev. *5*, 1092–1101.

Bryant, J.M., Meyer-Ficca, M.L., Dang, V.M., Berger, S.L., and Meyer, R.G. (2013). Separation of spermatogenic cell types using STA-PUT velocity sedimentation. J. Vis. Exp. (80):e50648.

Bryant, J.M., Donahue, G., Wang, X., Meyer-Ficca, M., Luense, L.J., Weller, A.H., Bartolomei, M.S., Blobel, G.A., Meyer, R.G., Garcia, B.A., et al. (2015). Characterization of BRD4 during Mammalian Postmeiotic Sperm Development. Mol. Cell. Biol. *35*, 1433–1448.

Cai, J., Chen, J., Liu, Y., Miura, T., Luo, Y., Loring, J.F., Freed, W.J., Rao, M.S., and Zeng, X. (2006). Assessing self-renewal and differentiation in human embryonic stem cell lines. Stem Cells *24*, 516–530.

Cassidy, S.B., Schwartz, S., Miller, J.L., and Driscoll, D.J. (2012). Prader-Willi syndrome. Genet. Med. *14*, 10–26.

Chamberlain, S.J., Chen, P., Ng, K.Y., Bourgois-rocha, F., Lemtiri-chlieh, F., Levine, E.S., and Lalande, M. (2010). Induced pluripotent stem cell models of the genomic imprinting disorders Angelman and Prader – Willi syndromes. Pnas *107*, 17668–17673.

Chang, G., Gao, S., Hou, X., Xu, Z., Liu, Y., Kang, L., Tao, Y., Liu, W., Huang, B., Kou, X., et al. (2014). High-throughput sequencing reveals the disruption of methylation of imprinted gene in induced pluripotent stem cells. Cell Res. *24*, 293–306.

Chen, J., Guo, L., Zhang, L., Wu, H., Yang, J., Liu, H., Wang, X., Hu, X., Gu, T., Zhou, Z., et al. (2013). Vitamin C modulates TET1 function during somatic cell reprogramming. Nat. Genet. *45*, 1504–1509.

Cheng, X., Ying, L., Lu, L., Galvão, A.M., Mills, J.A., Lin, H.C., Kotton, D.N., Shen, S.S., Nostro, M.C., Choi, J.K., et al. (2012). Self-renewing endodermal progenitor lines generated from human pluripotent stem cells. Cell Stem Cell *10*, 371–384.

Chotalia, M., Smallwood, S.A., Ruf, N., Dawson, C., Lucifero, D., Frontera, M., James, K., Dean, W., and Kelsey, G. (2009). Transcription is required for establishment of germline methylation marks at imprinted genes. Genes Dev. *23*, 105–117.

Choufani, S., Shuman, C., and Weksberg, R. (2013). Molecular findings in beckwith-wiedemann syndrome. Am. J. Med. Genet. Part C Semin. Med. Genet. *163*, 131–140.

Christodoulou, C., Longmire, T.A., Shen, S.S., Bourdon, A., Sommer, C.A., Gadue, P., Spira, A., Gouon-Evans, V., Murphy, G.J., Mostoslavsky, G., et al. (2011). Mouse ES and iPS cells can form similar definitive endoderm despite differences in imprinted genes. J. Clin. Invest. *121*, 2313–2325.

Chung, T.-L., Brena, R.M., Kolle, G., Grimmond, S.M., Berman, B.P., Laird, P.W., Pera, M.F., and Wolvetang, E.J. (2010). Vitamin C promotes widespread yet specific DNA demethylation of the epigenome in human embryonic stem cells. Stem Cells *28*, 1848–1855.

Ciccone, D.N., Su, H., Hevi, S., Gay, F., Lei, H., Bajko, J., Xu, G., Li, E., and Chen, T. (2009). KDM1B is a histone H3K4 demethylase required to establish maternal genomic imprints. Nature *461*, 415–418.

Coan, P.M., Fowden, A.L., Constancia, M., Ferguson-Smith, A.C., Burton, G.J., and Sibley, C.P. (2008). Disproportional effects of Igf2 knockout on placental morphology and diffusional exchange characteristics in the mouse. J Physiol *586*, 5023–5032.

Conlin, L.K., Thiel, B.D., Bonnemann, C.G., Medne, L., Ernst, L.M., Zackai, E.H., Deardorff, M.A., Krantz, I.D., Hakonarson, H., and Spinner, N.B. (2010). Mechanisms of mosaicism, chimerism and uniparental disomy identified by single nucleotide polymorphism array analysis. Hum. Mol. Genet. *19*, 1263–1275.

Constância, M., Hemberger, M., Hughes, J., Dean, W., Ferguson-Smith, A., Fundele, R., Stewart, F., Kelsey, G., Fowden, A., Sibley, C., et al. (2002). Placental-specific IGF-II is a major modulator of placental and fetal growth. Nature *417*, 945–948.

Cruvinel, E., Budinetz, T., Germain, N., Chamberlain, S., Lalande, M., and Martins-Taylor, K. (2014). Reactivation of maternal SNORD116 cluster via SETDB1 knockdown in Prader-Willi syndrome iPSCs. Hum. Mol. Genet. *23*, 4674–4685.

Davis, T.L., Trasler, J.M., Moss, S.B., Yang, G.J., and Bartolomei, M.S. (1999). Acquisition of the H19 methylation imprint occurs differentially on the parental alleles during spermatogenesis. Genomics *58*, 18–28.

Dawlaty, M.M., Breiling, A., Le, T., Raddatz, G., Barrasa, M.I., Cheng, A.W., Gao, Q., Powell, B.E., Li, Z., Xu, M., et al. (2013). Combined Deficiency of Tet1 and Tet2 Causes Epigenetic Abnormalities but Is Compatible with Postnatal Development. Dev. Cell *24*, 310–323.

DeChiara, T.M., Efstratiadis, A., and J., R.E. (1990). A growth-deficiency phenotype in heterozygous mice carrying an insulin-like growth factor II gene disrupted by targeting. Nature *345*, 78–80.

DeChiara, T.M., Robertson, E.J., and Efstratiadis, A. (1991). Parental imprinting of the mouse insulin-like growth factor II gene. Cell *64*, 849–859.

Delaval, K., Govin, J., Cerqueira, F., Rousseaux, S., Khochbin, S., and Feil, R. (2007). Differential histone modifications mark mouse imprinting control regions during spermatogenesis. EMBO J. *26*, 720–729.

Demars, J., Shmela, M.E., Rossignol, S., Okabe, J., Netchine, I., Azzi, S., Cabrol, S., le Caignec, C., David, A., le Bouc, Y., et al. (2010). Analysis of the IGF2/H19 imprinting control region uncovers new genetic defects, including mutations of OCT-binding sequences, in patients with 11p15 fetal growth disorders. Hum. Mol. Genet. *19*, 803–814.

Diaz-Meyer, N., Day, C.D., Khatod, K., Maher, E.R., Cooper, W., Reik, W., Junien, C., Graham, G., Algar, E., Der Kaloustian, V.M., et al. (2003). Silencing of CDKN1C (p57KIP2) is associated with hypomethylation at KvDMR1 in Beckwith-Wiedemann syndrome. J Med Genet *40*, 797–801.

Eid, W., and Abdel-Rehim, W. (2016). Vitamin C promotes pluripotency of human induced pluripotent stem cells via the histone demethylase JARID1A. Biol. Chem. *397*, 1205–1213.

Engel, N., West, A.G., Felsenfeld, G., and Bartolomei, M.S. (2004). Antagonism between DNA hypermethylation and enhancer-blocking activity at the H19 DMD is uncovered by CpG mutations. Nat. Genet. *36*, 883–888.

Engel, N., Thorvaldsen, J.L., and Bartolomei, M.S. (2006). CTCF binding sites promote transcription initiation and prevent DNA methylation on the maternal allele at the imprinted H19/Igf2 locus. Hum. Mol. Genet. *15*, 2945–2954.

Engel, N., Raval, A.K., Thorvaldsen, J.L., and Bartolomei, S.M. (2008). Three-dimensional conformation at the H19/Igf2 locus supports a model of enhancer tracking. Hum. Mol. Genet. *17*, 3021–3029.

Engström, W., Shokrai, a, Otte, K., Granérus, M., Gessbo, a, Bierke, P., Madej, a, Sjölund, M., and Ward, a (1998). Transcriptional regulation and biological significance of the insulin like growth factor II gene. Cell Prolif. *31*, 173–189.

Esteban, M.A., Wang, T., Qin, B., Yang, J., Qin, D., Cai, J., Li, W., Weng, Z., Chen, J., Ni, S., et al. (2010). Vitamin C Enhances the Generation of Mouse and Human Induced Pluripotent Stem Cells. Cell Stem Cell *6*, 71–79.

Frank, D., Fortino, W., Clark, L., Musalo, R., Wang, W., Saxena, A., Li, C.-M., Reik, W., Ludwig, T., and Tycko, B. (2002). Placental overgrowth in mice lacking the imprinted gene Ipl. Proc. Natl. Acad. Sci. U. S. A. *99*, 7490–7495.

Frost, J.M., and Moore, G.E. (2010). The importance of imprinting in the human placenta. PLoS Genet. *6*, 1–9.

Gabory, A., Ripoche, M.-A., Le Digarcher, A., Watrin, F., Ziyyat, A., Forné, T., Jammes, H., Ainscough, J.F.X., Surani, M.A., Journot, L., et al. (2009). H19 acts as a trans regulator of the imprinted gene network controlling growth in mice. Development *136*, 3413–3421.

Gao, Y., Han, Z., Li, Q., Wu, Y., Shi, X., Ai, Z., Du, J., Li, W., Guo, Z., and Zhang, Y. (2015). Vitamin C induces a pluripotent state in mouse embryonic stem cells by modulating microRNA expression. FEBS J. *282*, 685–699.

Gicquel, C., Rossignol, S., Cabrol, S., Houang, M., Steunou, V., Barbu, V., Danton, F., Thibaud, N., Le Merrer, M., Burglen, L., et al. (2005). Epimutation of the telomeric imprinting center region on chromosome 11p15 in Silver-Russell syndrome. Nat. Genet. *37*, 1003–1007.

Gkountela, S., Zhang, K.X., Shafiq, T.A., Liao, W.W., Hargan-Calvopiña, J., Chen, P.Y., and Clark, A.T. (2015). DNA demethylation dynamics in the human prenatal germline. Cell *161*, 1425–1436.

Guastafierro, T., Cecchinelli, B., Zampieri, M., Reale, A., Riggio, G., Sthandier, O., Zupi, G., Calabrese, L., and Caiafa, P. (2008). CCCTC-binding factor activates PARP-1 affecting DNA methylation machinery. J. Biol. Chem. *283*, 21873–21880.

Guo, F., Yan, L., Guo, H., Li, L., Hu, B., Zhao, Y., Yong, J., Hu, Y., Wang, X., Wei, Y., et al. (2015). The transcriptome and DNA methylome landscapes of human primordial germ cells. Cell *161*, 1437–1452.

Habib, W.A., Azzi, S., Brioude, F., Steunou, V., Thibaud, N., Das Neves, C., Le Jule, M., Chantot-Bastaraud, S., Keren, B., Lyonnet, S., et al. (2014). Extensive investigation of the IGF2/H19 imprinting control region reveals novel OCT4/SOX2 binding site defects associated withspecific methylation patterns in Beckwith-Wiedemann syndrome. Hum. Mol. Genet. *23*, 5763–5773.

Hackett, J.A., Sengupta, R., Zylicz, J.J., Murakami, K., Lee, C., Down, T.A., and Surani, M.A. (2013). Germline DNA Demethylation Dynamics and Imprint Erasure Through 5-Hydroxymethylcytosine. Science (80-.). *339*, 448–452.

Hajkova, P., Ancelin, K., Waldmann, T., Lacoste, N., Lange, U.C., Cesari, F., Lee, C., Almouzni, G., Schneider, R., and Surani, M.A. (2008). Chromatin dynamics during epigenetic reprogramming in the mouse germ line. Nature *452*, 877–881.

Hatada, I., and Mukai, T. (1995). Genomic imprinting of p57KIP2, a cyclin-dependent kinase inhibitor, in mouse. Nat. Genet. *11*, 204–206.

Hatada, I., Ohashi, H., Fukushima, Y., Kaneko, Y., Inoue, M., Komoto, Y., Okada, A., Ohishi, S., Nabetani, A., Morisaki, H., et al. (1996). An imprinted gene p57KIP2 is mutated in Beckwith-Wiedemann syndrome. Nat. Genet. *14*, 171–173.

Heckmann, D., Urban, C., Weber, K., Kannenberg, K., and Binder, G. (2015). Decreased expression of cell proliferation-related genes in clonally derived skin fibroblasts from children with Silver-Russell syndrome is independent of the degree of 11p15 ICR1 hypomethylation. Clin. Epigenetics *7*, 5.

Henckel, A., Chebli, K., Kota, S.K., Arnaud, P., and Feil, R. (2012). Transcription and histone methylation changes correlate with imprint acquisition in male germ cells. EMBO J. *31*, 606–615.

Higashimoto, K., Urano, T., Sugiura, K., Yatsuki, H., Joh, K., Zhao, W., Iwakawa, M., Ohashi, H., Oshimura, M., Niikawa, N., et al. (2003). Loss of CpG methylation is strongly correlated with loss of histone H3 lysine 9 methylation at DMR-LIT1 in patients with Beckwith-Wiedemann syndrome. Am. J. Hum. Genet. *73*, 948–956.

Higgins, C.A., Petukhova, L., Harel, S., Ho, Y.Y., Drill, E., Shapiro, L., Wajid, M., and Christiano, A.M. (2014). FGF5 is a crucial regulator of hair length in humans. Proc. Natl. Acad. Sci. *111*, 10648–10653.

Hiura, H., Toyoda, M., Okae, H., Sakurai, M., Miyauchi, N., Sato, A., Kiyokawa, N., Okita, H., Miyagawa, Y., Akutsu, H., et al. (2013). Stability of genomic imprinting in human induced pluripotent stem cells. BMC Genet *14*, 32.

Holwerda, S.J.B., and de Laat, W. (2013). CTCF: the protein, the binding partners, the binding sites and their chromatin loops. Philos. Trans. R. Soc. Lond. B. Biol. Sci. *368*, 20120369.

Hori, N., Nakano, H., Takeuchi, T., Kato, H., Hamaguchi, S., Oshimura, M., and Sato, K. (2002). A dyad Oct-binding sequence functions as a maintenance sequence for the unmethylated state within the H19/Igf2-imprinted control region. J. Biol. Chem. *277*, 27960–27967.

Hur, S.K., Freschi, A., Ideraabdullah, F., Thorvaldsen, J.L., Luense, L.J., Weller, A.H., Berger, S.L., Cerrato, F., Riccio, A., and Bartolomei, M.S. (2016). Humanized H19/Igf2 locus reveals diverged imprinting mechanism between mouse and human and reflects Silver-Russell syndrome phenotypes. Proc. Natl. Acad. Sci. U. S. A. *113*, 10938–10943.

Ideraabdullah, F.Y., Vigneau, S., and Bartolomei, M.S. (2008). Genomic imprinting mechanisms in mammals. Mutat. Res. - Fundam. Mol. Mech. Mutagen. *647*, 77–85.

Ideraabdullah, F.Y., Abramowitz, L.K., Thorvaldsen, J.L., Krapp, C., Wen, S.C., Engel, N., and Bartolomei, M.S. (2011). Novel cis-regulatory function in ICR-mediated imprinted repression of H19. Dev. Biol. *355*, 349–357.

Ideraabdullah, F.Y., Thorvaldsen, J.L., Myers, J.A., and Bartolomei, M.S. (2014). Tissue-specific insulator function at H19/Igf2 revealed by deletions at the imprinting control region. Hum. Mol. Genet. *23*, 6246–6259.

Ishida, M. (2016). New developments in Silver – Russell syndrome and implications for clinical practice. *8*, 563–580.

Ishihara, K., Hatano, N., Furuumi, H., Kato, R., Iwaki, T., Miura, K., Jinno, Y., and Sasaki, H. (2000). Comparative genomic sequencing identifies novel tissue-specific enhancers and sequence elements for methylation-sensitive factors implicated in Igf2/H19 imprinting. Genome Res. *10*, 664–671.

Isles, A.R. (2009). Evolution of genomic imprinting in humans: does bipedalism have a role? Trends Genet. *25*, 495–500.

Jinno, Y., Sengoku, K., Nakao, M., Tamate, K., Miyamoto, T., Matsuzaka, T., Sutcliffe, J.S., Anan, T., Takuma, N., Nishiwaki, K., et al. (1996). Mouse/human sequence divergence in a region with a paternal-specific methylation imprint at the human H19 locus. Hum. Mol. Genet. *5*, 1155–1161.

Jones, B.K., Levorse, J., and Tilghman, S.M. (2002). A human H19 transgene exhibits impaired paternal-specific imprint acquisition and maintenance in mice. Hum. Mol. Genet. *11*, 411–418.

Kaffer, C.R., Grinberg, A., and Pfeifer, K. (2001). Regulatory Mechanisms at the Mouse Igf2/H19 Locus. Mol. Cell. Biol. *21*, 8189–8196.

Kalish, J.M., Conlin, L.K., Mostoufi-Moab, S., Wilkens, A.B., Mulchandani, S., Zelley, K., Kowalski, M., Bhatti, T.R., Russo, P., Mattei, P., et al. (2013). Bilateral Pheochromocytomas, Hemihyperplasia, and Subtle Somatic Mosaicism: The Importance of Detecting Low-Level Uniparental Disomy. Am. J. Med. Genet. Part A *161*, 993–1001.

Kalish, J.M., Jiang, C., and Bartolomei, M.S. (2014). Epigenetics and imprinting in human disease. Int. J. Dev. Biol. *58*, 291–298.

Kameswaran, V., Bramswig, N.C., McKenna, L.B., Penn, M., Schug, J., Hand, N.J., Chen, Y., Choi, I., Vourekas, A., Won, K.J., et al. (2014). Epigenetic regulation of the DLK1-MEG3 MicroRNA cluster in human type 2 diabetic islets. Cell Metab. *19*, 135–145.

Kanduri, C. (2011). Kcnq1ot1: A chromatin regulatory RNA. Semin. Cell Dev. Biol. *22*, 343–350.

Kaneda, M., Okano, M., Hata, K., Sado, T., Tsujimoto, N., Li, E., and Sasaki, H. (2004). Essential role for de novo DNA methyltransferase Dnmt3a in paternal and maternal imprinting. Nature *429*, 900–903.

Kaneko, S., Bonasio, R., Saldaña-Meyer, R., Yoshida, T., Son, J., Nishino, K., Umezawa, A., and Reinberg, D. (2014). Interactions between JARID2 and Noncoding RNAs Regulate PRC2 Recruitment to Chromatin. Mol. Cell *53*, 290–300.

Kannenberg, K., Weber, K., Binder, C., Urban, C., Kirschner, H.-J., and Binder, G. (2012). IGF2/H19 hypomethylation is tissue, cell, and CpG site dependent and not correlated with body asymmetry in adolescents with Silver-Russell syndrome. Clin. Epigenetics *4*, 15.

Kato, Y., Kaneda, M., Hata, K., Kumaki, K., Hisano, M., Kohara, Y., Okano, M., Li, E., Nozaki, M., and Sasaki, H. (2007). Role of the Dnmt3 family in de novo methylation of imprinted and repetitive sequences during male germ cell development in the mouse. Hum. Mol. Genet. *16*, 2272–2280.

Keniry, A., Oxley, D., Monnier, P., Kyba, M., Dandolo, L., Smits, G., and Reik, W. (2012). The H19 lincRNA is a developmental reservoir of miR-675 that suppresses growth and Igf1r. Nat. Cell Biol. *14*, 659–665.

Kühn, R., Rajewsky, K., and Müller, W. (1991). Generation and analysis of interleukin-4 deficient mice. Science *254*, 707–710.

Latos, P.A., Pauler, F.M., Koerner, M. V., Senergin, H.B., Hudson, Q.J., Stocsits, R.R., Allhoff, W., Stricker, S.H., Klement, R.M., Warcsok, Katarzyna, E., et al. (2012). Airn Transcriptional Overlab, But Not Its lncRNA Products, Induces Imprinted Igf2r Silencing. Science. *338*, 1469–1472.

Leach, N.T., Chudoba, I., Stewart, T. V., Holmes, L.B., and Weremowicz, S. (2007). Maternally Inherited Duplication of Chromosome 7, dup(7)(p11.2p12), Associated With Mild Cognitive Deficit Without Features of Silver-Russell Syndrome. Am. J. Med. Genet. A *143A*, 1489–1493.

Lee, J.T., and Bartolomei, M.S. (2013). X-inactivation, imprinting, and long noncoding RNAs in health and disease. Cell *152*, 1308–1323.

Lee, D.H., Singh, P., Tsai, S.Y., Oates, N., Spalla, A., Spalla, C., Brown, L., Rivas, G., Larson, G., Rauch, T.A., et al. (2010). CTCF-dependent chromatin bias constitutes transient epigenetic memory of the mother at the H19-igf2 imprinting control region in prospermatogonia. PLoS Genet. *6*:e1001224.

Lee, J.E., Pintar, J., and Efstratiadis, A. (1990). Pattern of the insulin-like growth factor II gene expression during early mouse embryogenesis. Development *110*, 151–159.

Leighton, P.A., Saam, J.R., Ingram, R.S., Stewart, C.L., and Tilghman, S.M. (1995a). An enhancer deletion affects both H19 and Igf2 expression. Genes Dev. *9*, 2079–2089.

Leighton, P. a, Ingram, R.S., Eggenschwiler, J., Efstratiadis, a, and Tilghman, S.M. (1995b). Disruption of imprinting caused by deletion of the H19 gene region in mice. Nature *375*, 34–39.

Lewis, A., Mitsuya, K., Umlauf, D., Smith, P., Dean, W., Walter, J., Higgins, M., Feil, R., and Reik, W. (2004). Imprinting on distal chromosome 7 in the placenta involves repressive histone methylation independent of DNA methylation. Nat. Genet. *36*, 1291–1295.

Li, E., Beard, C., and Jaenisch, R. (1993). Role for DNA methylation in genomic imprinting. Nature *366*, 362–365.

Li, X., Ito, M., Zhou, F., Youngson, N., Zuo, X., Leder, P., and Ferguson-Smith, A.C. (2008). A Maternal-Zygotic Effect Gene, Zfp57, Maintains Both Maternal and Paternal Imprints. Dev. Cell *15*, 547–557.

Lin, S., Ferguson-Smith, A.C., Schultz, R.M., and Bartolomei, M.S. (2011). Nonallelic transcriptional roles of CTCF and cohesins at imprinted loci. Mol. Cell. Biol. *31*, 3094–3104.

Liu, L., Luo, G.Z., Yang, W., Zhao, X., Zheng, Q., Lv, Z., Li, W., Wu, H.J., Wang, L., Wang, X.J., et al. (2010). Activation of the imprinted Dlk1-Dio3 region correlates with pluripotency levels of mouse stem cells. J. Biol. Chem. *285*, 19483–19490.

Lucifero, D., Mann, M.R.W., Bartolomei, M.S., and Trasler, J.M. (2004). Gene-specific timing and epigenetic memory in oocyte imprinting. Hum. Mol. Genet. *13*, 839–849.

Mackay, D.J., Callaway, J.L., Marks, S.M., White, H.E., Acerini, C.L., Boonen, S.E., Dayanikli, P., Firth, H. V, Goodship, J.A., Haemers, A.P., et al. (2008). Hypomethylation of multiple imprinted loci in individuals with transient neonatal diabetes is associated with mutations in ZFP57. Nat Genet *40*, 949–951.

Mann, M.R.W. (2003). Disruption of Imprinted Gene Methylation and Expression in Cloned Preimplantation Stage Mouse Embryos. Biol. Reprod. *69*, 902–914.

Mapendano, C.K., Kishino, T., Miyazaki, K., Kondo, S., Yoshiura, K.I., Hishikawa, Y., Koji, T., Niikawa, N., and Ohta, T. (2006). Expression of the Snurf-Snrpn IC transcript in the oocyte and its putative role in the imprinting establishment of the mouse 7C imprinting domain. J. Hum. Genet. *51*, 236–243.

McDonald, C.M., Liu, L., Xiao, L., Schaniel, C., and Li, X. (2016). Genomic imprinting defect in Zfp57 mutant iPS cell lines. Stem Cell Res. *16*, 259–263.

McDonald, J.F., Matzke, M.A., and Matzke, A.J. (2005). Host defenses to transposable elements and the evolution of genomic imprinting. Cytogenet. Genome Res. *110*, 242–249.

McGrath, J., and Solter, D. (1984). Completion of mouse embryogenesis requires both the maternal and paternal genomes. Cell *37*, 179–183.

Meissner, A., Mikkelsen, T.S., Gu, H., Wernig, M., Hanna, J., Sivachenko, A., Zhang, X., Bernstein, B.E., Nusbaum, C., Jaffe, D.B., et al. (2008). Genome-scale DNA methylation maps of pluripotent and differentiated cells. Nature *454*, 766–770.

Milligan, L., Antoine, E., Bisbal, C., Weber, M., Brunel, C., Forné, T., and Cathala, G. (2000). H19 gene expression is up-regulated exclusively by stabilization of the RNA during muscle cell differentiation. Oncogene *19*, 5810–5816.

Mo, C.-F., Wu, F.-C., Tai, K.-Y., Chang, W.-C., Chang, K.-W., Kuo, H.-C., Ho, H.-N., Chen, H.-F., and Lin, S.-P. (2015). Loss of non-coding RNA expression from the DLK1-DIO3 imprinted locus correlates with reduced neural differentiation potential in human embryonic stem cell lines. Stem Cell Res. Ther. *6*, 1. doi:10.1186/scrt535.

Mohammad, F., Mondal, T., Guseva, N., Pandey, G.K., and Kanduri, C. (2010). Kcnq1ot1 noncoding RNA mediates transcriptional gene silencing by interacting with Dnmt1. Development *137*, 2493–2499.

Monnier, P., Martinet, C., Pontis, J., Stancheva, I., Ait-Si-Ali, S., and Dandolo, L. (2013). H19 lncRNA controls gene expression of the Imprinted Gene Network by recruiting MBD1. Proc. Natl. Acad. Sci. U. S. A. *110*, 20693–20698.

Moore, G.E., Ishida, M., Demetriou, C., Al-Olabi, L., Leon, L.J., Thomas, A.C., Abu-Amero, S., Frost, J.M., Stafford, J.L., Chaoqun, Y., et al. (2015). The role and interaction of imprinted genes in human fetal growth. Philos. Trans. R. Soc. Lond. B. Biol. Sci. *370*, 20140074.

Mussa, A., Russo, S., De Crescenzo, A., Freschi, A., Calzari, L., Maitz, S., Macchiaiolo, M., Molinatto, C., Baldassarre, G., Mariani, M., et al. (2016). (Epi)genotype–phenotype correlations in Beckwith–Wiedemann syndrome. Eur. J. Hum. Genet. *24*, 183–190.

Nakamura, T., Liu, Y.-J., Nakashima, H., Umehara, H., Inoue, K., Matoba, S., Tachibana, M., Ogura, A., Shinkai, Y., and Nakano, T. (2012). PGC7 binds histone H3K9me2 to protect against conversion of 5mC to 5hmC in early embryos. Nature *486*, 415–419.

Nativio, R., Sparago, A., Ito, Y., Weksberg, R., Riccio, A., and Murrell, A. (2011). Disruption of genomic neighbourhood at the imprinted IGF2-H19 locus in Beckwith-Wiedemann syndrome and Silver-Russell syndrome. Hum. Mol. Genet. *20*, 1363–1374.

Nazor, K.L., Altun, G., Lynch, C., Tran, H., Harness, J. V., Slavin, I., Garitaonandia, I., Müller, F.J., Wang, Y.C., Boscolo, F.S., et al. (2012). Recurrent variations in DNA methylation in human pluripotent stem cells and their differentiated derivatives. Cell Stem Cell *10*, 620–634.

Nishino, K., Toyoda, M., Yamazaki-Inoue, M., Fukawatase, Y., Chikazawa, E., Sakaguchi, H., Akutsu, H., and Umezawa, A. (2011). DNA methylation dynamics in human induced pluripotent stem cells over time. PLoS Genet. *7*.

Okita, K., Matsumura, Y., Sato, Y., Okada, A., Morizane, A., Okamoto, S., Hong, H., Nakagawa, M., Tanabe, K., Tezuka, K., et al. (2011). A more efficient method to generate integration-free human iPS cells. Nat. Methods *8*, 409–412.

Ooi, S.K.T., Qiu, C., Bernstein, E., Li, K., Jia, D., Yang, Z., Erdjument-Bromage, H., Tempst, P., Lin, S.-P., Allis, C.D., et al. (2007). DNMT3L connects unmethylated lysine 4 of histone H3 to de novo methylation of DNA. Nature *448*, 714–717.

Pandey, R.R., Mondal, T., Mohammad, F., Enroth, S., Redrup, L., Komorowski, J., Nagano, T., Mancini-DiNardo, D., and Kanduri, C. (2008). Kcnq1ot1 Antisense Noncoding RNA Mediates Lineage-Specific Transcriptional Silencing through Chromatin-Level Regulation. Mol. Cell *32*, 232–246.

Park, I.-H., Zhao, R., West, J.A., Yabuuchi, A., Huo, H., Ince, T.A., Lerou, P.H., Lensch, M.W., and Daley, G.Q. (2008). Reprogramming of human somatic cells to pluripotency with defined factors. Nature *451*, 141–146.

Patten, M.M., Ross, L., Curley, J.P., Queller, D.C., Bonduriansky, R., and Wolf, J.B. (2014). The evolution of genomic imprinting: theories, predictions and empirical tests. Heredity (Edinb). *113*, 119–128.

Patten, M.M., Cowley, M., Oakey, R.J., and Feil, R. (2016). Regulatory links between imprinted genes: evolutionary predictions and consequences. Proc. R. Soc. B Biol. Sci. *283*, doi:10.1098/rspn.2015.2760.

Peters, J. (2014). The role of genomic imprinting in biology and disease: an expanding view. Nat. Rev. Genet. *15*, 517–530.

Plasschaert, R.N., and Bartolomei, M.S. (2014). Genomic imprinting in development, growth, behavior and stem cells. Development *141*, 1805–1813.

Poirier, F., Chan, C.-T.J., Timmons, P.M., Robertson, E.J., Evans, M.J., and Rigby, P.W.J. (1991). The murine H19 gene is activated during embryonic stem cell differentiation in vitro and at the time of implantation in the developing embryo. Development *113*, 1105–1114.

Poole, R.L., Leith, D.J., Docherty, L.E., Shmela, M.E., Gicquel, C., Splitt, M., Temple, I.K., and Mackay, D.J.G. (2012). Beckwith-Wiedemann syndrome caused by maternally inherited mutation of an OCT-binding motif in the IGF2/H19-imprinting control region, ICR1. Eur. J. Hum. Genet. *20*, 240–243.

Prawitt, D., Enklaar, T., Gärtner-Rupprecht, B., Spangenberg, C., Oswald, M., Lausch, E., Schmidtke, P., Reutzel, D., Fees, S., Lucito, R., et al. (2005). Microdeletion of target sites for insulator protein CTCF in a chromosome 11p15 imprinting center in Beckwith-Wiedemann syndrome and Wilms' tumor. Proc. Natl. Acad. Sci. U. S. A. *102*, 4085–4090.

Reik, W., Constância, M., Fowden, A., Anderson, N., Dean, W., Ferguson-Smith, A., Tycko, B., and Sibley, C. (2003). Regulation of supply and demand for maternal nutrients in mammals by imprinted genes. J. Physiol. *547*, 35–44.

Renfree, M.B., Suzuki, S., and Kaneko-Ishino, T. (2013). The origin and evolution of genomic imprinting and viviparity in mammals. Philos. Trans. R. Soc. Lond. B. Biol. Sci. *368*, doi:10.1098/rstb.2012.0151.

Ripoche, M.A., Kress, C., Poirier, F., and Dandolo, L. (1997). Deletion of the H19 transcription unit reveals the existence of a putative imprinting control element. Genes Dev. *11*, 1596–1604.

Riso, V., Cammisa, M., Kukreja, H., Anvar, Z., Verde, G., Sparago, A., Acurzio, B., Lad, S., Lonardo, E., Sankar, A., et al. (2016). ZFP57 maintains the parent-of-origin-specific expression of the imprinted genes and differentially affects non-imprinted targets in mouse embryonic stem cells. Nucleic Acids Res. *44*, 8165–8178.

Rocha, S.T. da, Edwards, C.A., Ito, M., Ogata, T., and Ferguson-Smith, A.C. (2008). Genomic imprinting at the mammalian Dlk1-Dio3 domain. Trends Genet. *24*, 306–316.

Romanelli, V., Belinchón, A., Benito-Sanz, S., Martínez-Glez, V., Gracia-Bouthelier, R., Heath, K.E., Campos-Barros, A., García-Miñaur, S., Fernandez, L., Meneses, H., et al. (2010). CDKN1C (p57Kip2) analysis in beckwith-wiedemann syndrome (BWS) patients: Genotype-phenotype correlations, novel mutations, and polymorphisms. Am. J. Med. Genet. Part A *152*, 1390–1397.

Rose, N.R., and Klose, R.J. (2014). Understanding the relationship between DNA methylation and histone lysine methylation. Biochim. Biophys. Acta - Gene Regul. Mech. *1839*, 1362–1372.

Schmidt, J. V, Levorse, J.M., and Tilghman, S.M. (1999). Enhancer competition between H19 and Igf2 does not mediate their imprinting. Proc. Natl. Acad. Sci. U. S. A. *96*, 9733–9738.

Scott, C.D., and Weiss, J. (2000). Soluble insulin-like growth factor II/mannose 6-phosphate receptor inhibits DNA synthesis in insulin-like growth factor II sensitive cells. J. Cell. Physiol. *182*, 62–68.

Shi, Y., Zhao, Y., and Deng, H. (2010). Powering Reprogramming with Vitamin C. Cell Stem Cell *6*, 1–2.

Shmela, M.E., and Gicquel, C.F. (2013). Human diseases versus mouse models: insights into the regulation of genomic imprinting at the human 11p15/mouse distal chromosome 7 region. J. Med. Genet. *50*, 11–20.

Singh, P., Li, A.X., Tran, D.A., Oates, N., Kang, E.R., Wu, X., and Szabó, P.E. (2013). De Novo DNA Methylation in the Male Germ Line Occurs by Default but Is Excluded at Sites of H3K4 Methylation. Cell Rep. *4*, 205–219.

Smits, G., Mungall, A.J., Griffiths-Jones, S., Smith, P., Beury, D., Matthews, L., Rogers, J., Pask, A.J., Shaw, G., VandeBerg, J.L., et al. (2008). Conservation of the H19 noncoding RNA and H19-IGF2 imprinting mechanism in therians. Nat. Genet. *40*, 971–976.

Soejima, H., and Higashimoto, K. (2013). Epigenetic and genetic alterations of the imprinting disorder Beckwith-Wiedemann syndrome and related disorders. J Hum Genet *58*, 402–409.

Sommer, C.A., Stadtfeld, M., Murphy, G.J., Hochedlinger, K., Kotton, D.N., and Mostoslavsky, G. (2009). Induced pluripotent stem cell generation using a single lentiviral stem cell cassette. Stem Cells *27*, 543–549.

Sparago, A., Cerrato, F., Vernucci, M., Ferrero, G.B., Silengo, M.C., and Riccio, A. (2004). Microdeletions in the human H19 DMR result in loss of IGF2 imprinting and Beckwith-Wiedemann syndrome. Nat. Genet. *36*, 958–960.

Stadnick, M.P., Pieracci, F.M., Cranston, M.J., Taksel, E., Thorvaldsen, J.L., and Bartolomei, M.S. (1999). Role of a 461-bp G-rich repetitive element in H19 transgene imprinting. Dev. Genes Evol. *209*, 239–248.

Stadtfeld, M., Apostolou, E., Akutsu, H., Fukuda, A., Follett, P., Natesan, S., Kono, T., Shioda, T., and Hochedlinger, K. (2010). Aberrant silencing of imprinted genes on chromosome 12qF1 in mouse induced pluripotent stem cells. Nature *465*, 175–181.

Stadtfeld, M., Apostolou, E., Ferrari, F., Choi, J., Walsh, R.M., Chen, T., Oi, S., Kim, S.Y., Bestor, T., Shioda, T., et al. (2012). Ascorbic acid prevents loss of Dlk1-Dio3 imprinting and facilitates generation of all-iPS cell mice from terminally differentiated B cells. Nat. Genet. *44*, 398–405.

Stelzer, Y., Sagi, I., Yanuka, O., Eiges, R., and Benvenisty, N. (2014). The noncoding RNA IPW regulates the imprinted DLK1-DIO3 locus in an induced pluripotent stem cell model of Prader-Willi syndrome. Nat. Genet. *46*, 551–557.

Stewart, K.R., Veselovska, L., Kim, J., Huang, J., Saadeh, H., Tomizawa, S.I., Smallwood, S.A., Chen, T., and Kelsey, G. (2015). Dynamic changes in histone modifications precede de novo DNA methylation in oocytes. Genes Dev. *29*, 2449–2462.

Sun, B., Ito, M., Mendjan, S., Ito, Y., Brons, I.G.M., Murrell, A., Vallier, L., Ferguson-Smith, A.C., and Pedersen, R.A. (2012). Status of genomic imprinting in epigenetically distinct pluripotent stem cells. Stem Cells *30*, 161–168.

Suzuki, S., Shaw, G., Kaneko-Ishino, T., Ishino, F., and Renfree, M.B. (2011). The evolution of mammalian genomic imprinting was accompanied by the acquisition of novel CpG islands. Genome Biol. Evol. *3*, 1276–1283.

Takahashi, K., and Yamanaka, S. (2006). Induction of Pluripotent Stem Cells from Mouse Embryonic and Adult Fibroblast Cultures by Defined Factors. Cell *126*, 663–676.

Takai, D., Gonzales, F. a, Tsai, Y.C., Thayer, M.J., and Jones, P. a (2001). Large scale mapping of methylcytosines in CTCF-binding sites in the human H19 promoter and aberrant hypomethylation in human bladder cancer. Hum. Mol. Genet. *10*, 2619–2626.

Takikawa, S., Ray, C., Wang, X., Shamis, Y., Wu, T.Y., and Li, X. (2013). Genomic imprinting is variably lost during reprogramming of mouse iPS cells. Stem Cell Res. *11*, 861–873.

Tang, W.W.C., Dietmann, S., Irie, N., Leitch, H.G., Floros, V.I., Bradshaw, C.R., Hackett, J.A., Chinnery, P.F., and Surani, M.A. (2015). A unique gene regulatory network resets the human germline epigenome for development. Cell *161*, 1453–1467.

Teo, A.K.K., Arnold, S.J., Trotter, M.W.B., Brown, S., Ang, L.T., Chng, Z., Robertson, E.J., Dunn, N.R., and Vallier, L. (2011). Pluripotency factors regulate definitive endoderm specification through eomesodermin. Genes Dev. *25*, 238–250.

Terranova, R., Yokobayashi, S., Stadler, M.B., Otte, A.P., van Lohuizen, M., Orkin, S.H., and Peters, A.H.F.M. (2008). Polycomb Group Proteins Ezh2 and Rnf2 Direct Genomic Contraction and Imprinted Repression in Early Mouse Embryos. Dev. Cell *15*, 668–679.

Thorvaldsen, J.L., Duran, K.L., and Bartolomei, M.S. (1998). Deletion of the H19 differentially methylated domain results in loss of imprinted expression of H19 and Igf2. Genes Dev. *12*, 3693–3702.

Thorvaldsen, J.L., Mann, M.R.W., Nwoko, O., Duran, K.L., and Bartolomei, M.S. (2002). Analysis of sequence upstream of the endogenous H19 gene reveals elements both essential and dispensable for imprinting. Mol. Cell. Biol. *22*, 2450–2462.

Tremblay, K.D., Duran, K.L., and Bartolomei, M.S. (1997). A 5' 2-kilobase-pair region of the imprinted mouse H19 gene exhibits exclusive paternal methylation throughout development. Mol. Cell. Biol. *17*, 4322–4329.

Tunster, S.J., Van de Pette, M., and John, R.M. (2011). Fetal overgrowth in the Cdkn1c mouse model of Beckwith-Wiedemann syndrome. Dis. Model. Mech. *4*, 814–821.

Umlauf, D., Goto, Y., Cao, R., Cerqueira, F., Wagschal, A., Zhang, Y., and Feil, R. (2004). Imprinting along the Kcnq1 domain on mouse chromosome 7 involves repressive histone methylation and recruitment of Polycomb group complexes. Nat. Genet. *36*, 1296–1300.

Unternaehrer, J.J., and Daley, G.Q. (2011). Induced pluripotent stem cells for modelling human diseases. Philos Trans R Soc L. B Biol Sci *366*, 2274–2285.

Varrault, A., Gueydan, C., Delalbre, A., Bellmann, A., Houssami, S., Aknin, C., Severac, D., Chotard, L., Kahli, M., Le Digarcher, A., et al. (2006). Zac1 Regulates an Imprinted Gene Network Critically Involved in the Control of Embryonic Growth. Dev. Cell *11*, 711–722.

Verona, R.I., Thorvaldsen, J.L., Reese, K.J., and Bartolomei, M.S. (2008). The transcriptional status but not the imprinting control region determines allele-specific histone modifications at the imprinted H19 locus. Mol. Cell. Biol. *28*, 71–82.

de Waal, E., Mak, W., Calhoun, S., Stein, P., Ord, T., Krapp, C., Coutifaris, C., Schultz, R.M., and Bartolomei, M.S. (2014). In Vitro Culture Increases the Frequency of Stochastic Epigenetic Errors at Imprinted Genes in Placental Tissues from Mouse Concepti Produced Through Assisted Reproductive Technologies. Biol. Reprod. *90*, 22–22.

de Waal, E., Vrooman, L.A., Fischer, E., Ord, T., Mainigi, M.A., Coutifaris, C., Schultz, R.M., and Bartolomei, M.S. (2015). The cumulative effect of assisted reproduction procedures on placental development and epigenetic perturbations in a mouse model. Hum. Mol. Genet. *24*, 6975–6985.

Wagschal, A., Sutherland, H.G., Woodfine, K., Henckel, A., Chebli, K., Schulz, R., Oakey, R.J., Bickmore, W.A., and Feil, R. (2008). G9a histone methyltransferase contributes to imprinting in the mouse placenta. Mol. Cell. Biol. *28*, 1104–1113.

Wang, T., Chen, K., Zeng, X., Yang, J., Wu, Y., Shi, X., Qin, B., Zeng, L., Esteban, M.A., Pan, G., et al. (2011). The histone demethylases Jhdm1a/1b enhance somatic cell reprogramming in a vitamin-C-dependent manner. Cell Stem Cell *9*, 575–587.

Weaver, J.R., Susiarjo, M., and Bartolomei, M.S. (2009). Imprinting and epigenetic changes in the early embryo. Mamm. Genome *20*, 532–543.

Weksberg, R., Shuman, C., and Beckwith, J.B. (2010). Beckwith–Wiedemann syndrome. Eur. J. Hum. Genet. *18*, 8–14.

White, H.E., Durston, V.J., Harvey, J.F., and Cross, N.C.P. (2006). Quantitative analysis of SRNPN gene methylation by pyrosequencing as a diagnostic test for Prader-Willi syndrome and Angelman syndrome. Clin. Chem. *52*, 1005–1013.

Woo, D.H., Chen, Q., Yang, T.L.B., Glineburg, M.R., Hoge, C., Leu, N.A., Johnson, F.B., and Lengner, C.J. (2016). Enhancing a Wnt-Telomere Feedback Loop Restores Intestinal Stem Cell Function in a Human Organotypic Model of Dyskeratosis Congenita. Cell Stem Cell *19*, 397–405.

Xu, X., Smorag, L., Nakamura, T., Kimura, T., Dressel, R., Fitzner, A., Tan, X., Linke, M., Zechner, U., Engel, W., et al. (2015). Dppa3 expression is critical for generation of fully reprogrammed iPS cells and maintenance of Dlk1-Dio3 imprinting. Nat. Commun. *6*, 6008.

Yamazawa, K., Kagami, M., Nagai, T., Kondoh, T., Onigata, K., Maeyama, K., Hasegawa, T., Hasegawa, Y., Yamazaki, T., Mizuno, S., et al. (2008). Molecular and clinical findings and their correlations in Silver-Russell syndrome: Implications for a positive role of IGF2 in growth determination and differential imprinting regulation of the IGF2-H19 domain in bodies and placentas. J. Mol. Med. *86*, 1171–1181.

Yang, H., Wang, H., and Jaenisch, R. (2014). Generating genetically modified mice using CRISPR/Cas-mediated genome engineering. Nat. Protoc. *9*, 1956–1968.

Yoon, B., Herman, H., Hu, B., Park, Y.J., Lindroth, A., Bell, A., West, A.G., Chang, Y., Stablewski, A., Piel, J.C., et al. (2005). Rasgrf1 Imprinting Is Regulated by a CTCF-Dependent Methylation-Sensitive Enhancer Blocker. Mol. Cell. Biol. *25*, 11184–11190.

Yu, W., Ginjala, V., Pant, V., Chernukhin, I., Whitehead, J., Docquier, F., Farrar, D., Tavoosidana, G., Mukhopadhyay, R., Kanduri, C., et al. (2004). Poly(ADP-ribosyl)ation regulates CTCF-dependent chromatin insulation. Nat. Genet. *36*, 1105–1110.

Zacharek, S.J., Fillmore, C.M., Lau, A.N., Gludish, D.W., Chou, A., Ho, J.W.K., Zamponi, R., Gazit, R., Bock, C., Jäger, N., et al. (2011). Lung stem cell self-renewal relies on BMI1-dependent control of expression at imprinted loci. Cell Stem Cell *9*, 272–281.

Zampieri, M., Guastafierro, T., Calabrese, R., Ciccarone, F., Bacalini, M.G., Reale, A., Perilli, M., Passananti, C., and Caiafa, P. (2012). ADP-ribose polymers localized on Ctcf-Parp1-Dnmt1 complex prevent methylation of Ctcf target sites. Biochem. J. *441*, 645–652.

Zimmerman, D.L., Boddy, C.S., and Schoenherr, C.S. (2013). Oct4/Sox2 binding sites contribute to maintaining hypomethylation of the maternal Igf2/H19 imprinting control region. PLoS One *8*:e81962.